EPFL

Drift-Diffusion Simulations of Charge Transport and Trap Dynamics in Organic Semiconductor Materials

Camilla Arietta VAEL-GARN

Acceptée sur proposition du jury

Prof. C. Ludwig, président du jury
Prof. F. Nüesch, Prof. B. Ruhstaller, directeurs de thèse
Dr G.-J. Wetzelaer, rapporteur
Dr C. Pflumm, rapporteur
Dr C. M. Wolff , rapporteur

École
polytechnique
fédérale
de Lausanne

2023

Acknowledgement

I would like to express my gratitude to the following individuals:

- Beat Ruhstaller, for providing me with the opportunity to pursue this PhD, co-directing the program, and offering valuable insights into the simulation aspect of my project.

- Sandra Jenatsch and Simon Züfle, for their guidance and supervision, as well as for engaging in fruitful discussions that brought fresh perspectives to both the experimental and simulation components.

- Roland Hany, for his support, manuscript feedback, thought-provoking questions that led to new insights, and extensive discussions on the dynamics of electron trap generation and decay, as well as diffusion.

- I would like to extend my thanks to Frank Nüesch for insightful discussions on physics, as well as for serving as my thesis director.

- My appreciation goes to my colleagues at Fluxim, with whom I've had engaging discussions and enjoyable times during company activities. Special thanks to Balthasar Blülle for incorporating requested features into the simulation software and providing workarounds for features that were not yet implemented.

- I am grateful to my father for taking the time to proofread my dissertation and for his efforts in learning about organic electronics.

- I would like to thank Tao Zhang for fabricating devices according to my specifications.

- I express my gratitude to Wei-Hsu Hu for fabricating high-quality devices and for the opportunity to collaborate with him on the subject of upconverter devices.

- Lastly, I want to acknowledge Matthias Diethelm for the stimulating conversations and the opportunity to continue his work on electron trap states in superyellow.

I dedicate this thesis to my husband Bryan Vael, who supported me during most of my scientific career; my son Cassius Vael who incited me to write my thesis in a healthy fashion; and my whole family for their support and relaxing moments.

Kurzfassung

Polymer Halbleiter haben auf dem Gebiet der organischen Elektronik aufgrund ihrer einzigartigen Eigenschaften und potenziellen Anwendungen große Aufmerksamkeit erregt. Durch ihre Fähigkeit, Ladungsträger zu transportieren und Licht zu absorbieren oder zu emittieren, haben sie in der Display-, Sensor- und gedruckten Elektronikindustrie viel Aufmerksamkeit auf sich gezogen. Besonders signifikant ist der relativ junge industrielle Erfolg von Displays auf der Basis organischer Halbleiter. Die Forschung an organischen Halbleitern hat seit ihren Anfängen gegen Mitte des letzten Jahrhunderts nicht nachgelassen. Von besonderem Interesse ist das Verständnis der ungeordneten Struktur in diesen Materialien und deren Einfluss auf die elektrischen und optischen Eigenschaften. In dieser Studie haben wir die Drift-Diffusions-Simulation genutzt, um komplizierte elektronische Mechanismen in drei verschiedenen Bereichen im Zusammenhang mit polymeren Halbleitern zu entschlüsseln.

Zunächst haben wir uns auf die Messmethode des thermisch stimulierten Stroms (TSC) konzentriert. Der bei TSC gemessene elektrische Strom stammt von eingefangenen Ladungsträgern, die bei Erhöhung der Temperatur mobil werden. TSC ist somit eine direkte Sonde für die Schlüsseleigenschaften von Fallenzuständen und wurde häufig bei anorganischen Halbleitern eingesetzt, um die Dichte von Fallenzuständen, die Fallenenergie und die Frequenz des Entkommens zu untersuchen. Wir untersuchen die Anwendbarkeit und Zuverlässigkeit der ursprünglich für anorganische Halbleiter entwickelten Formeln für das organische Gegenstück, indem wir die Drift-Diffusion an einem einfachen Elektroden-Halbleiter-Elektroden-Stapel simulieren. Wir stellten fest, dass die Formel für langsames Wiedereinfangen die genaueste ist, auch wenn sie für die Datenanalyse am kompliziertesten zu implementieren ist. Für praktische Zwecke erwies sich jedoch die Formel für den anfänglichen Anstieg als die robusteste Vereinfachung der Formel für langsames Wiedereinfangen. Außerdem entdeckten wir, dass nicht alle Fallenzustände aufgrund von Diffusion geleert werden können und ein Proportionalitätsfaktor berücksichtigt werden muss, um genaue Werte für die Fallendichte zu erhalten.

Zweitens untersuchten wir reversible Fallenzustände in einer Polymer-Leuchtdiode (PLED), die das Poly(p-phenylenvinylen) (PPV) Derivat superyellow (SY) als Emitter verwendet. Die während des PLED-Betriebs gebildeten Fallenzustände folgten einem kinetischen Prozess dritter Ordnung, verschwanden jedoch nach dem Abschalten des Geräts langsam mit einer Potenzgesetz-Rate. Unsere Untersuchung deutet darauf hin, dass die Bildung und Auflösung von Fallenzuständen auf einen Komplex aus Wasser- und Sauerstoffmolekülen zurückzuführen sein könnten. SY und andere Polymere weisen in der Regel universelle Elektronenfallen auf, die eine geringe Elektronenbeweglichkeit verursachen. Unsere Forschung zeigt, dass die beobachteten reversiblen Fallenstellen diesen bekannten universellen Fallenzuständen entsprechen und ihre bisher unerforschte Bildungskinetik und Reversibilität aufzeigen.

Schließlich untersuchten wir die Funktionsprinzipien eines Aufwärtswandlers, der superyellow als Emitter und einen Cyaninfarbstoff als Photodetektor verwendet. Diese Vorrichtung wandelt Licht im nahen Infrarotbereich (NIR) in sichtbares Licht um und ermöglicht so den Nachweis von für das menschliche Auge nicht sichtbares Licht. Auf komplett Organik basierte Aufwärtswandler sind noch relativ unerforscht, und die detaillierten Mechanismen, die den Aufwärtswandlungs-prozessen zugrunde liegen, sind noch nicht genau bekannt. Unsere Untersuchung konzentrierte sich darauf, die Ursache für die verlängerte Reaktionszeit des SY-Aufwärtskonverters zu verstehen, wenn die Gerätespannung erhöht wird. Wir haben festgestellt, dass die Elektronenmobilität innerhalb

der Emissionsschicht eine entscheidende Rolle bei der Beeinflussung des Verhaltens des Aufwärts-konverters spielt.

Abstract

Polymeric semiconductors have gained significant attention in the field of organic electronics due to their unique properties and potential applications. Through their ability to transport charge carriers and to absorb or emit light, they have attracted much attention in the display, sensing, and printed electronics industry. Particularly significant is the rather recent industrial success of organic semiconductor-based displays. Research on organic semiconductors has not ceased since its beginning in the middle of last century. Of special interest is the understanding of the disordered structure in these materials and its impact on electrical and optical properties. In this study, we have used drift-diffusion simulation to unravel intricate electronic mechanisms in three distinct areas related to polymeric semiconductors.

First, we focused on the thermally stimulated current (TSC) measurement method. The electric current measured in TSC originates from trapped charge carrier which become mobile upon increasing the temperature. TSC thus directly probes key characteristics of trap states and was commonly used on inorganic semiconductors to study trap site density, trap energy and attempt-to-escape frequency. We investigate the applicability and reliability of the formulas originally developed for inorganic semiconductors for the organic counterpart by employing drift-diffusion simulation on a simple electrode-semiconductor-electrode stack. We identified the slow retrapping formula as the most accurate, albeit being the most complicated to implement for data analysis. However, for practical purposes, the initial rise formula emerged as the most robust simplification of the slow retrapping formula. Additionally, we discovered that not all trap states can be emptied due to diffusion, and a proportionality factor must be considered to obtain accurate values for the trap density.

Second, we studied reversible trap states in a polymeric light-emitting diode (PLED) using the poly(p-phenylene vinylene) (PPV) derivative superyellow (SY) as the emitter. Trap states formed during PLED operation followed a third order kinetics, but after device switch-off slowly disappeared with a power law rate. Our investigation suggests that trap state formation and disaggregation may originate from a complex involving water and oxygen molecules. SY and other polymers commonly exhibit universal electron trap states, causing low electron mobility. Our research indicates that the observed reversible trap sites correspond to these known universal trap states, revealing their previously unexplored formation kinetics and reversibility.

Last, we examined the operational principles of an upconverter device that employed superyellow as the emitter and a cyanine dye as the photodetector. This device converts near infra-red (NIR) light into visible light, enabling the detection of light that is invisible to the human eye. All-organic upconverter devices are still relatively unexplored, and the detailed mechanisms underlying the up-conversion processes lack detailed understanding. Our investigation focused on understanding the cause behind the increased response time of the SY upconverter when the device voltage is elevated. We identified that the electron mobility within the emission layer plays a crucial role in influencing the behaviour of the upconverter device.

Table of Contents

List of abbreviations

CV	capacitance-voltage
DCB	Dichlorobenzene
DLTS	Deep-level transient spectroscopy
DMC	Decamethylcobaltocene
DPP-BTz	[[2,5-bis(2-octadecyl)-2,3,5,6-tetrahydro-3,6-diketopyrrolo[3,4-c]pyrrole-1,4-diyl]-alt-(2-octylnonyl)-2,1,3-benzotriazole]
DOS	Density of states
EGDM	Extended Gaussian disorder model
EQE	External quantum efficiency
ETL	Electron transport layer
F8BT	Poly[9,9-dioctylfluorene-alt-benzothiadiazole]
HOMO	Highest occupied molecular orbital
HTL	Hole transport layer
IDTBT	Indacenodithiophene-co-benzothiadiazole copolymer
IV	Current-voltage
ITO	Indium Tin Oxide
LCAO	Linear combination of atomic orbitals
LED	Light-emitting diode
LUMO	Lowest unoccupied molecular orbital
MEH-PPV	Poly[2-methoxy-5-(2'-ethylhexyloxy)-1,4-phenylene vinylene]
MIR	Mid-infra-red
NIR	Near infra-red
OPV	Organic photovoltaics
PEDOT:PSS	Poly(3,4-ethylene dioxythiophene)polystyrene sulfonate
PD	Photodiode
PLED	Polymer light emitting diode
PPV	Poly(p-phenylene vinylene)
SCLC	Space charge limited current
SY	Superyellow
TCNQ	Tetracyanoquinodimethane
TPBi	2,2',2"-(1,3,5-benzinetriyl)-tris(1-phenyl-1-H-benzimidazole)
TSC	Thermally stimulated current
UV	Ultraviolet
1D	One dimensional
2D	Two dimensional
3D	Three dimensional

List of figures

List of tables

Introduction

I   Structure and objectives

The traditional scientific method has been the conventional approach to understanding the behaviour of systems of various sizes. This approach involves a continuous cycle of observing effects, formulating hypotheses explaining the effects, designing and performing experiments to test hypotheses, analysing the acquired data and modifying the hypotheses[1]. Though, this method can be both time-consuming and expensive.

The increased computational processing power has made it possible to transfer specific parts of experimentation, such as device optimization and statistical analysis, to in silico simulations, thus speeding up research. For instance, screening is performed by means of simulation of thousands of molecules in medicinal chemistry to identify candidates that exhibit the desired properties, reducing research and development expenses significantly.

Simulation techniques can also be used to investigate and optimize devices like solar cells, light-emitting devices, transistors, and sensors based on organic semiconductors, with the charge drift-diffusion model being an exciting simulation technique for this purpose.

This PhD thesis focuses on investigating various ways in which the drift-diffusion model can be applied in semiconductor device research. Specifically, the thesis explores three different aspects of the use of drift-diffusion modelling:

(1) using drift-diffusion to generate synthetic device characterization data with known input parameters and investigate the performance of different traditional methods in interpreting the data;

(2) exploring how drift-diffusion can be used to quantify material parameters of interest by determining a device's response to different operating conditions; and

(3) investigating how drift-diffusion can be used to understand the working principles of a device and using the information gathered to improve its design.

The model system for this research is a polymeric semiconducting material, in particular the super yellow light emitting PPV copolymer, a widely used and highly efficient solution-processable conjugated polymer. Specifically, we investigate trap sites since they affect the device performance and may be formed during prolonged operation. The specific aspects of this research are detailed below and subdivided into chapters.

II   Chapter 1: Drift-diffusion study on thermally stimulated current

The fundamental properties of crystalline inorganic semiconductors, like their band structure, charge carrier dynamics and defect formation, are well studied. In contrast, the physics of organic semiconductors is not yet fully explored. This is, among other reasons, due to low intermolecular binding forces between organic molecules, leading to disorder in the material and, thus, to a more complex electronic structure.

One key difference between inorganic and organic semiconductors is their electronic band structure. Inorganic crystalline semiconductors have a well-defined and broad valence band and

conduction band. Thus, charge carrier transport across a device is uniform, and mobility is relatively high.

In contrast, organic semiconductors have a narrow distribution of transporting states and exhibit a complex energy landscape with many different states between the valence and conduction bands. These additional energy levels can participate in charge carrier transport and thus make transport complex and dependent on the local environment[2]. In general, the mobility of organic materials is relatively low.

Many experimental methods are used to characterise inorganic semiconductors, which were successfully adapted for the characterisation of organic semiconductors by accounting for the above-mentioned fundamental differences between the two types of materials. Examples of such measurements are current-voltage (IV or JV if current density instead of current is measured), capacitance-voltage (CV) or photoconductivity measurements.

However, other methods, like thermally stimulated current (TSC)[3], which investigated trap site properties like trap energy and trap density, were not rigorously adapted. Still, there are some groups that use TSC for the characterisation of trap sites in organic semiconductors. However, models explicitly developed for inorganic materials are commonly used to interpret the data.

In this chapter, we investigate the different methods employed to extract parameters from TSC measurements and compare their performance to data generated using a drift-diffusion model of a generic organic semiconductor. This allows us to assess the relative error arising due to usage of an extraction method developed for inorganic semiconductors on measured data of an organic semiconductor. In addition, we perform parameter variations in order to find the confidence intervals for the different extraction models.

III   Chapter 2: Electron trap evolution in Super Yellow polymer light-emitting diodes

Organic semiconductors have many advantages over their inorganic counterpart ranging from a higher degree in adaptation both in function and shape, over to lower production costs and more effortless scalability.

Especially for polymer semiconductor, economic prospectives are fantastic since high-cost fabrication steps like deposition in ultra-high vacuum systems can be avoided altogether. However, in contrast to small molecule semiconducting materials, polymer semiconductors suffer from the presence of inherent trap states and thus relatively low efficiency and fast degradation. This for example is reflected in the highest EQE achieved with polymer LEDs (23.5% [4]) as compared to the record EQE achieved with small molecule LEDs (36.4% for blue emitters[5] and 36.1% for red emitters[6]).

To improve the performance of polymer semiconductor materials, ways to alleviate effects from trap states have to be found. A first step toward this goal is the investigation of the chemical and physical trap origin and the formation mechanisms of trap states.

One kind of trap sites based on an oxygen-water complex is ubiquitously present in most polymer materials and is thought to be the primary reason for the poor electron mobility found in polymer semiconductors. In this chapter, we study the kinetics of water-oxygen trap states in a state-of-the-art PPV derivative named superyellow. Although their influence on device performance is pronounced, the concentration of water and oxygen is minimal and cannot be measured directly.

Thus, we use a combination of electrical characterization methods and drift-diffusion simulation to investigate the kinetics of this kind of trap sites. In this investigation, the drift-diffusion model used is specifically adapted for the device configuration and materials used in the experiment.

IV   Chapter 3 Upconverter devices based on superyellow as emitting layer

Human vision is limited to a wavelength range between 400 and 700 nm. However, many interesting natural phenomenon and industrial applications are more conveniently studied and monitored in the infra-red spectral region. Examples for this are atmosphere monitoring by observation of infrared absorption of molecules or night vision googles. One way to make the infra-red spectrum visible to humans is to convert the infra-red light into visible light.

In 2007[7], an all-organic device based on a photodetector connected in series to an OLED was proposed, which is capable of converting NIR light directly into visible light. Since then, only few of the physical effects exhibited by this kind of device were fully explained and many aspects of its functionality have not been illuminated.

In this work we, use a drift-diffusion model composed of a photo detecting and a light emissive layer, along with performance enhancing layers, to recreate observed physical effects like the slow-down of the device response speed with increasing voltage, which is an unusual phenomenon and opposite to the performance of a typical organic photodetector.

V   Drift-diffusion

The drift-diffusion model is a mathematical framework used to describe the behaviour of charged particles, such as electrons or ions in solid-state devices like transistors and diodes[8]. The model is based on the combined effects of two physical processes: drift and diffusion.

Drift refers to the directed movement of particles in response to an electric field. The electric field causes charged particles to accelerate and move in a particular direction.

Diffusion refers to the random movement of particles due to thermal energy. At any given time, particles are randomly moving in different directions, and this random movement leads to a levelling of the particle distribution.

The drift-diffusion model is mathematically described using the continuity equation, the Poisson equation and the drift-diffusion equation, which can be solved numerically to determine the distribution of free particles at any given point in time and space[9].

The drift-diffusion equation is given by

$$\vec{J}_n = qn\mu_n\vec{E} + qD_n\vec{\nabla}n \tag{0.1}$$

for electron current and

$$\vec{J}_p = qp\mu_p\vec{E} - qD_p\vec{\nabla}p \tag{0.2}$$

for hole current. q is the elementary charge, $\mu_{n,p}$ is the electron or hole mobility, respectively; n and p denote the density of electrons or holes, respectively; E is the electric field, $D_{n,p}$ the diffusion constant of electron or hole, respectively and $\vec{\nabla}$ is the nabla operator. The first summand of the equation describes the contribution from the drift, while the second summand (subtrahend for

the hole equation) describe the diffusion part. The diffusion constant in this model is given by Einstein relation

$$D_{n,p} = \mu_{n,p} \frac{k_B T}{q} \qquad (0.3)$$

with k_B the Boltzmann constant and T the temperature. This relation makes the dependence of the diffusion on temperature directly visible.

The continuity equation is used to calculate the continuous transport of charge carriers from one site to the neighbouring site also taking into account sources and sinks for charge carriers.

In the simulation, charged particles like electrons can be generated by the absorption of photons and splitting of the exciton into a free electron (transfer from the HOMO to the LUMO). Also, electrons and holes can be removed by recombination with a charge carrier with opposite charge or be trapped in trap states. These processes are considered by implementing generation, recombination, and trapping terms into the continuity equation.

$$\frac{dn}{dt} = \frac{\vec{\nabla} \vec{J}_n}{-q} - R_{Langevin} - R_{nt} + g_{opt} G_n \qquad (0.4)$$

for electrons and

$$\frac{dp}{dt} = \frac{\vec{\nabla} \vec{J}_p}{q} - R_{Langevin} - R_{pt} + g_{opt} G_p \qquad (0.5)$$

for holes. $R_{Langevin}$ is the bimolecular recombination of a free electron in the LUMO with a free hole in the HOMO, R_{nt} and R_{pt} describe the rate of change in free electrons or holes due to interaction with trap states, g_{opt} is the generation efficiency and $G_{n,p}$ are the generation rates for electrons or holes, respectively.

The bimolecular recombination can be expressed by

$$R_{Langevin} = \eta(\mu_n + \mu_p)\frac{q}{\varepsilon}(np - n_i^2) \qquad (0.6)$$

with η the Langevin prefactor, ε the relative permittivity of the semiconductor and n_i the intrinsic free charge carrier density.

A further extension of the drift-diffusion model is the implementation of trap states – states with an energy within the bandgap.

To consider these states, a second set of continuity equations is introduced. These take the form

$$\frac{dn_t}{dt} = c_n n(N_t - n_t) - e_n n_t + e_p(N_t - n_t) - c_p p n_t \qquad (0.7)$$

for electron trap sites and

$$\frac{dp_t}{dt} = c_p p(P_t - p_t) - e_p p_t + e_n(P_t - p_t) - c_n n p_t \qquad (0.8)$$

for hole trap sites[10].
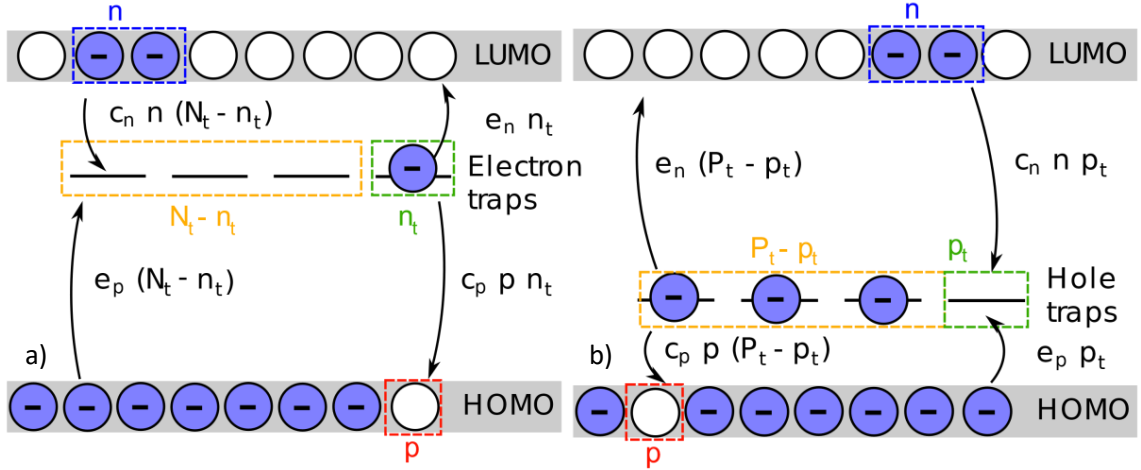
Figure I Schematic for a) electron trap sites and b) hole trap sites within the bandgap. The different possibilities for capturing and releasing charge carriers into and from the trap site are marked with arrows and corresponding formulas.

The first two terms in (0.7) denote capturing and release of an electron from the LUMO (corresponding to R_{nt}) while the last two describe the capturing and release of electrons from the HOMO (Figure Ia).

In (0.8), the first two terms are capturing and release of a hole from/into HOMO (corresponding to R_{pt}) and the last two terms are capturing and release of holes from/into the LUMO (Figure Ib). If those processes are in equilibrium, a rate for Shockley-Read-Hall recombination can be calculated yielding

$$R_{SRH} = \frac{N_t\left(np - n_i^2\right)}{\frac{1}{c_p}\left(n + N_{0,n}exp\left(\frac{E_t - LUMO}{k_B T}\right)\right) + \frac{1}{c_n}\left(p + N_{0,p}exp\left(\frac{HOMO - E_t}{k_B T}\right)\right)} \tag{0.9}$$

In this formula, $c_{n,p}$ is the capture rate for electrons or holes, respectively, N_t is the total number of electron trap sites, and n_t the number of filled trap sites. Correspondingly, P_t is the number of total hole trap sites and p_t the number of filled hole trap sites. $E_{n,p}$ is the release rate from the trap sites for electrons and holes which is related to the respective capture rates via

$$e_n = c_n N_{0,N} \cdot \exp\left(\frac{E_t - LUMO}{k_B T}\right) \tag{0.10}$$

for electron emission

$$e_p = c_p N_{0,P} \cdot exp\left(\frac{HOMO - E_t}{k_B T}\right) \tag{0.11}$$

for hole emission. $N_{0,n}$ is the density of states (DOS) for LUMO and $N_{0,p}$ is the DOS for HOMO.

The external applied voltage difference and the contribution from charged particles and ions within the device determine the electric field in the drift-diffusion simulation. The internal electric field is expressed by the Poisson's equation

$$\varepsilon \triangle \varphi = q\left(p - n + p_t - n_p - A_{Doping} + D_{Doping}\right) \tag{0.12}$$

The drift-diffusion simulation framework can also be used to calculate non-equilibrium cases where one external parameter like temperature or voltage is changed during simulation. This so-called transient simulation takes on the form

$$S_{t+1} = S_t + \alpha * dt \tag{0.13}$$

where S_t is the current simulation step that is updated by a small rate of change α in the external parameter with appropriate time step dt to yield the next simulation step S_{t+1}. It is important to note that each simulation step is at steady state while the overall simulation shows how the system changes with time. Parameters dependent on the external parameter that changes during the transient simulation must be adjusted at each time step.

Drift-diffusion simulation can be carried out for 3D, 2D and 1D systems. For this work, we assume the active layer to be isotropic. It therefore is sufficient to use a 1D simulation.

The drift-diffusion model used in this work is a commercial tool named Setfos (version 5.1 and 5.2) by Fluxim AG.

VI   Advantages and limitations of drift-diffusion

Drift-diffusion simulation is a macroscopic model that uses charged particles' averaged behaviour. It can be solved using fast numerical methods like finite difference method (FDM) which makes it possible to simulate large systems like complete devices with a reasonable accuracy using only little computational resources and time[11][12].

Drift-diffusion simulation can predict various parameters like lifetime and efficiency on a device level. In addition, it allows to locally investigate recombination rate, charge carrier mobility, charge carrier density, electric field and doping concentration. These parameters are generally not observable in experiments. Device behaviour that has its origin in local differences in the above-mentioned parameters thus are best studied using drift-diffusion.

It is possible to couple drift-diffusion simulation with optical models[10] to calculate absorption and emission of light or thermodynamic models to calculate a device's energy transfer and heat dissipation. This coupling yields a more comprehensive device simulation and allows to additionally predict local device temperature and internal quantum efficiency. For PLEDs, also luminance and colour of the emission can be predicted while for photovoltaic cells a prediction for spectral response, open circuit voltage and short-circuit current is possible.

The predictive power of drift-diffusion allows to test different materials and optimise their properties like layer thickness and orientation without the need of extensive experimental adjustment. This potentially saves money and speeds up research.

However, there are also limitations for the use of drift-diffusion simulation. The drift-diffusion model does not consider quantum effects and assumes local equilibrium. Especially at small length scales, this might lead to errors. In such situations simulation models like non-equilibrium Green's function yield more accurate results. Also, it is not possible to depict charge transport on a molecular level. Anisotropies in charge carrier transport due to the molecular structure of the material is better simulated using for example kinetic Monte Carlo[13].

The simulation results' reliability also strongly depends on the input parameter's accuracy.

If it is impossible to determine input parameters like mobility or recombination rate, only qualitative trends but no quantitative values can be simulated.

VII   Polymers

The term polymer is used to refer to the material as a whole. Depending on its degree of crosslinking a polymer either is composed of long single strands of molecules (coined macromolecules by Staudinger[14]) with a molecular weight ranging from 50'000 to several millions of Daltons, or of a 2D or 3D network of crosslinked strands. Each macromolecule is composed of up to several thousand monomer repeating units (analogous to crystallography the smallest repeatable unit). If only one kind of monomer is used for a polymer, it is called homopolymer. More complex polymers can also be made up by two or more different monomers with different ratios. Such polymers are called block- or copolymers depending on the ordering of the monomers. If the monomers are mixed randomly, it is a copolymer, if there are large regions within the polymer consisting of repeating units of only one monomer, it is called a block polymer.

The properties a polymer exhibits depends on the nature and functionality of the constituting monomers, the number of repeating units, the degree of polymerization, the 3D structure they exhibit, or the additives that were added.

Polymers were thought to be only good insulators, e.g, useful to insulate copper wires. This notion changed following the work of Hideki Shirakawa, Alan G. MacDiarmid and Alan J. Heeger in the 1970's on polyacetylene[15]–[18], a conjugated organic polymer. They showed that polyacetylene exhibits semiconducting properties upon partial reduction (n-doping) or oxidation (p-doping). This discovery led to the development of the field of polymer electronics and was awarded with the Nobel prize in chemistry in the year 2000[19].

One of the key advantages of using polymers is the ease of processing using solution-based techniques, making it possible to produce large-area devices cheaply. Additionally, the versatility of polymers allowed for the design of materials with specific optical and electronic properties, enabling the creation of highly efficient optoelectronic devices.
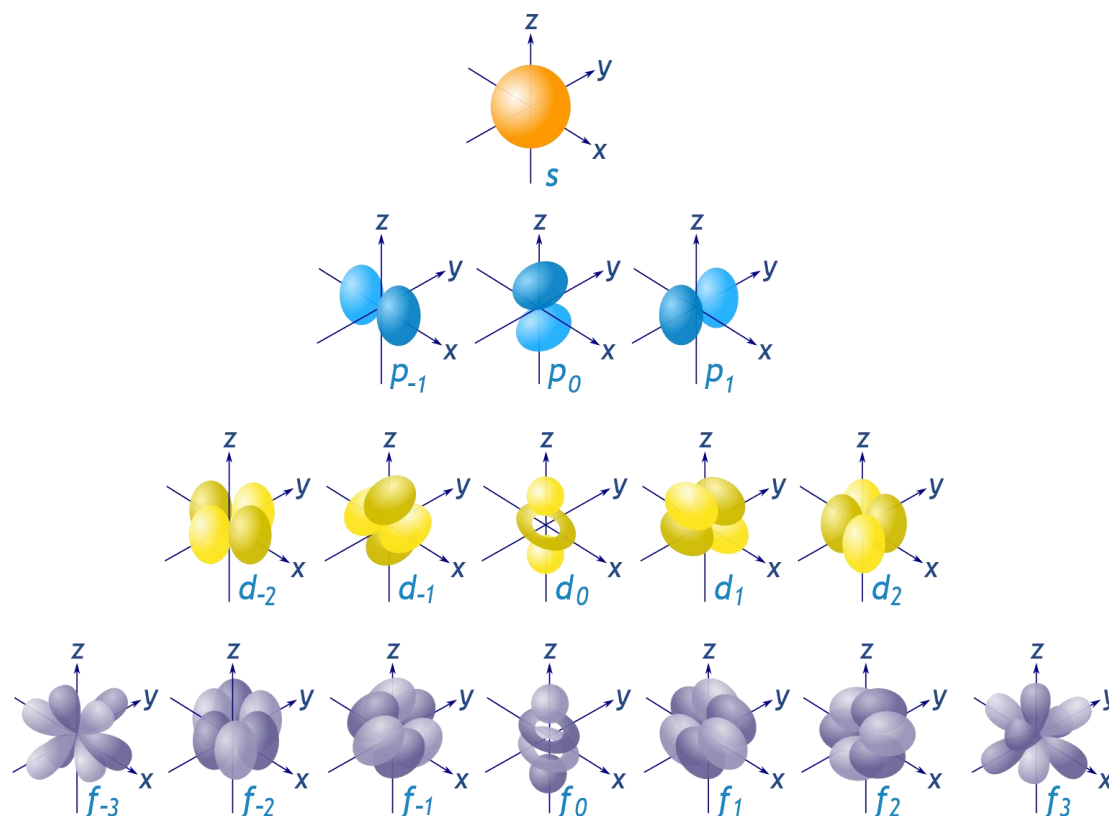
Figure II Shape and geometrical orientation of the atomic orbitals. Source of the image:
https://www.mathsisfun.com/physics/images/orbitals.svg

In order to understand how a polymer can become semiconducting it is necessary to take a look on how molecules form bonds. There are different theories with varying degrees of complexity to explain bond formation. To understand the most important properties, the linear combination of atomic orbitals (LCAO) theory is a suitable model[20].

Each atom in its neutral state has a number of electrons equal to its position in the table of elements. Since electrons have a negative charge and repel each other, they inhabit a certain distribution around the positively charged atomic core. It is not possible to pinpoint the exact location of each electron since they move around and exhibit some wave-like properties. Instead, the vicinity where an electron is likely to be found is described by a wave function and commonly visually represented as an atomic orbital. The shape of the orbital, the energy associated with it and its geometrical orientation follows a certain rule and can be described using different quantum numbers (Figure II).

Electrons of a single atom are restricted to locations around the atomic nucleus and thus are relatively localised. When an atom forms a chemical bond, its outermost electrons will interact with the outermost electrons of another atom and thereby new wavefunctions are created. These wavefunctions can be calculated by a linear combination of the constituent wavefunctions This leads to the creation of new wavefunctions via hybridization of orbitals where the resulting orbital exhibits properties from all constituting atomic orbitals (hybridized orbitals). When two electrons of two different atoms interact with each other, their wave functions interact constructively and destructively, which results in the formation of a bonding molecular orbital with a lower energy level than the atomic orbitals, and an anti-bonding orbital with energy higher than the atomic

orbitals (Figure III). The properties of the new orbitals are described by new wavefunctions which are a linear combination of both constituting atomic orbitals. There are exactly as many linear combinations of orbitals as there are participating atomic orbitals. Not all newly formed molecular orbitals are filled. Each orbital can accommodate two electrons. In most cases this leads to filled bonding and empty anti-bonding orbitals. The filled molecular orbital lying highest in energy is termed highest occupied molecular orbital (HOMO) and the first empty molecular orbital lowest in energy is called lowest unoccupied molecular orbital (LUMO).

In order to form a bond, two electron orbitals must have a similar energy and a favourable geometrical orientation. Two (lone) electrons directly facing each other (aligned on a line between both atoms) will form a σ bond. If there are other lone electrons present in orbitals that are perpendicular to the orbitals forming the σ bond, they also can hybridize and form a bond due to intermolecular electronic coupling – this results in a π bond which is weaker in nature due to less overlap than a σ bond.
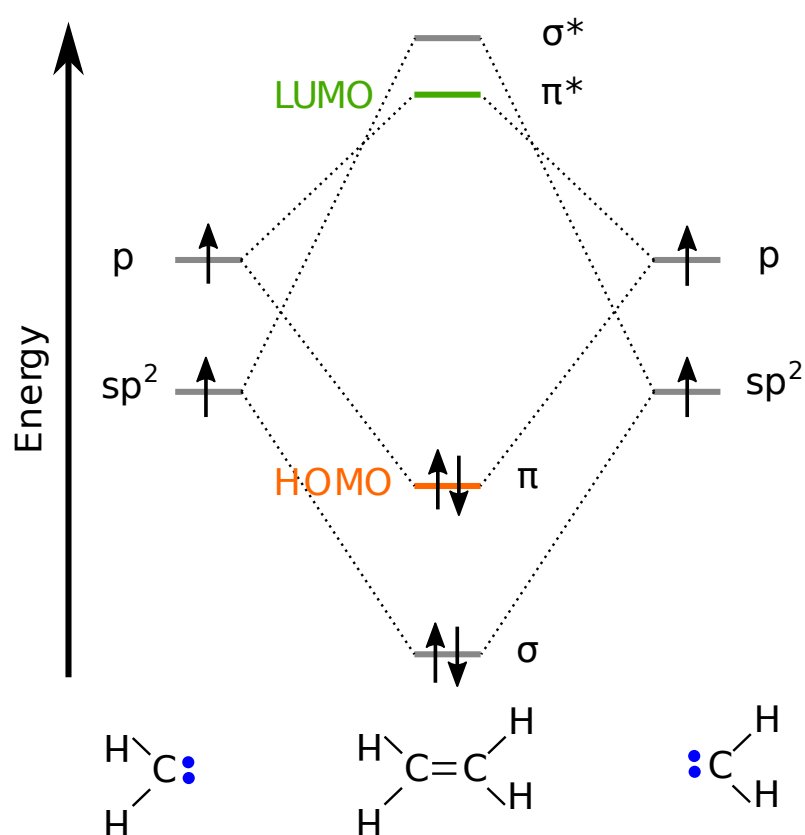
Figure III Molecular orbital diagram for ethene formation. sp2 and p are atomic orbitals on the carbon atoms which can form bonds. σ and π are binding molecular orbitals that form upon bond formation and σ* and π* are anti-bonding orbitals. Since the π-bond is the molecular orbital highest in energy which still has electrons present, it is the HOMO. The π* molecular orbital is the first empty orbital and thus is the LUMO.
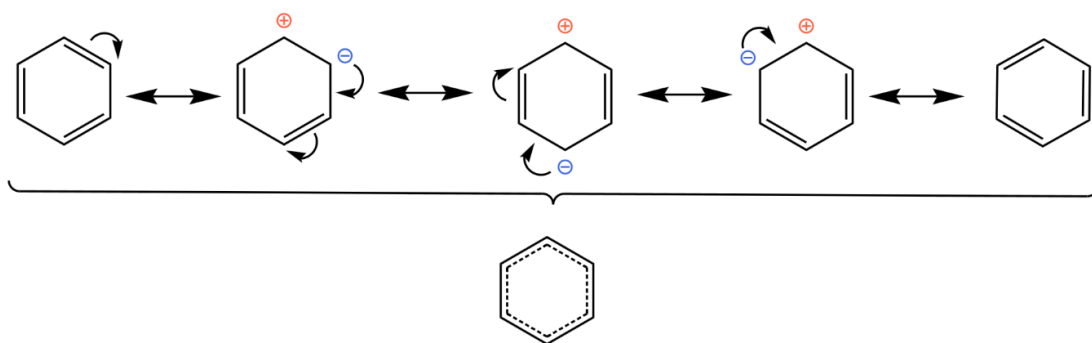
Figure IV Lewis formula of benzene with different resonance structures. Since the electrons in the π bonds are delocalised over the whole molecule, benzene is also represented with a solid- dashed double line to illustrate the delocalisation.

IX   Origin of conduction in polymers

As all organic materials, conducting polymers mainly are composed of carbon and hydrogen atoms. The semiconducting properties arise from conjugation - the alternation of double and single bonds between carbon atoms along a chain[21]. Some carbons may also be substituted by heteroatoms like nitrogen, sulphur and oxygen.

However, where the double bonds in a conjugated molecule are located is not straight forward. Each carbon atom has a lone electron which could form a π bond with the electron of either neighbour. The π bonds and thus the electrons are delocalised between each of the neighbouring atoms. An example of this delocalisation is given for benzene (Figure IV)

The addition of more conjugated segments to a molecule will increase the number of filled states near the HOMO and also increase the number of empty states close to the LUMO (Figure V)[22] . If enough conjugated segments are present in the molecule, the energy difference between the states will diminish and instead of a single HOMO and LUMO state, a distribution of states with similar energy emerges[18]. This distribution of states with similar energy in the LUMO allows the transport of electrons between the states and thus is key to the ability of the molecule to transport electrons from one end to the other. However, this transport will only occur if additional charge carriers are introduced, either by doping the molecule, the generation of free electron-hole pairs upon illumination, or via injection of external charges due to application of an electric field.
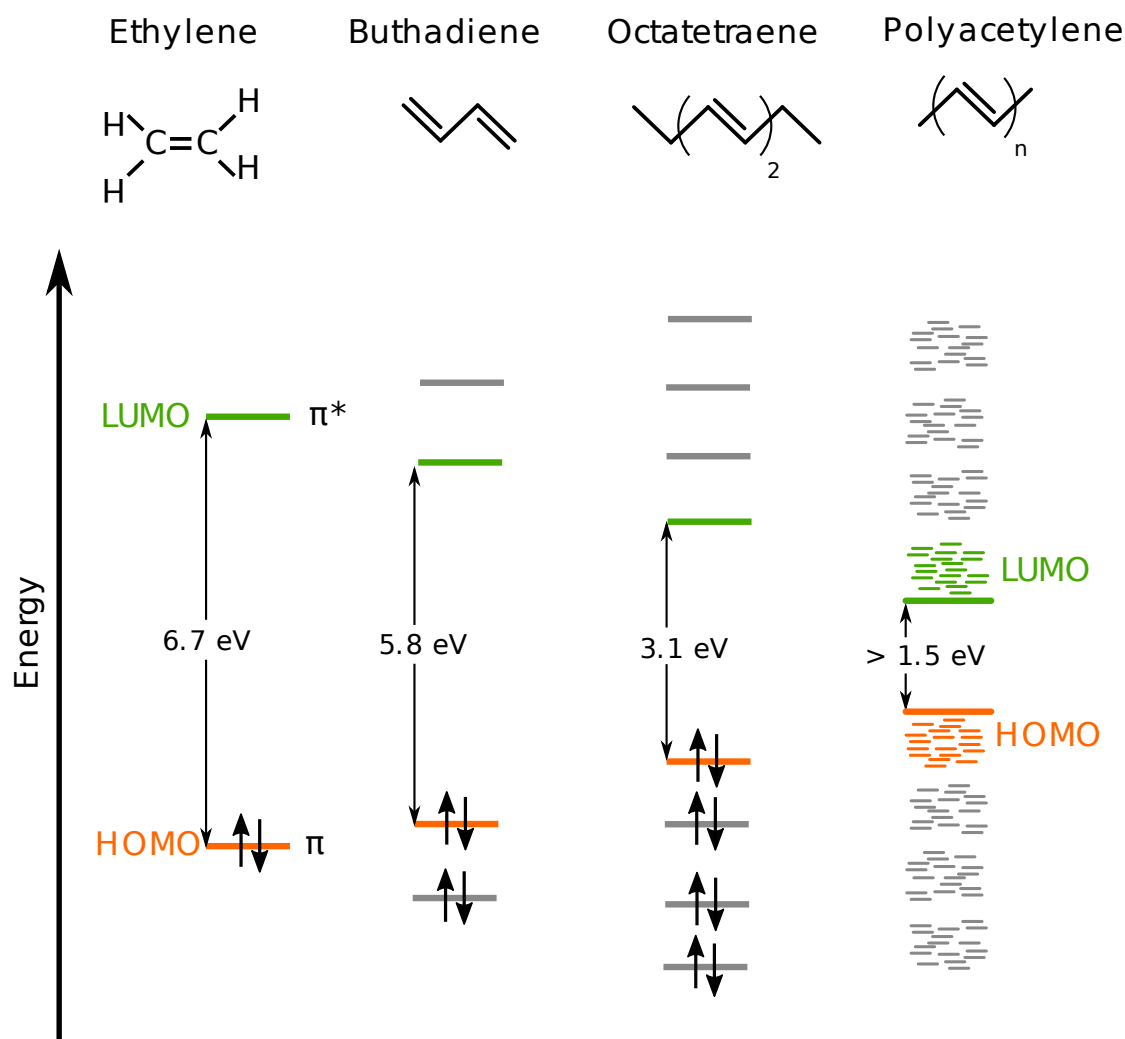
Figure V Energy diagram for the π orbitals of conjugated molecules of various lengths. The longer the conjugated system becomes, the closer in energy are the different states of the molecules. For polymers with hundreds of conjugated segments, the states are close enough to easily allow transport of charge carriers from one state to another. The electrons filling the HOMO states and the states below in polyacetylene were omitted for better visibility.

X   Charge carrier transport in organic and crystalline inorganic semiconductors

As opposed to the strong ionic and covalent bonds present in crystalline inorganic semiconductors, the intermolecular interactions in organic semiconductors are mainly determined by weak van der Waals forces and therefore give rise to a relatively narrow electronic band structure with a width of 50-500 meV[23]. As a result, charge carrier transport in organic polymers cannot be well explained by the delocalised transport in valence and conduction bands (Figure VIa). Instead, charge carriers are localized at molecular units, e.g. segments of a conjugated polymer chain and move by incoherent hopping among adjacent sites[24] (Figure VIb). A further consequence of the weak intermolecular interaction is that no strong force exists which tightly binds molecules to each other. This allows for large thermal motions of polymer segments in the range of 0.1 Å [25] leading to structural and energetic disorder. The different hopping sites therefore have a statistical variation in energy and position and do not contribute equally well to the transport of charge carriers. Therefore, an effective transport level was introduced to distinguish between the sites[26]. States that lie deeper in the gap than this effective transport level are called trap states as they tend to

hinder charge transport, leading to low effective carrier mobility. Typical mobilities measured in polymers range from 10^{-7} to 10^{-3} cm^2/Vs for holes, and the electron mobility is usually smaller than the hole mobility by a factor of 10 to 100[27].

XI   Origin of trap sites in polymers
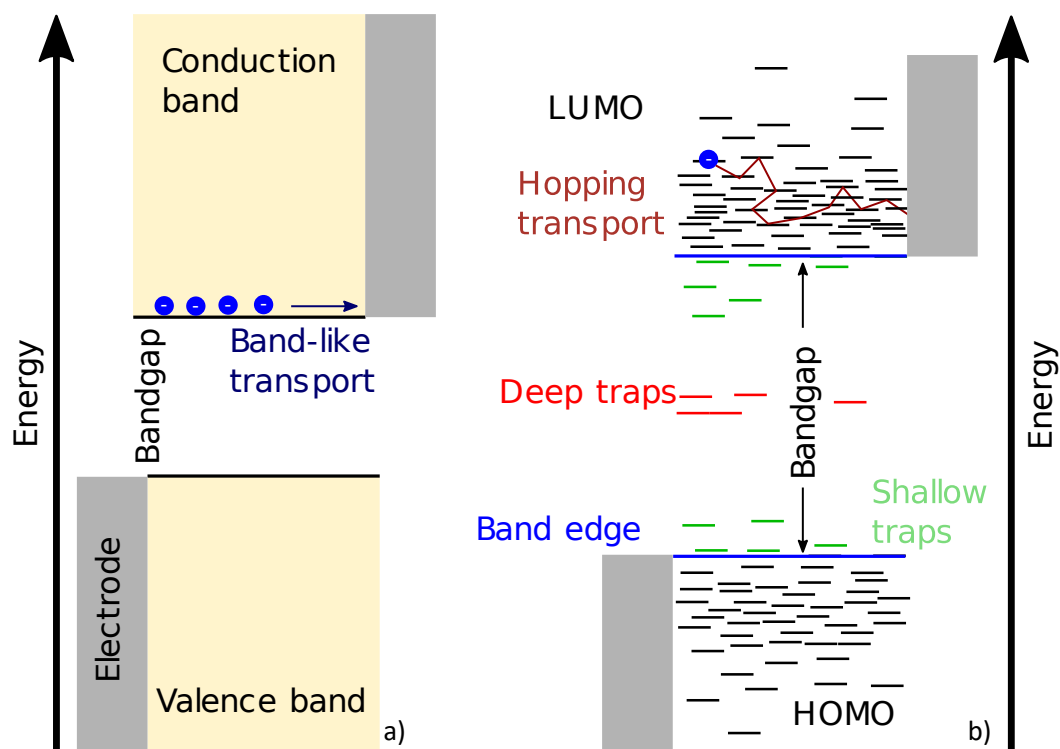
Figure VI. a) Charge carrier transport model for crystalline inorganic semiconductors. An inorganic material is sandwiched between two electrodes. Broad bands with continuous states lead to band-like, uniform charge carrier transport (dark blue). b) charge carrier transport model for disordered polymer semiconductors. Combined spatial and energy diagram of a disordered polymer semiconductor containing shallow (green) and deep traps (red) within the bandgap. States are discrete and localized Charge carrier transport occurs via hopping between the states (dark red). Marked on the diagram is the "band" edge which is used to distinguish transport states from shallow trap states.

Disorder is one major factor responsible for the presence of trap states with low energy, i.e. they have a slight energy difference from the band gap edge, and have typically a high density – on the order of 10^{17} to 10^{19} cm^{-3} [28]. Other trap states can be attributed to the presence of impurities and dopants (with varying trap depth), which locally change the molecular environment and therefore the intermolecular interactions[29]. Also, traps may come from interfacial degradation[30] and self-ionization[28]. Depending on their relative energetic positions from the respective band edge i.e. trap depth at a given temperature, traps can be termed shallow if located within a few k_BT of the band edges (displayed in green in Figure VI), or deep if they lie several k_BT from the band edges (displayed in red in Figure VI). Traps found in the vicinity of the lowest unoccupied molecular orbital (LUMO) generally trap electrons, whereas traps close to the highest occupied molecular orbital (HOMO) generally trap holes.

XII   Effect of trap sites

Trap sites in organic semiconductors have different effects on device performance, depending on their energy with regards to the conducting states[31]. Shallow trap sites will mainly slow down charge carrier transport within a given layer. This occurs since shallow trap states can contribute

to the transport of charge carriers[29]. However, the energy levels of these states are lower than the surrounding states. This means that the charge carriers occupying these states need to acquire energy to hop towards another state. This energy can be gained by absorption of phonons i.e thermal energy from the surrounding medium. The rate of phonon absorption is usually lower than the hopping rate. The charge carriers therefore remain longer in shallow trap states than in transport states and thus the overall transport of charge carriers across a device is decelerated. The degree of deceleration depends on the relative concentration of shallow and transport states, and on the trap energy. The more trap states are present and the lower their energy, the lower the overall mobility becomes. Shallow trap sites can also act as scattering centres which further reduces mobility.

Deep trap states do reduce the number of free charge carriers within the device[29]. There are two effects contributing to this. First, the trap sites usually are close to the middle of the band gap and have an affinity for electron and holes. This leads to another recombination pathway where trapped charge carriers can easily recombine with a free charge carrier of opposite sign. This recombination type is termed Shockley-Read-Hall recombination. In addition, charge carriers which are trapped in a deep trap which do not act as a recombination centre act as static charges and thus reduce the internal electric field. This effect leads to a slower transport of charge carriers through the device. Effects from deep trap sites are most pronounced at low applied field since then the free charge carrier concentration is low and the recombination of charge carrier thus has a higher impact on the charge carrier density.

The presence of trap states in organic photovoltaic devices can cause non-radiative trap-assisted recombination (SRH) of the dissociated charge carriers, which decreases the quantum efficiency of the devices[32]. Also, trap states can alter the energy level alignment of the absorption layer[33], which potentially reduces the fill factor and the open circuit voltage[34]. The presence of a trapped charge may also increase degradation by promoting chemical reactions with oxidants like H_2O and O_2[29]. On the positive side, traps can assist with the dissociation of excitons into free charge carriers and thereby increase the efficiency of the device[35].

In PLEDs trap states lower the external quantum efficiency (EQE) by providing a non-radiative recombination pathway (SRH recombination). They also lead to an imbalance in charge carrier mobility shifting the emission zone towards an electrode. This may lead to a lower light out-coupling efficiency and to quenching of excitons at the trap sites. Overall, this leads to a reduction in electroluminescence.

Trap states have a significant impact on the performance of devices based on organic semiconductors. Optimization of devices therefore requires the investigation of the origin and the effects of traps in search of ways to reduce the number of traps or their impact.

XIII   Strategies to counter trap states

It was found by Nicolai et al. that there exists a common electron trap level in polymeric semiconductors at ~3.6 eV below the vacuum level with a density of $10^{17}–10^{18}$ cm^{-3} [36], which might have a common origin[37]. The presence of such traps is thought to be the origin of the imbalance between the hole and electron mobility in organic polymers. The most probable candidate leading to these trap states was identified by Zhuo[38] and Nicolai to be a bis-hydrated-oxygen complex. One of the conclusions that was drawn by Nicolai is that trap free transport with near equal electron and hole mobility can be achieved by using active materials with a LUMO higher than 3.6 eV. Therefore, by carefully choosing the materials, the effects of some of the deep traps can be

eliminated altogether. However, this approach limits the number of available materials for device fabrication.

Another way of dealing with those deep traps which reduce the free electron density was demonstrated by Zhang and co-workers[39]. They used decamethylcobaltocene (DMC) as an n-type dopant in poly[2-methoxy-5-(2-ethylhexyloxy)-1,4-phenylenevinylene] (MEH-PPV) to fill the deep trap states with electrons. For a doping concentration of about 1:20% they achieved an electron current which was nearly equal to the hole current. From space charge limited current (SCLC) measurements, they found an electron mobility of $1.7 * 10^{-6}$ cm^{2}V^{-1}/s and a hole mobility of $1.4 * 10^{-6}$ cm^{2}V^{-1}/s. However the presence of dopants can also cause the formation of additional traps in the device which pin the Fermi level and decrease the mobility[28].

It was demonstrated by Nikolka et al. for a low-disorder, p-type indacenodithiophene-co-benzothiadiazole copolymer (IDTBT) field-effect transistor[40] and for a [[2,5-bis(2-octadecyl)-2,3,5,6-tetrahydro-3,6-diketopyrrolo[3,4-c]pyrrole-1,4-diyl]-alt-(2-octylnonyl)-2,1,3-benzotriazole] (DPP-BTz) diode [41] that the addition of small molecule additives like tetracyanoquinodimethane (TCNQ) or the incomplete removal of solvents like dichlorobenzene (DCB) have a beneficial influence on the device performance. They argued that the solvent or additives fill nanometric voids inside the polymers and thus prevent water from entering these voids. Therefore, no water-induced deep traps will form[42] which could decrease the current density and the stability of the device. Nikolka et al. used this approach for other polymers and received a hole mobility of $1 *10^{-2}$ cm^{2}V^{-1}/s for poly[9,9-dioctylfluorene-alt-benzothiadiazole] (F8BT) which is among the highest values reported for this material. This also demonstrates that the introduction of small additives to prevent water incorporation might be a general approach to increase device stability. However, especially solvent molecules tend to evaporate, leaving empty voids behind which can be filled by water later on.

XIV   Models for mobility

The ability of charged particles to move through a material like a metal or a semiconductor as a response to the presence of an electric field is termed mobility. Charge carriers with a high mobility react more strongly to an electric field than charge carriers with a low mobility and thus are faster. Mobility is strongly dependent on material properties like defect concentration and polarity, and on external factors like temperature and the applied field[43][44]. For these reasons, the mobility of a material usually is determined experimentally. However, there exist different models which allows to make predictions about charged particles mobilities under various conditions. Two important models used in this work are presented here.

XIV.a   Constant mobility

The constant mobility model assumes that the mobility of charge carriers in a material is independent of the carrier concentration, temperature, or electric field. It is a simplified model that can be useful for understanding some basic properties of low-mobility organic semiconductors.

The constant mobility model is often used when the mobility of the charge carriers is relatively insensitive to the doping concentration or the external conditions, such as temperature or electric field. This can be the case for some highly disordered materials or materials with a low degree of crystallinity. In such cases, the mobility may be limited by the intrinsic properties of the material, such as the energetic disorder or the presence of trapping states, which are not strongly affected by the external conditions.

Another situation in which the constant mobility model may be appropriate is when the charge carriers are predominantly transported through a particular transport pathway, such as a percolation network or a preferentially oriented crystallographic direction. In such cases, the mobility may be limited by the properties of the dominant transport pathway, rather than the overall material properties.

The formula applied for the constant mobility case is

$$\mu_{n,p} = const. \tag{0.14}$$

However, it is essential to note that the constant mobility model is a simplified model and may not accurately describe the behaviour of charge carriers in low-mobility organic semiconductors in all cases. Often, the mobility of charge carriers in organic semiconductors is highly dependent on factors such as carrier concentration, temperature, and electric field, and more complex transport models are then necessary to accurately describe their behaviour.

XIV.b   Extended Gaussian disorder model

The Extended Gaussian Disorder Model (EGDM) is a theoretical framework used to describe charge transport in organic disordered polymers as thermally assisted hopping between randomly distributed local states[45]. It assumes that the energetic disorder in organic semiconductors arises from a Gaussian distribution of site energies and also takes into account non-Gaussian effects, such as molecular vibrations, molecular conformational changes, and intermolecular charge transfer.

The EGDM is based on the numerical solution of a 3D master equation representing hopping of charge carriers on a rigid cubic lattice

$$\sum_{j\neq i}\left[W_{ij}p_i(1-p_j) - W_{ij}p_j(1-p_i)\right] = 0 \tag{0.15}$$

with a transition rate

$$W_{ij} = \begin{cases} v_0 exp\left[-2\alpha R_{ij} - \dfrac{\varepsilon_j - \varepsilon_i}{k_B T}\right], \varepsilon_j \geq \varepsilon_i \\ v_0 exp\left[-2\alpha R_{ij}\right], \quad \varepsilon_j < \varepsilon_i \end{cases} \tag{0.16}$$

where $p_{i,j}$ is the probability that site i,j is occupied by a charge carrier, v_0 is the attempt to hop frequency, α is the inverse localization length of the wave function, R_{ij} is the distance between site i and j, W_{ij} is the transition rate for hopping from site i to j, and $\varepsilon_{i,j}$ is the energy of site i,j.

Spatial averaging of the master equation solution results in an analytical description of the effective mobility in 1D

$$\mu(T,p,E) = \mu_p(T,p)f_E(T,E) \tag{0.17}$$

with

$$\mu_p(T,p) = \mu_0 c_1 exp[-c_2\hat{\sigma}^2]exp\left[\frac{1}{2}(\hat{\sigma}^2 - \hat{\sigma})\left(\frac{2p}{N_{0,p}}\right)^\delta\right] \tag{0.18}$$

15

and

$$f_E(T,E) = exp\left\{0.44\left(\hat{\sigma}^{3/2} - 2.2\right)\left[\sqrt{1 + 0.8\left(\frac{Eq}{N_{0,p}^{1/3}\sigma}\right)^2} - 1\right]\right\} \qquad (0.19)$$

and

$$\delta = 2\frac{ln(\hat{\sigma}^2 - \hat{\sigma}) - ln(ln(4))}{\hat{\sigma}^2} \qquad (0.20)$$

and

$$\hat{\sigma} = \frac{\sigma}{k_B T} \qquad (0.21)$$

Where σ is the width of the Gaussian, p is the density of free holes, $N_{0,p}$ is the density of states in the valence band, and μ_0 is the mobility prefactor. Throughout the thesis following values for c_1 and c_2 are used: $c_1 = 1.8 \times 10^{-9}$ and $c_2 = 0.42$

The EGDM accounts for the electric field, charge carrier density and temperature dependence of charge carrier mobility. It can be used to analyse and optimize the device performance by predicting the impact of disorder on the device properties, such as the charge carrier mobility, exciton dissociation efficiency, and radiative recombination rate.

The EGDM has been widely used in the design and optimization of organic photovoltaics, OLEDs, and other optoelectronic devices. However, it should be noted that the EGDM is still a simplified model and does not capture all the complex and dynamic effects that can occur in real organic semiconductor systems.

XV   PLED working principle

A polymer light emitting diode (PLED) contains an organic polymer as emissive layer. In a PLED, the principle of electroluminescence is utilized to generate light from the radiative recombination of injected charge carriers within a material[46][47].

In the most basic PLED, a thin polymer film is sandwiched between two electrodes, an anode and a cathode. A typical anode material is indium tin oxide (ITO) since it has a relatively high work function of around 4.8 eV, a very flat surface and is transparent. The latter property allows the outcoupling of light which is generated in the polymer. For the cathode, a low work function metal like calcium (2.9 eV) is often used. To protect this electrode from oxidation, a layer of silver or aluminium is deposited on top[48].
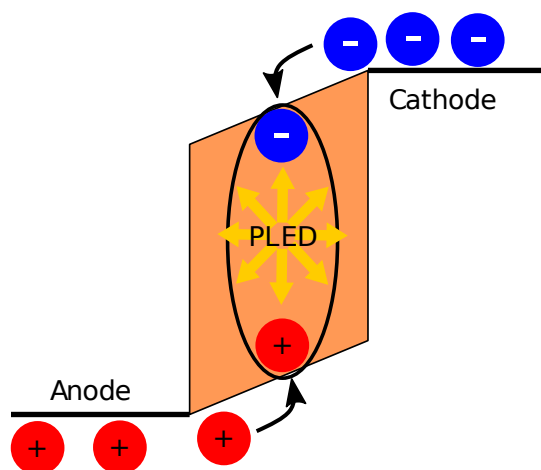
Figure VII Basic working principle of a polymer light diode. The most important steps are injection, transport and recombination.

When a voltage above the bandgap is applied across the device, electrons are injected into the polymer from the cathode and holes are injected from the anode. These injected carriers move through the polymer and recombine to form excitons (neutral bound excited states). If the exciton has a singlet state, it decays radiatively under emission of photons (Figure VII). The colour of the emitted light is determined by the polymer material and its energy bandgap and can range from the UV to the NIR range.

To achieve high device performance, the efficient injection, transport and radiative recombination of charge carriers is critical. This can be improved by optimizing the energy level alignment between the electrodes and the polymer material, controlling the morphology and composition of the layer and interfaces, and increasing mobility of the layers. For example, hole transporting layers (HTL) like (PEDOT:PSS) or electron transporting layers (ETL) like 2,2',2''-(1,3,5-benzinetriyl)-tris(1-phenyl-1-H-benzimidazole) (TPBi) can be added to control the location of the recombination zone.

XVI   Upconverter working principle

The basic idea behind a NIR-to-visible-light upconverter device is the monolithic integration of a NIR sensitive photodetector with a visible LED.

The simplest device structure for an upconverter is a NIR photodetector and an LED sandwiched between two electrodes. There are two possible configurations for the device. Either it has the structure anode – photodetector – LED – cathode or it is stacked like anode – LED – photodetector – cathode. In the first case, the anode is designed to be hole injection blocking while for the second case, the cathode is designed to block the injection of electrons. This device design leads to a monopolar current flow upon application of an electric field. i.e. either only electrons flow through the device (Figure VIIIa) or only holes are transported across the device (Figure VIIIb). Since only one kind of charge carriers is present, no recombination will occur within the device. Thus, also no light can be generated and emitted in the LED layer. This state is considered the off state since no illumination with NIR light is provided.

Off state   **On state**
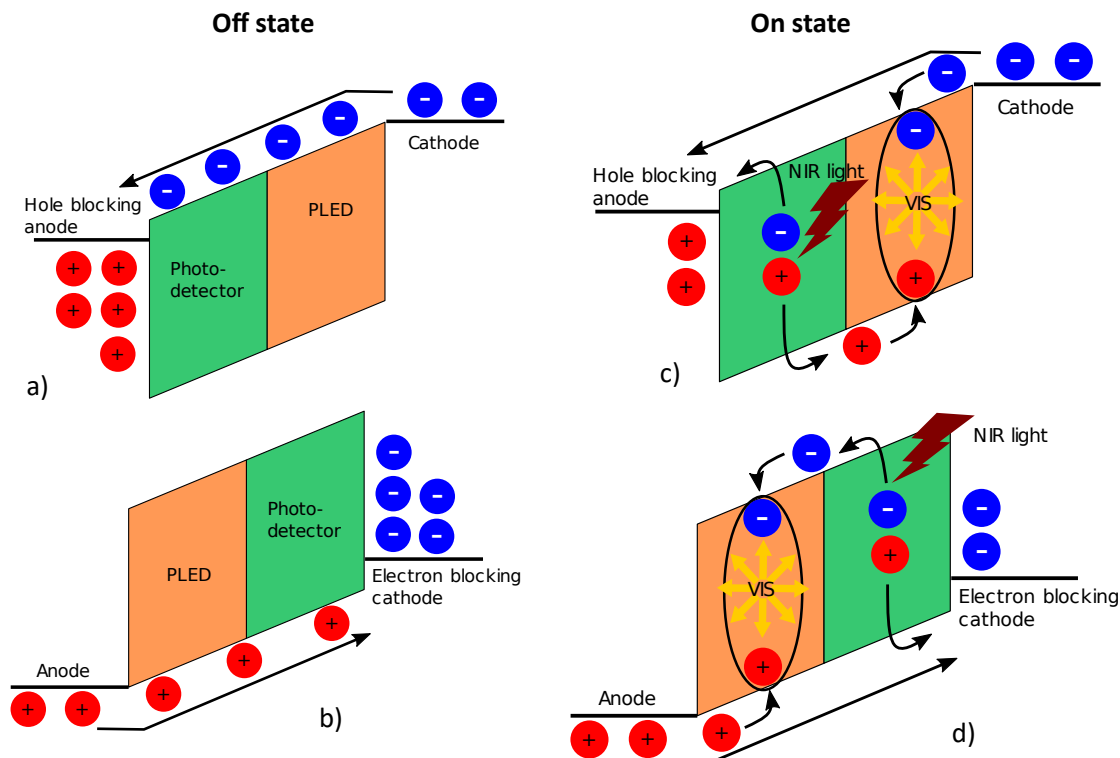
Figure VIII Simplest possible diagram for an all organic NIR-VIS upconverter device consisting of a photodetecting and a light emitting layer. a) configuration if holes are blocked and b) configuration if electrons are blocked. c) and d) show how the device operates under illumination for both configurations.

When the device in addition to the applied field also is illuminated with NIR light through a transparent electrode – the on-state of the device -, the NIR photons are absorbed in the photodetector layer which leads to a formation of an exciton. These pairs are separated into free electrons and holes which drift to the anode or cathode, respectively (Figure VIIIc, d)[49]. The energy required for this separation and drift is gained from the applied field and decay of photoexcited states.

Due to the generation of free electrons and free holes upon NIR illumination, both types of charge carriers are present within the device. Thus, recombination will occur. If this recombination occurs in the LED layer, it will lead to the emission of photons. The energy of the photon and thus the wavelength is determined by the band gap of the emission layer. This is generally chosen to be within the range of visible light, since this wavelength is easy to detect.

The in-coupling of NIR light and the outcoupling of VIS light requires careful engineering. Either both wavelength ranges need to enter (NIR) or exit (VIS) at the same electrode or at different electrodes. In the former case, the electrode needs to be transparent for NIR and VIS light and the layers of the device must have a narrow absorption spectrum. Assuming a transparent anode, this means for Figure VIIIc that the photodetector must not absorb in the VIS range. Otherwise, no visible light can exit the device. In the configuration of Figure VIIId, the emissive layer must not absorb in the NIR range. Otherwise, no NIR photons reach the photodetector and consequently no bound electron-hole pairs are generated.

If NIR and VIS enter or exit at opposite electrodes, the requirement for a narrow absorption spectrum of the layers is less stringent. However, it is difficult to fabricate a cathode which is transparent.

The upconverter device can be improved by optimization of the layer and interface morphology, by increasing the efficiency of photon absorption, exciton generation and separation in the photo-detector layer, as well as by improving charge transport, singlet exciton recombination and photon outcoupling in the emission layer.

One current research focus is to increase the photon-to-photon conversion efficiency and to extend the absorption wavelength range of the organic photodetector beyond 1100 nm, i.e beyond the band-edge of a silicon photodetector.

Chapter 1: Drift-diffusion study on thermally stimulated current

Scrutinizing thermally stimulated current transients originating from trapped charges in organic semiconductors: A drift-diffusion study

Camilla Vael [1,3] , Sandra Jenatsch [1]* , Simon Züfle [1] , Frank Nüesch [2,3]* , Beat Ruhstaller [1]

[1] Fluxim AG, Katharina-Sulzer-Platz 2, 8400 Winterthur, Switzerland

[2] Empa, Swiss Federal Laboratories for Materials Science and Technology, Laboratory for Functional Polymers, 8600 Dübendorf, Switzerland

[3] EPFL, Institute of Materials Science and Engineering, Ecole Polytechnique Fédérale de Lausanne, Station 12, 1015 Lausanne, Switzerland

* corresponding authors: frank.nueesch@empa.ch; sandra.jenatsch@fluxim.ch

Declaration of contribution

C.V. conducted all simulations and data analysis and was responsible for the majority of the manuscript's preparation.

1.1   Introduction

Organic semiconductors (OSCs) are an intriguing class of materials with unique physical properties like high mechanical flexibility[50], high absorption coefficient and tunability of its optical, electronic and dielectric characteristics[51][52]. Owing to their chemical versatility allowing to tune material properties and optimize processing, their abundance and low cost, they are viable candidates for a broad range of applications including solar cells, light-emitting devices, transistors, diodes and sensors[53]. By occupying a large share of the display market, organic light-emitting devices have evidenced that OSCs fully comply with the reliability requirements in this sector. Power conversion efficiency of organic photovoltaic devices is recently surging to competitive values up to 19%[54]. Although OSCs were identified as promising enablers for self-powered printed electronics, their stability and reliability still need to be further improved. Pinpointing the precise nature of degradation is a challenging task requiring the study of structural and morphological defects as well as chemical impurities[55]. Such defects always induce energetic disorder and hence produce electronic trap states impairing device performance by reducing charge carrier mobility, acting as recombination centres, changing the internal electric field distribution[56] and reducing the effective band gap of the material[29][57][58][31].

Albeit difficult to identify individually, electronic trap states have a large impact on the physical and chemical properties of OSCs. It is therefore possible to extract a number of parameters relevant to a particular trap distribution such as the average trap energy, energy distribution or density. There exists a wealth of different methods to probe the characteristics of trap states. A straightforward approach consists of using electrical measurement techniques, since they can also be applied to actual devices. Among others, such methods include steady state or transient current-voltage measurement [59], deep level transient spectroscopy [60], thermal admittance spectroscopy [61], the drain pulse method in field effect transistors[62], impedance spectroscopy[63]

or the transient photo-voltage method[64] which can easily be carried out as a function of temperature. Alternatively, optical methods like photothermal deflection spectroscopy (PDS) [65][66][41] and photoemission spectroscopy[67] may be used. It is also possible to use scanning probe methods like electric force microscopy which allows to measure trap characteristics with a high spatial resolution[68]. In some cases, X-ray diffraction methods can be used to investigate structural defects or interface roughness[69].

There are only a few electrical methods which measure trap states directly. One of these methods is thermally stimulated current (TSC)[3][70]. In this method, deep traps are filled at low temperature either by a voltage or light pulse. The trapped charges are subsequently released by linearly increasing the temperature and collected at the electrodes. This is a statistical process, which is controlled by a well-defined heating ramp allowing to access both thermodynamic and kinetic information. With TSC one is therefore able to probe the trap energy relative to the band edge, the number of traps (or trap density) as well as the capture and release dynamics (attempt-to-escape frequency). The basic requirement is that the filled trap states at low temperatures are inactive and cannot be released to the conduction states of the OSC, which are defined by the frontier orbitals of the OSC. Note that the current measured upon heating may not solely be due to released traps. Ions or reorienting dipoles as well as temperature-dependent charge injection may interfere with the signal originating from trap-released charges. These effects can however be accounted for by recording a so-called "dark" TSC transient, where the trap filling step is omitted, and by subtracting the dark TSC transient from the actual signal. Albeit relatively easy to measure, analysis of TSC data is not straight forward, since many physical factors have an influence on the shape of the TSC signal[71]. Hence, the interpretation of the measured signal relies on the application of a compact physical model allowing to fit an analytical formula to the experimental TSC data [72]. Every model, though, is subject to underlying basic assumptions, which are difficult to verify experimentally. It is therefore important to have a possibility for validating the models for a particular experimental system and to understand their application ranges.

In this study, we use a numerical drift-diffusion algorithm implemented in the commercial simulation software Setfos 5.1 to scrutinize the validity of the most popular analytical formula[73]. Among other input parameters, we first define the relevant trap characteristics for an OSC, which are then used to generate synthetic TSC data. We then use different analytical models to extract important trap parameters and compare the obtained values with the input parameters. We also analyze the limitations and validity range of the analytical formulas employed for TSC by varying various device materials and experimental parameters in the simulations. This approach provides further insights into the reliability of the models and guides the experimentalist on how to design the device and optimize the measurement procedures in order to determine the trap parameters with the highest possible accuracy. Eventually, we unravel unexplored features of TSC experiments such as the correlation between extracted charges and trap density as well as the fraction of non-extractable trapped charges

1.2   Analytical and Drift-Diffusion Models

There exists a plethora of models describing TSC, which were originally developed for inorganic semiconductors [74][75][76]. Very often, these models originate from the phenomenon of thermally stimulated luminescence and can be directly used to describe TSC by assuming temperature-independent mobility and a constant lifetime of the free carriers. For a comprehensive discussion, we refer to the book by R. Chen and Y. Kirsh [70]. While these models well describe semiconductors involving discrete trap levels and constant free carrier lifetime, they may not be appropriate for

disordered organic materials, where the thermally stimulated luminescence peak is observed at lower temperatures than the TSC peak[77]. Here we focus on the most common analytical expressions initially derived for inorganic semiconductors in order to shed light on their validity range in organic semiconductors. We treat the simple case of discrete trap levels and allow for the variation of free charge carrier lifetime as well as space charge.

1.2.1   Slow retrapping

In a typical TSC experiment, the active material containing electronic trap states is sandwiched between two electrodes and is heated at a rate β from a start temperature T_0 to a temperature $T= T_0 +\beta *t$, where t is the heating time. Simultaneously the current I_{TSC} originating from released charge carriers (for the sake of simplicity, we limit ourselves to electron traps) in the material is measured by means of an appropriate extraction field. The TSC signal is characterized by a peak, which is shaped by an exponential current onset due to thermally activated carriers at early times and by a fast decline at later times related to the limited availability of filled traps. Time t and temperature T are correlated by a linear relationship such that $dt=dT/\beta$. Based on a few assumptions that will be discussed below, R.R. Haering and E.N. Adams[74] derived an analytical formula which is commonly used to describe the complete peak shape as a function of T:

$$I_{TSC} = AFe\mu\tau n_{t,0}N_0 c_n exp\left(-\frac{E_t}{kT}\right) exp\left[-\frac{1}{\beta}\int_{T_0}^{T} N_0(T')c_n(T')exp\left(-\frac{E_t}{kT'}\right)dT'\right] \quad (1.1)$$

where A is the area of the electrode, F is the electric field, e is the elemental charge, μ is the charge carrier mobility, c_n is the electron capture coefficient, $n_{t,0}$ is the initial density of filled traps, τ is the lifetime of electrons in the transport states, N_0 is the density of transporting states, E_t is the energy difference between the transport energy level and the trap energy (trap depth) and k_B is the Boltzmann constant. Here, the capture rate coefficient c_n is used to describe trap dynamics. The latter is related to the attempt-to-escape frequency s or the capture cross section σ via $s = N_0 v_{th}\sigma = N_0 c$, where v_{th} is the thermal velocity of the charge carrier. Equation (1.1) is valid for the special case where recombination of electrons with hole centres is dominating recapturing by the trap. In the following, we will refer to this formula as "slow" for slow retrapping.

1.2.2   Initial rise

A simplification of equation (1.1) is frequently employed, which will hereafter be referred to as the "initial rise" method. In this approximation only the rising part of the I_{TSC} peak is considered, where the temperature T_0 is close enough to the temperature of the current onset. The integral of the second exponential term in (1.1) is then close to zero and can therefore be neglected. Thus, the formula reduces to:

$$I_{TSC} = AFe\mu\tau n_{t,0}N_0 c_n \exp\left(-\frac{E_t}{kT}\right) \quad (1.2)$$

Originally, this approach was developed by Garlick and Gibson in 1948 [78] for thermally stimulated luminescence.

1.2.3 T4max formula

By taking the derivative of equation (1.1) with respect to the temperature and only including the temperature dependence of c_n and N_0 explicitly after the differentiation, a simple formula for the slow retrapping case can be derived, relating the temperature at peak position T_{max} to the trap energy E_t:

$$E_t = k_B T_{max} \ln \left(\frac{T_{max}^4}{\beta} \right) \tag{1.3}$$

This formula will be referred to as "T4max" in the following. Originally, it was derived by Fang et al.[79] for the case of semi-insulating GaAs. Because of its simplicity, it is still widely used for the analysis of organic semiconductors and lead-halide perovskites [80][81].

For the case where retrapping and recombination have equal probability, another expression was derived by Garlick und Gibson[78]:

$$I_{TSC} = \frac{AFe\mu\tau n_{t,0}^2 N_0 c_n \exp\left(-\frac{E_t}{kT}\right)}{N_t \left[1 + \frac{n_{t,0}}{N_t \beta} \int_{T_0}^{T} N_0(T')c_n(T')\exp\left(-\frac{E_t}{kT'}\right)dT'\right]^2} \tag{1.4}$$

where N_t stands for the total density of trap states. We refer to this formula as "bimolecular" reflecting the fact that recombination depends on the product of the density of free electrons and holes. Above expressions are derived from rate equations and provide the temporal evolution of trap occupation when replacing time by temperature. Differently from equation (1.1) describing first order kinetics, equation (1.4) describes second order kinetics.

1.2.4 Extraction of trap site density

A straight forward method to extract the trap site density n_t from the TSC signal is by integrating over the current peak:

$$n_{t,recorded} = \int I_{TSC}\, dt \leq en_t V \tag{1.5}$$

where $n_{trecorded}$ is the apparent trap site density and V is the volume of the sample.

1.2.5 Models: underlying assumptions

It is important to recall the basic assumptions made in the derivation of the above expressions. First of all, the material is assumed to be homogeneous, allowing it to correlate the density of free charge carriers to the measured current density. Furthermore, the absence of space charge and minority charge carriers as well as a constant free carrier lifetime is presumed. Finally, the effect of contacts as well as any electric field dependence is neglected. It is also assumed that at any time during heating, the number of trapped charge carriers is larger than the number of free charge carriers in conducting states ($n \ll n_t$).[82] . This assumption is generally satisfied for undoped high resistivity materials since the intrinsic number of free charge carriers is small and $n \approx n_t\, e^{-E_t/kT}$ [70] (i.e the number of free charge carriers is always significantly smaller than the number of filled trap states when $\frac{E_t}{kT} > 10$ for the whole temperature range of the experiment). Also, it is presumed that $\frac{dn}{dt} \ll \frac{dn_t}{dt}$ [75], meaning that the free charge carrier density varies slowly over time as compared to the trapped charge carrier density.

1.2.6 Model used for drift-diffusion

Even though equations (1.1) to (1.5) allow to the extraction of important trap parameters such as E_t, c_n and n_t, the validity of these equations for a particular sample still has to be assessed. In particular, it is often difficult to verify experimentally that above base assumptions are fulfilled in a real device with electrical contacts. Variables such as the type of electrodes, the voltage applied or the device thickness may greatly influence the current transient of a TSC run. Also, a number of factors can lead to a reduction of the extracted charges and therefore to an underestimation of the traps present in the device[83]. For example, it may not be possible to fill all the traps at the start of the temperature ramp. Furthermore, the recombination of charge carriers released during the TSC experiment with free charge carriers of the opposite sign may depend on the applied voltage. A complementary modelling approach of TSC being able to bridge the gap between experimental parameters and the analytical approaches described above would therefore be highly valuable.

Drift-diffusion simulations allow us to take account of numerous experimental parameters in addition to those related to trap states. In this study, synthetic TSC data is simulated using a commercial drift-diffusion solver Setfos 5.1 by Fluxim AG[73] using representative input parameters of organic semiconductors. A typical sample for a TSC experiment consists of an organic semiconductor sandwiched between two electrodes. Even though further semiconducting layers may be applied to the device for optimizing charge extraction, we here consider the case of two metallic electrodes with variable charge injection barriers. In order to minimize charge injection from the electrodes under reverse bias condition, a small injection barrier from the anode to the highest occupied molecular orbital (HOMO) and from the cathode to the lowest unoccupied molecular orbital (LUMO) is chosen (see Figure 1.1a).

In order to be able to refer to a standard device, a parameter set corresponding to typical values for amorphous organic semiconductors is defined (base case, Table 1.2). Trap states with an energy of 0.35 eV below the LUMO energy level are homogenously distributed in the semiconductor with a density of $N_t = 1 \times 10^{17}$ cm^{-3}. The parameters used for the stack do not correspond to one specific material but are rather average values of typical materials. For the simulations, a value for the density of states of $N_{0,p} = N_{0,n} = N_0 = 1 \times 10^{21}$ cm^{-3} is used for both HOMO and LUMO transport levels.
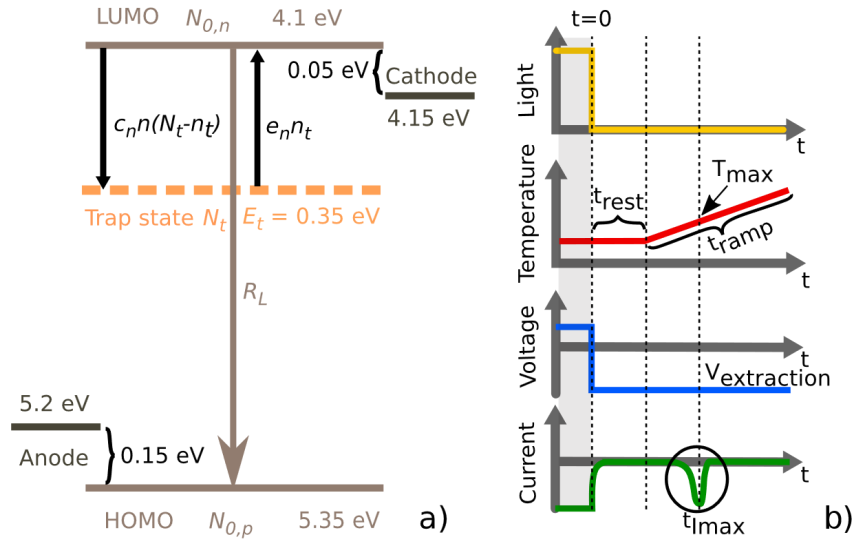
Figure 1.1 a) Simplified energy level diagram employed for this study. There are three distinct states where an electron may be found: HOMO, LUMO or in the electron trap. N0,x is the density of available states for holes (x=p) in the HOMO or electrons (x=n) in the LUMO, N_t is the total number of trap states at energy Et. Beside extraction, there are three processes considered in the model with corresponding rate constants. Namely electron capturing (c_n), electron emission (e_n) and band-to-band recombination (RL). b) Schematic of a TSC transient used for the generation of data by drift-diffusion. $V_{extraction}$ is the employed reverse bias voltage for the extraction of de-trapped charge carriers, t is the time with marked points at t=0 the start of the transient simulation, trest the time where superfluous charge carriers leave the device, tramp the time during which the temperature is increased linearly and tImax the time where the TSC peak reaches its maximum current. t_{Imax} can be converted to T_{max}, the temperature where the TSC peak reaches its maximum. Marked with the circle is the TSC peak.

The various electronic processes considered in this study are indicated in Figure 1.1a). As will be discussed below, electrons are present in the trap states before the temperature ramp of the TSC simulation starts. With increasing temperature, electrons can be emitted to the LUMO transport level at a rate e_n, from where they are either extracted at the cathode, trapped again with a capture rate c_n or undergo recombination with a hole in the HOMO level at the Langevin recombination rate R_L according to:

$$R_L = \eta\gamma\left(np - n_i^2\right), \text{with } \gamma = \frac{e(\mu_e + \mu_h)}{\varepsilon_0\varepsilon} \tag{1.6}$$

where η is the reduction factor (Langevin recombination efficiency), n is the number of free electrons, p is the number of free holes, n_i denotes the number of intrinsic charge carriers in the material, γ is the Langevin recombination constant, ε_0 is the vacuum permittivity, ε is the relative permittivity of the material and $\mu_{e,h}$ the mobility of electrons and holes, respectively. This condition is quite different from the basic model related to equations (1.1) and (1.4) since no static recombination centres are present in the drift-diffusion model and no constant lifetime can be defined. For simplicity, Shockley-Read-Hall (trap-assisted) recombination is not considered in the base case.

TSC is simulated in two steps as displayed schematically in Figure 1.1b) and corresponds to a typical experimental procedure. Traps are first filled by irradiating the sample with light (at a wavelength of 500 nm) at a temperature of 50 K (grey-shaded area). The computation is carried out for the steady state at an applied forward bias of 1.05 V (flat band condition) and ensures that all of the traps are filled and the current is zero. In a second step, a transient simulation is carried out using the output of the initial steady state calculation as an initial step. There are two distinct parts in the transient simulation. During the first part, the device is kept at T_0 = 50 K while an extraction voltage of -2 V (reverse bias) is applied and the illumination is turned off. During this time, the

superfluous charge carriers generated by the irradiation in steady state are extracted while the traps remain filled. The extracted charge carriers are recorded as a rapidly decaying current. After this equilibration step at $t=t_{rest}$, the temperature is linearly increased with a heating rate β of 10 K/min for the time t_{ramp}=1680 s until it reaches 330 K. During the temperature ramp the trapped charge carriers gain enough energy to leave the trap and are recorded as a current upon extraction. The current caused by the de-trapped charges reaches a maximum at T_{max} before it declines due to the limited supply of trapped charge carriers.

In the base case drift-diffusion simulation, we consider N_0, c_n and μ to be independent of temperature. For inorganic materials, a temperature dependence for N_0 and c_n of $T^{3/2}$ and $T^{1/2}$, respectively, is generally considered, while temperature-independent carrier mobility is adopted in advanced TSC models. According to (1.1) this contribution would result in a temperature dependence of T^2, which is often neglected given the fact that the exponential temperature dependence induced by the activation term dominates over the power law dependence[84][85]. The same argument can be invoked for the carrier mobility in inorganic semiconductors, which also shows a power law dependence due to impurity and lattice scattering[86]. Similarly, crystalline organic semiconductors also show a linear or power-law dependence of mobility with temperature, indicative of band-like transport[87][88]), which justifies the simplification of neglecting temperature dependence of the above parameters in the TSC experiment. However, disordered organic semiconductors often exhibit thermally activated transport behaviour where mobility increases exponentially with temperature [89][90]. Therefore, the impact of temperature-dependent carrier mobility is also tackled briefly in this work (S1.1). Furthermore, to assess the sensitivity of trap parameter extraction on mobility, we analyze the simulated TSC curves for a large variation of electron mobilities.

1.3   Results

1.3.1   Fitting synthetic data
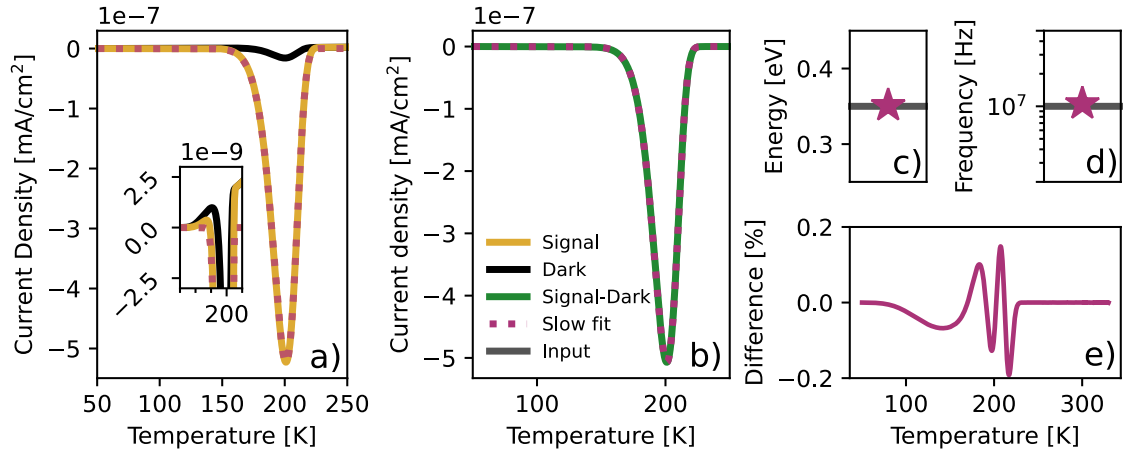
Figure 1.2 a) TSC data from drift-diffusion simulations for actual (yellow) signal and dark current (grey). For comparison the TSC peak from equation (1.1) (slow fit, purple) is indicated. Inset: close-up of the current displaying the effects of injection from the electrodes. b) fit using equation (1.1) (purple) to the dark current subtracted data (green). c) and d) values for trap energy and attempt-to-escape frequency, respectively, extracted from the fit using equation (1.1). Grey line denotes the input value. f) difference in % between the dark current subtracted DD data and the full curve fit using equation (1.1).

A typical TSC simulation, hereafter called the base case, is displayed in Figure 1.2a for a 100 nm thick organic film incorporating a trap density of 10^{17} cm^{-3} with an electron trap depth of 0.35 eV

below the LUMO level. The device is sandwiched between two electrodes and biased at -2V during a temperature increase from 50 K to 330 K at a heating rate of 10 K/min (see Table 1.2, Table 1.3 and Table 1.4 for all other input parameters used in the simulation). In order to simulate an actual TSC experiment and to provide synthetic TSC data for fitting to the analytical models, the dark current (where the trap filling step has been omitted) is subtracted from the TSC signal obtained with initially filled traps (Figure 1.2a). Interestingly, the dark current presents a clear signal contribution in addition to a small positive feature. As will be discussed below, this is due to the release of electrons from traps close to the electrode.

Fitting the analytical equations (1.1) and (1.4) to the TSC data is not trivial since I_{TSC} varies over several orders of magnitude - large values are weighted more in the least square approach used here. However, the most relevant for the extraction of trap parameters is the peak itself with the largest current values. Here we use the Levenberg-Marquardt algorithm (python library lmfit) and obtain R^2 values above 0.9998 when the extracted trap parameters match the input parameters (the goodness of the fits are above 0.998 in the other cases). The fit of the background subtracted drift-diffusion data to equation (1.1) and its residue are displayed in Figure 1.2b) and f), respectively. Note that the residue is calculated as the difference between the synthetic drift-diffusion data and the curve fit using the analytical equations, normalized by the maximum current value. The extracted trap energy (Figure 1.2c) and the attempt-to-escape frequency (Figure 1.2d) match the input values of 0.35 eV and 10^7 Hz remarkably well. Theoretically, it is also possible to calculate the trap density from the fit. However, we will refrain from it since the parameter is one factor in the product of seven other parameters, which would first need to be determined individually in other experiments. More straightforward is the integration of I_{TSC} according to (1.5) yielding a trap density of $4.8 \cdot 10^{16}$ cm^{-3} which compares to about half of the input density of 10^{17} cm^{-3}.

1.3.2   Parameter variation

In order to assess the accuracy of the other commonly used expressions and to probe the sensitivity of the fits to the analytical equations, a series of simulations are performed where one parameter in the base case is varied, while keeping the other parameters fixed. The extent of the change depends on the range of physically meaningful values and the range of values where the numerical calculation remains stable. Most relevant are those parameters describing the characteristics of the traps namely the trap energy, trap density and the capture rate. Also important are parameters which can easily be changed by the experimentalist such as the thickness of the semiconductor layer, the heating rate and the applied extraction voltage. The most important trap parameter is its energy, which also has the largest influence on the position of the peak. This is already visible in the analytical formulas for the TSC curve where trap energy enters as an exponent of an exponent. The extracted trap energies are presented in Figure 1.3 for a range of single parameter variations, while the simulated TSC curves are shown in the supplementary information (S1.3).

1.3.2.1 Trap energy
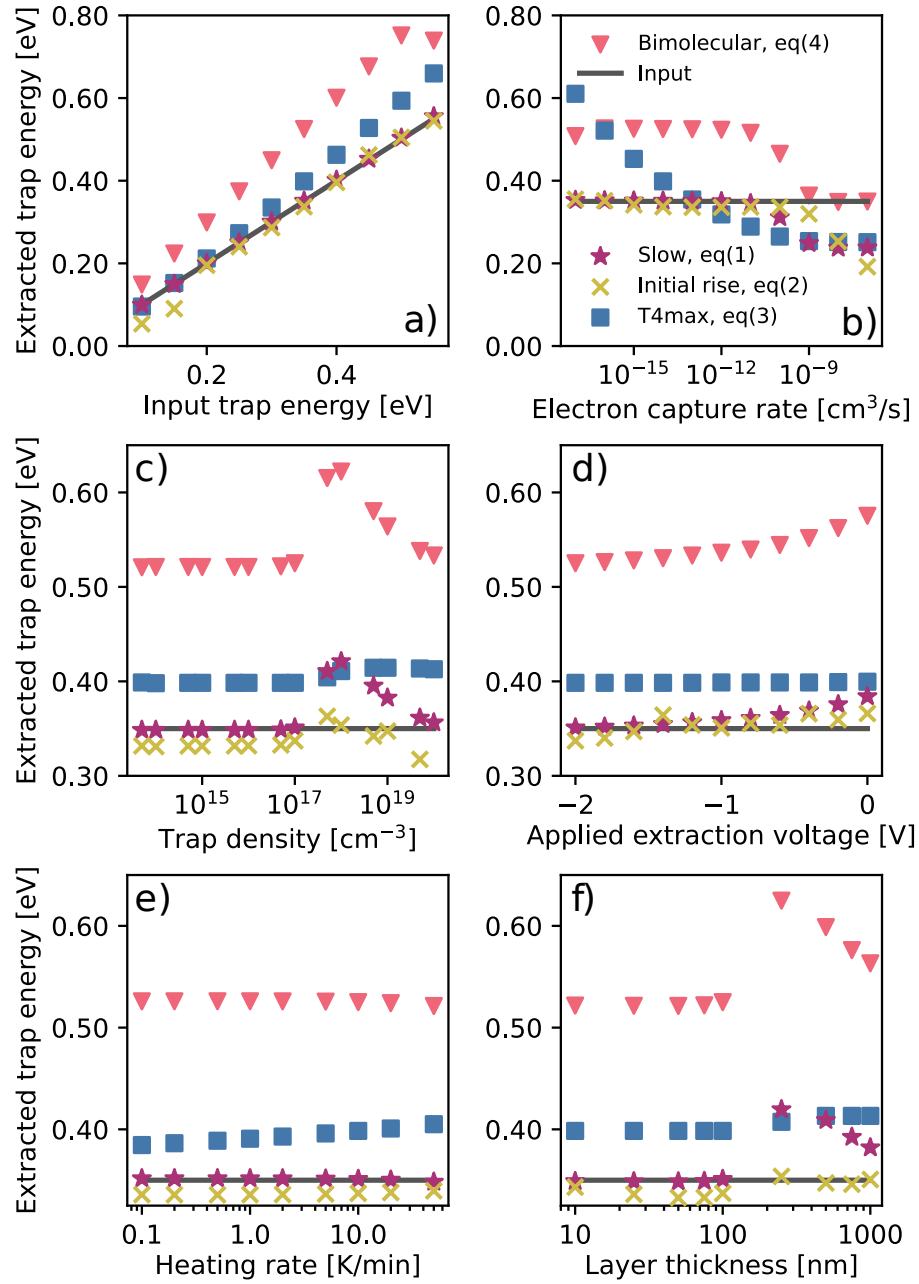
Figure 1.3 Electron trap energy determined by diverse TSC formulas for different input values in single parameter variation series. The following input parameters were changed with respect to the base case: a) trap energy, b) capture rate, c) trap density, d) extraction voltage, e) heating rate and f) thickness of the semiconductor film.

Figure 1.3a shows the extracted trap energy from the fits of equations (1.1) to (1.4) to synthetic TSC data generated for trap energy input values of 0.1 to 0.55 eV. Impressively, fits with equation (1.1) yield values, which lie within 1% of the input trap energy. At low trap energies, the "initial rise" method (1.2) provides deviating values. This is mainly due to the fact that the TSC peak occurs close to the start temperature of the ramp. The relevant part of the peak is therefore not fully accessible which leads to this deviation. For trap energies of 0.2 eV and above, equation (1.2) provides the correct trap energy within an error of 5%. The "T4max" equation (3) gives values for

the trap energy that is close to the input value for low trap energies (<0.25 eV). However, for increasing trap energies, the extracted value starts to deviate systematically. This is an indication that the temperature dependence of the T4max formula may be stronger than the temperature dependence obtained from the drift-diffusion simulation. The "bimolecular" equation (1.4) does greatly overestimate the trap energy by 50% for trap energies between 0.15 and 0.5 eV. A large deviation is expected since the capture rate for the base case is in the slow retrapping regime. It is possible to measure traps with energies higher than 0.55 eV by heating the device to temperatures above 330 K. However, at such elevated temperatures, other effects such as morphological changes within the layers may occur in organic semiconductors, which can mask the effects originating from de-trapping of charge carriers. We therefore refrained from simulating temperatures higher than 330 K.

By using a higher extraction voltage in the reverse bias, the accuracy of the extracted trap energy using (1.1) increases clearly (Figure 1.3d). The same tendency can be observed in the case of equation (1.4). However, since we are in the limit of slow retrapping, as discussed above, the trap energies are systematically too high (by 0.18 eV for an extraction voltage of -2V). Fitting using equation (1.3) provides an energy of 0.4 eV independent of the applied extraction voltage. The values extracted using (1.2) are within 5% of the input trap energy with the tendency to underestimate trap energy at high extraction voltages and to overestimate it at low extraction voltages.

The range considered for the variation of the capture rate s deserves some more explanation. In the case of inorganic semiconductors, values for $s \approx 10^{11} - 10^{13}$ Hz are commonly used[91][92] which translates to capture rates in the range of $c_p \approx 10^{-10} - 10^{-12}$ cm$^{3/s}$ assuming a density of states of 10^{21} cm^{-3}. For organic semiconductors Carr *et al.* found values ranging from 10^8 Hz to 10^9 Hz for P3HT:PC60BM, PTB7:PC70BM, and PCDTBT:PC70BM[85]. Other studies reported values for perovskite materials of 10^9 to 10^{11} Hz[93][94]. However, also 5x10^{12} Hz for pentacene thin-films and 10^5 Hz for sexithiophene-based transistors[95] have been reported. These numbers correspond to capture rate coefficients spanning a broad range of 1x10^{-8} cm$^{3/s}$ to 1x10^{-16} cm$^{3/s}$ assuming a density of states of 10^{21} cm^{-3}. Physically, attempt-to-escape frequency can be understood as the rate at which a trapped charge carrier interacts with molecules in its surrounding and can be estimated as a first approximation to be about an order of magnitude smaller than the relevant vibration frequency. This amounts to a capture rate of 1x10^{-14} cm$^{3/s}$ for organic materials as opposed to 1x10^{-8} cm$^{3/s}$ for inorganic materials)[70]. While this accounts for the choice of the capture rate coefficient for the base case in this work, there may exist traps which are not tightly coupled to their surroundings or have a small transition probability from the trap to the LUMO. Both would lead to a lower capture rate coefficient. On the other hand, traps with high capture rate coefficients may exist. This is for example possible for traps that are charged when they are empty.

Capture rate variation shows a quite consistent picture. For our set of parameters, trap energies extracted for capture rates higher than 1x10^{-8} cm^{-3}/s can be described by the bimolecular formalism (1.4) while accurate trap energies at capture rates lower than 1x10^{-11} cm^{3}/s are well described using the slow retrapping rate according to equation (1.1). This is confirmed by the fits to synthetic TSC data (Figure 1.3b). An intermediate capture rate regime between 1x10^{-8} and 1x10^{-11} cm^{3}/s is indeed observed, where neither formalism will provide good values for the trap energy. Similarly to the slow retrapping formalism, equation (1.2) - which is derived from (1.1) - shows the same deficiencies at higher capture rates. Extraction of the trap energy from equation (1.3), however, is strongly dependent on the capture rate of the trap. Only for a value of 1x10^{-13} cm^{3}/s, this formula determines the trap energy with good accuracy. Indeed, the T_{max} method is free from

any parameter related to trap dynamics and therefore cannot be used in a meaningful way without knowing the capture rate.

When looking at the influence of input trap density, equation (1.1) gives accurate values, however for high trap densities (above 1×10^{17} cm^{-3}) an overestimation of the trap energy is found (Figure 1.3c). The deviation occurs due to a distortion in the peak shape (S1.3 d, S1.5c and d, which also similarly affects the fits using equations (1.3) and (1.4). Both fits, in particular equation (1.4), overestimate the trap energy systematically, as discussed before. Note that equation (1.2) is rather independent of input trap density and slightly underestimates trap energy.

An important experimental parameter for TSC is the heating rate. There is a trade-off between using a high heating rate to obtain a larger signal and a low heating rate to guarantee a uniform device temperature. Our drift-diffusion model considers a constant temperature within the device and does therefore not allow accounting for the latter effect. All but the Tmax method (1.3) show almost constant trap energy when the heating rate is varied (Figure 1.3e).

Film thickness too is an important experimental parameter, as thicker devices can contain more (homogeneously) distributed traps and can therefore lead to a larger, easier detectable current signal. Here, the film thickness is varied from 10 nm to 1000 nm (Figure 1.3f). Interestingly, equation (1.1) shows a clear deviation from the input trap energy for thicknesses larger than 100 nm. This is not the case for equation (1.2) based on the initial rise of the TSC curve. Equation (1.4) also shows a strong variation at larger film thicknesses. As we explain in the supplementary information (Figure 1.5e and f) this comes from the fact that equations (1.1) and (1.4) suffer from the peak shape modification due to charge transport and extraction as well as recombination, while the initial rise method (equation 1.2) is not impacted by recombination effects due to the low concentration of de-trapped holes and electrons at the onset temperature of the TSC signal.

Since the base case uses a rather low capture rate coefficient of 10^{-14} cm^3/s, trap energies extracted from equation (1.4) derived for fast recapturing are strongly deviating from the input energy using most parameter settings in Figure 1.3.

1.3.2.2 Attempt to escape frequency

It is possible to check the validity of capture rate values by generating TSC curves with different input values and extracting the capture rate. Figure 1.4 shows the attempt-to-escape frequency (for short: escape frequency) as a function of electron capture rate. As shown in Figure 1.4, fairly accurate values for the extracted escape frequency are obtained using equation (1.1) within the limit of slow retrapping, while it is underestimated by orders of magnitude in the fast-retrapping regime. In other words, the attempt-to-escape frequency is determined with higher accuracy for all cases where also the determination of the trap energy is correct, i.e. when the assumption in the derivation of (1.1) is fulfilled. This finding doesn't change substantially when taking the input trap energy as comparted to the case where the trap energy is extracted from the fit, together with the escape frequency. Using equation (1.4) for fitting the escape frequency does not provide correct values for nearly all input electron capture rates, even when the input trap energy is taken. This again highlights the shortcomings of equation (1.4) to extract decent trap parameters from the simulated data.
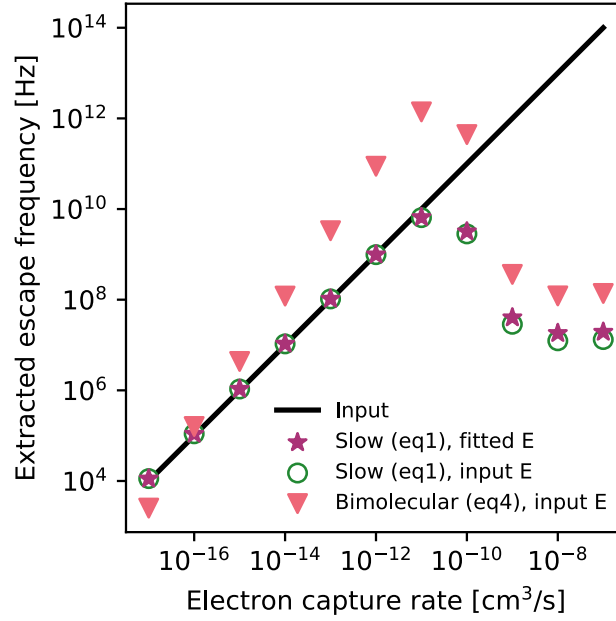
Figure 1.4 Attempt-to-escape frequency s calculated from fits using equations (1.1) and (1.4) for electron capture rates c_n varied from 10^{-17} to 10^{-7} cm³/s. The trap energy was taken as an input parameter for the calculation of the attempt-to-escape frequency (triangles, circles). For comparison, the attempt-to-escape frequency was also calculated using the trap energy from the fit (stars).

1.3.2.3 Trap site density

After analysing the reliability of the trap energy and the capture rate, we now turn our attention to the third trap parameter: the trap site density. A major advantage of drift-diffusion simulations is the possibility to obtain the charge carrier density as well as the electric potential profile at each point in time during the signal. This allows us to gain more insight into the underlying processes of the TSC experiment. Here it is used to analyse the trap distribution at different points in time and compare it to the simulation input as well as to the calculated trap density using equation (1.5). The number of extracted charge carriers is generally expected to be smaller than the number of trap states due to incomplete trap filling or emptying and the recombination of charge carriers.
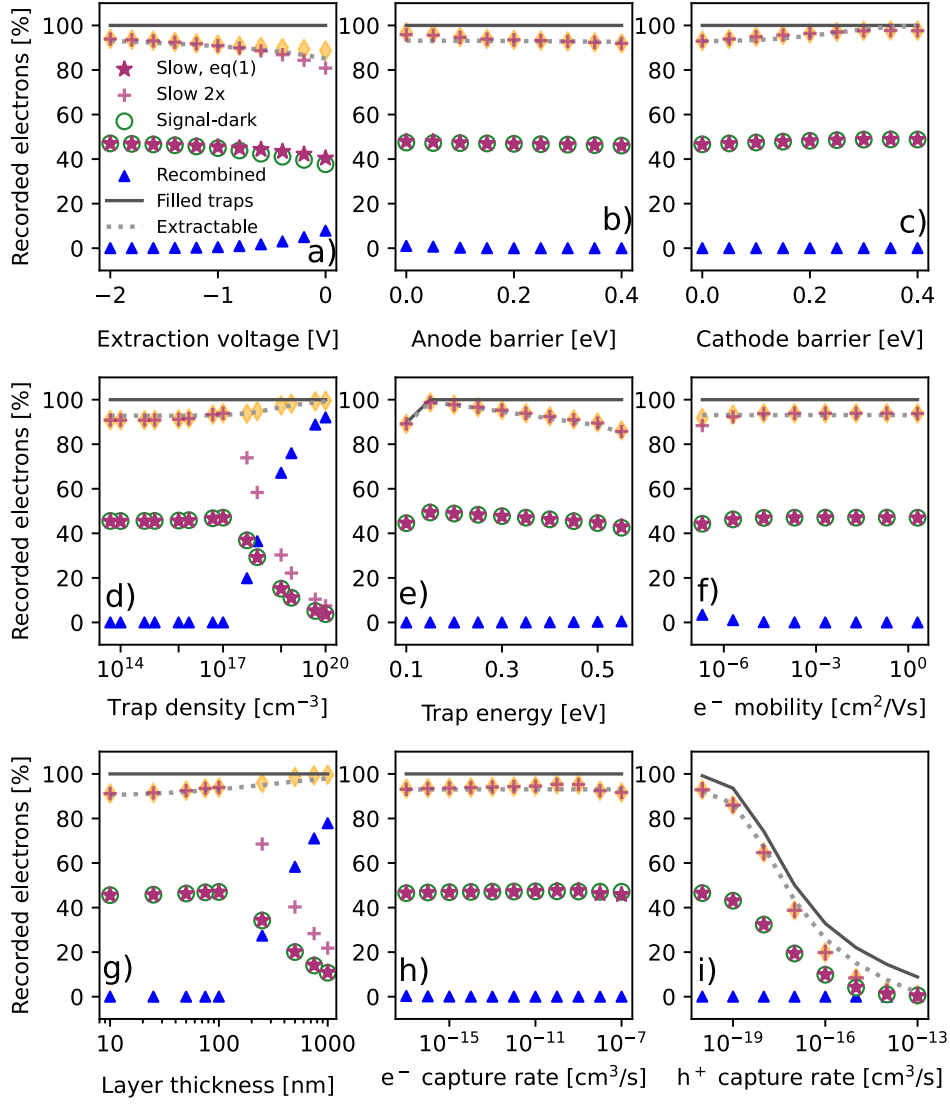
Figure 1.5 Percentage of recorded electrons originating from traps as a function of a single parameter variation. The dark grey solid line indicates the fraction of filled traps at the start of the temperature ramp. The grey dotted line denotes the percentage of extractable electrons. The difference between the filled traps line and the extractable line corresponds to the percentage of electrons remaining in the electron traps at the end of the ram. Signal-Dark corresponds to the trap density in percent extracted from the simulated TSC where the dark current was subtracted. Slow fit is the trap density extracted from the integral of the fit to the Signal-Dark TSC curve using equation (1.1). For electronic reasons, the TSC peak attributes only $e_{nt}/2$ of the traps. So, the values received from the integral on the fitted curve were doubled (slow x2). The percentage of recombined charge carriers is displayed as blue triangles. The sum of slow x2 and recombined is shown as yellow diamonds (total). Displayed are the result for following variation series: a) extraction voltage, b) hole injection barrier at the anode, c) electron injection barrier at the cathode, d) trap density, e) trap energy relative to the LUMO, f) electron mobility (different constant values), g) thickness of the semiconductor layer, h) electron capture rate and i) hole capture rate of the electron trap (leading to Shockley-Read-Hall recombination)

We discriminate between input trap state density N_t (100% mark), initially trapped charge carriers (grey solid line), extractable (grey dotted line) and recombined charge carriers (blue triangles) as well as recorded charge carriers which we obtain from integrating the TSC signal or the fit to it using (1.1) (Figure 1.5). The value for extractable charges is derived from the difference of trap occupation at the start and the end of the simulation. Trap occupation is calculated at every 0.5s and is exported every 10 s for each position in the device (0.497 nm resolution) as part of the drift-diffusion simulation. Carriers which contribute to the TSC current are obtained by integrating the dark current corrected TSC peak (green circles) and similarly for the fit using equation (1.1) (purple

stars). In the base case, trap states with an energy of 0.35 eV, a homogeneous density of 10^{17} cm^{-3} and a capture rate coefficient of 10^{-14} cm$^{3/s}$ are entirely filled at the start of the temperature ramp at t=t$_{rest}$ in the TSC experiment. Under the strong extraction field of -2V, nearly all de-trapped charge carriers will be recorded. For a homogeneous trap density, it has been shown that the recorded charge carriers correspond to en$_t$/2 (for a thorough investigation of this factor and the underlying physics refer to Hawks et al. [96]). For this reason, we multiply the values obtained from the integral of the TSC curve by a factor of 2 (purple plus, Figure 1.5) in order to get more accurate values for the trap density. This procedure may not be accurate for an arbitrary trap distribution producing a space charge, which can drive the charges to both electrodes. Also, recombination will be enhanced in those areas of the film where the local electric field is low. In all those cases, the number of recorded charge carriers may be considerably lower than en$_t$/2. Since there are only few free electrons other than the de-trapped electrons present in the device, the recombination signal is limited by Langevin recombination of de-trapped electrons with holes. This can be checked by comparing the sum of the recombined charge carriers and the recorded charge carriers (corrected by a factor of 2, "total") with the number of extractable charge carriers (see Figure 1.5). If the first number is higher than the latter, charge carriers other than the de-trapped electrons either recombined or were extracted.

For all parameters varied in Figure 1.5, trap filling at t=t$_{rest}$ is almost always complete. A trap filling of 100% corresponds to a filled trap density of 10^{17} cm^{-3}, except in Figure 1.5d, where 100% corresponds to the respective value of the input trap density being varied in this experiment. There are two exceptions, where the fraction of filled traps is smaller than unity. The first concerns shallow traps (Figure 1.5e), the second considers Shockley-Read-Hall recombination (Figure 1.5). A further finding is that the proportion of extractable charge carriers is generally smaller than 100%. In most cases, this proportion exceeds 90%, underlining the suitability of the TSC technique to determine the number of trap states quantitatively. For large cathode injection barriers (Figure 1.5), small trap energy (Figure 1.5e) and large film thicknesses (Figure 1.5g), the proportion of extractable charge carriers comes even close to unity. This hints to a particular effect at the cathode interface, which will be discussed below. Finally, Langevin recombination is negligible for a large range of parameters and manifests itself only for large input trap densities (Figure 1.5d) as well as thick semiconductor layers (Figure 1.5g).

It is interesting to analyze the prediction of trap density provided by the TSC experiment, i.e. by integrating the TSC signal and multiplying it by a factor of 2, as reasoned above (purple plus). For a very large range of parameters, the fraction of extractable charges is extremely well reproduced. Some deviation is observed for low extraction voltages (Figure 1.5a) and very low electron mobilities (Figure 1.5f), while substantial differences are observed for high trap densities (Figure 1.5d) and film thicknesses above 200 nm. The latter two cases are clearly related to a high recombination of released electrons with holes in the device. These observations provide valuable input to the experimentalist in order to optimize experimental conditions and interpret the measured data adequately.

1.4   Discussion

Among the various analytical expressions (1.1) to (1.4), commonly used to extract trap parameters from TSC data, equation (1.1) derived for slow retrapping clearly provides the best match to the input parameters for a large variation of input parameters. For the base case, trap energy and capture rate present an excellent match (better than 0.3% for trap energy, better than 6% for capture rate), and for single parameter variations (while keeping all other parameters Table 1.1) a

good match is obtained for the extracted trap energy (first value in bracket) and capture rate (second value in bracket) when varying the following input parameters: trap energy from 0.1 to 0.55 eV (< 1% / < 23% deviation), the extraction voltage from -2 to -1V (< 2.5% / <65% deviation), the capture rate from 10^{-17} to 10^{-11} cm$^{3/s}$ (<1.5% / < 35% deviation), the trap density from 10^{13} cm^{-3} to 10^{17} cm^{-3} (<0.5% / <10% deviation), the heating rate from 0.1 to 50 K min^{-1} (<0.5% / <13% deviation), the film thickness from 10 to 100 nm (< 0.5% / <9% deviation). The larger deviation for the capture rate can be attributed to a) numerical imprecisions originating from the finite number of terms used to approach the integral in formula 1, b) the uncertainty from the other parameters involved in the determination of the capture rate from the fit parameter $B = \frac{N_0 c_n E_t}{\beta k_B}$, where E_t was set from the fit to the simulated data. The obtained value is usually in the same order of magnitude as the input value which is sufficiently accurate.

This excellent correspondence is not obvious given the fact that the underlying physical model of equation (1.1) only consideres conductivity and implies the absence of space charge and a constant electric field throughout the film. It is therefore interesting to analyze whether the latter conditions would be fulfilled in the drift-diffusion model, where space charge is naturally implemented, implying electric field variation throughout the sample. Figure 1.6 indicates the electron densities of free electrons and holes as well as the density of trapped electrons at the various temperatures of a TSC experiment. In the base case using an extraction voltage of -2V (Figure 1.6a), the high trap density of 10^{17} cm^{-3} at the start of the temperature ramp (50 K) cannot be compensated by holes. The initial space charge due to trapped electrons is gradually depleted as temperature is increased reaching a low level of 10^5 cm^{-3} at the end of the temperature ramp (330 K). Even though the hole density rises, it is orders of magnitude lower than the electron density throughout most of the device layer. The substantial space charge due to trapped electrons gives rise to a linearly increasing electric field, which converges to a constant field once the traps are emptied (Figure 1.6). The drift-diffusion simulation therefore does not satisfy the hypotheses of a constant electric field or the postulated absence of space charge and minority carriers. Equation (1.1) also stipulates that the number of trapped charge carriers is larger than the number of free charge carriers in conducting states ($n \ll n_t$). This assumption is indeed verified throughout most of the sample thickness for tempertures where Et/kT>10. Close to the cathode, the condition is not fulfilled (Figure 1.6d,e). Eventually $\frac{dn}{dt} \ll \frac{dn_t}{dt}$ is also presumed for the derivation of equation (1.1), which is fulfilled for the temperature range where the trap is active, but is not yet at equilibrium with the conducting states.

The analysis of charge carrier density reveals an interesting feature close to the electrode interfaces. At the cathode, diffusion of electrons into the semiconductor inhibits emptying of traps even at high temperatures. Active electron trap states ($E_t < k_B * T_{max}$) are at equilibrium with free electrons in the LUMO and thus are partially filled. The percentage of trap occupation n_t/N_t in steady-state depends on trap energy E_t, trap density N_t, temperature T and the free electron density n as (see supplementary information):

$$n_t/N_t = 100 \cdot n/\left[n + \left(N_{0,n} - n\right) * \exp(-E_t/k_B T)\right] \qquad (1.7)$$

The density for free electrons in the LUMO close to the cathode reaches up to $1 \cdot 10^{19}$ cm^{-3} at 330 K (Figure 1.6d) which is sufficiently high to ensure that traps in this vicinity are nearly completely filled during the whole TSC run. This explains why the fraction of extractable electrons from traps does not reach unity (see Figure 1.5). At a lower extraction voltage (Figure 1.6e) this phenomenon is even more pronounced, since the free carrier density spreads over a larger width at the cathode side. For higher trap energies the number of extractable charge carriers close to the cathode

decreases, mainly caused by the increased trap occupation ratio. Increasing the thickness of the device brings the fraction of extractable trapped charges closer to unity, since the cathode effect now is less important with respect to the bulk (Figure 1.5g). Note that the small peak in the dark current observed in Figure 1.2a) is also due to de-trapping of electrons from traps close to the cathode which are filled due to diffusion from the cathode and emptied upon reaching temperatures favourable for de-trapping.

The diffusion of electrons from the cathode, however, can also be reduced by employing a higher injection barrier (Figure 1.5c). This could indeed be a possibility to increase the number of extractable electrons. On the anode side, holes enter the semiconductor, but present a small density at high extraction voltage (Figure 1.6a). At lower extraction voltage, however, holes can enter the device more easily and compensate trapped electrons over a large region of the film (Figure 1.6b) which leads to a screening of the electric field or even to an inverted field in certain regions of the device (Figure 1.6h). This leads to increased recombination as seen in the decrease of collected charge carriers (Figure 1.5a). Efficient recombination also occurs at large device thicknesses due to the small extraction fields (Figure 1.5g). Finally, the situation of a very high trap density ($5 \cdot 10^{18}$ cm^{-3}) is analyzed. In this case free holes can perfectly compensate trapped electrons in the film at low temperature (Figure 1.6c and f). During the release of traps during heating up, electrons therefore easily meet a hole and recombine which drastically reduces the fraction of charge carriers extracted at the electrodes (Figure 1.5d). This may explain why the fit using equation (1.1) overestimates trap energy and underestimates trap density. Another factor potentially reducing the number of electrons present in traps is the trap-assisted SRH recombination (Shockley-Read-Hall recombination). During the TSC run, the number of free holes is too small for significant SRH recombination to occur. However, during the trap filling stage before the TSC run, SRH recombination may decrease the fraction of filled traps so that $n_t < N_t$. Consequently, the number of extracted electrons is smaller (Figure 1.5i).

The initial rise method using equation (1.2) also provides excellent parameter extraction for the base case. Furthermore, this method is very stable with respect to parameter variation, almost on par with equation (1.1) from where it is derived. Since only the onset of the TSC curve is used, the fitting range of the onset current is quite critical. As shown for the base case, injection of charge carriers at the onset temperature of consecutive de-trapping can even lead to positive current signal (inset Figure 1.2a) which may have an influence on the curve fit using equation (1.2), particularly at lower extraction fields. Moreover, the value for the trap energy extracted with the initial rise formula strongly depends on the amount of data and the part of the curve used for the fit (see S1.4)

As illustrated in Figure 1.3d), the initial rise method underestimates the trap energy at high extraction fields, while overestimating it at lower fields. This comes from the varying contribution of holes diffusing into the device from the anode (Figure 1.6b). When the activation temperature of the trapped electrons is reached, the recombination of charges sets in, reducing the current that would be expected without the presence of holes (see S1.5S1.5 TSC simulation broken down into contribution from holes (red) and electrons (sky blue). The recorded current signal is denoted by a black solid line, while the calculated, ideal TSC peak is displayed with a black dotted line. The recombined charge carriers are displayed as a recombination current by a grey line. In a) the base case is displayed. In b), the extraction voltage was changed to 0V, while in c) and d) the trap density was changed to 1x1018 and 1x1019 cm-3, respectively. In the last row, the current contribution for 250 nm (e) and 500 nm (f) thick active layers are displayed. All parameters which were not specifically mentioned correspond to the parameters used in the base case. To better resolve the

overlapping lines in a), the lines denoting the recorded TSC peak (black) and the electron contribution (sky blue) are fattened.). Eventually, hole and electron currents with current peaks at different temperatures provide a net contribution to the TSC signal. Due to these combined effects, the TSC curve is distorted and Tmax is shifted to higher temperatures, which leads to an overestimation of the trap energy.

Interestingly, the initial rise method is rather insensitive to the semiconductor thickness, while the underlying equation (1.1) shows a clear overestimation of the trap energy (Figure 1.3). This is due to the fact that albeit small, the current onset will not be inhibited by the low field regions that are present through a large part of the device at the onset temperature. On the other hand, a large part of trapped charges will only be collected at higher temperatures, once an appreciable electric field has been established throughout the device.

Fitting equations (1.3) to the synthetic TSC data from drift-diffusion is rather problematic. For the base case, the prediction of trap energy depends very much on the power law dependence of temperature which depends ultimately on the temperature dependence of the capture rate, the density of states and the thermal velocity of the charge carriers (see derivation of T4max formula in the SI). Here, we assume all parameters to be independent of temperature, which would suggest T_{max}^2 dependence in the logarithm of equation (3): $E = k_B T_{max} \ln\left(\frac{T_{max}^2}{\beta}\right)$. As is shown in S1.2, however, the power law of T_{max}^3 provides the closest fit to the synthetic data. Also, we note that there is a huge deviation from the input trap energy upon variation of the capture rate. Therefore, the use of equation (1.3) is only meaningful if the other parameters such as the capture rate and its temperature dependence as well as the temperature dependence of the mobility and density of states have already been determined.

Extracting trap parameters from equation (1.4) shows rather large discrepancies with resepect to the input parameters used for the drift-diffusion calculation of the base case (see Figure 1.3 and Figure 1.4). This is indeed consistent with the underlying model, stipulating a capture rate comparable to the recombination process. In drift-diffusion simulation the more realistic case of charge extraction plays a domint role at high extraction fields. The underlying mechanisms of the models are therefore radically different. One may argue that extraction may be comparable to the capture rate and therefore substitute for recombination in the classical model (equation 4). However, the model only provides accurate prediction of trap energy for capture rates larger than 10^{-9} cm^3/s, which is out of range for most organic semiconductors. For these reasons, equation 1.4) should not be used to fit TSC curves obtained for organic semiconductors.

Eventually it is interesting to verify the effect of neglecting temperature dependent charge carrier mobility, since charge carrier transport by a hopping mechanism leads to an exponential temperature dependence in disordered organic semiconductors. Using an activation energy of E_a=0.1 eV TSC curves were generated and fitted to equation (1.1) (S1.1a). This did not lead to a difference between the extracted and input trap energy (difference smaller than 0.02%). Another way to probe the sensitivity of equation (1.1) is to use large variations in mobility (see SI, S1.3 f). By varying the mobility from 10^{-6} cm^{2}V^{-1}/s to 2 cm^2 V^{-1}/s the extracted trap energy only varied from 0.352 to 0.351 eV demonstrating negligibly small dependence on mobility.
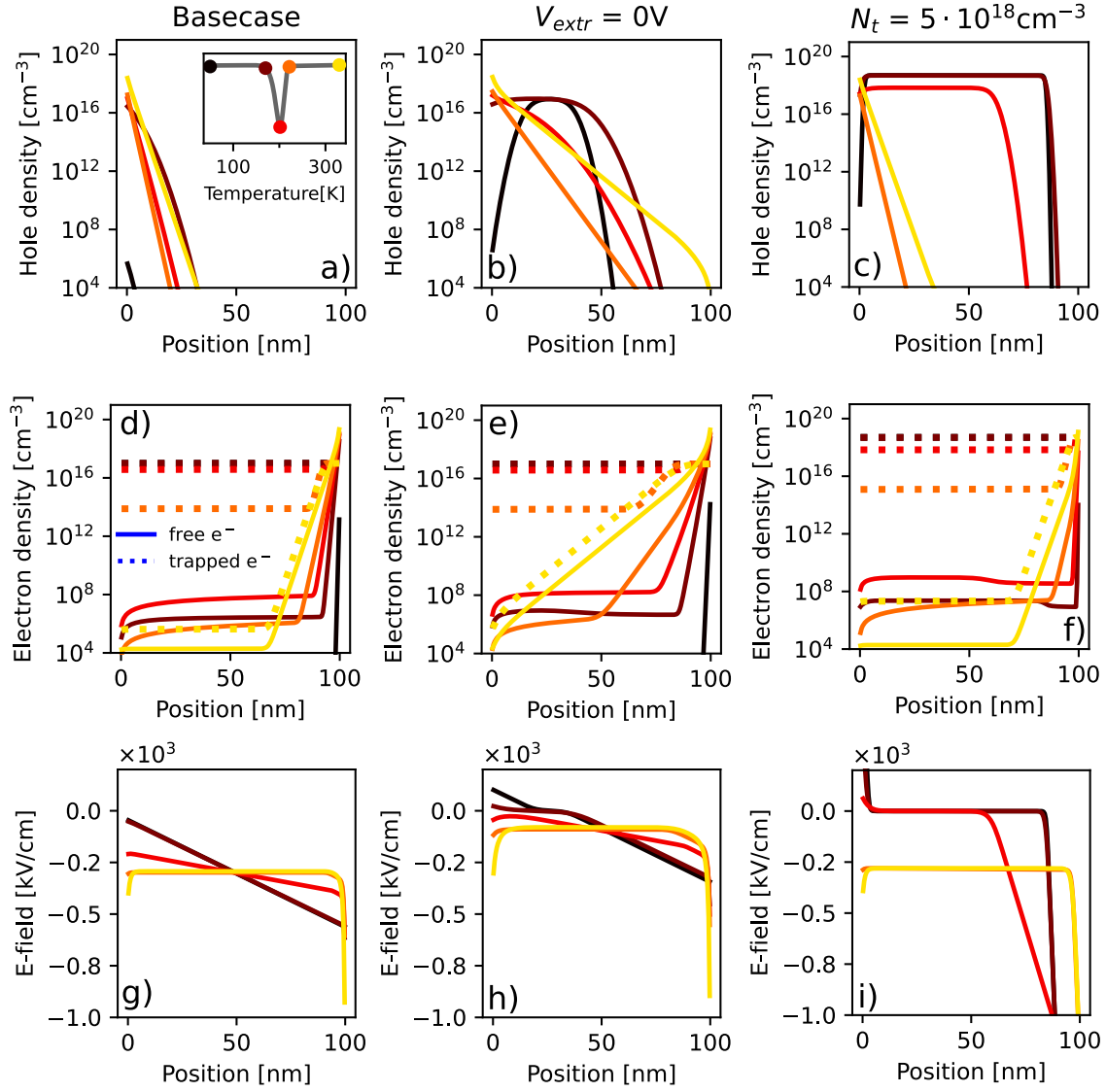
Figure 1.6 hole density (top row), electron density (middle row) and electric field (bottom row) as a function of the position inside the device for three sets of parameters at different temperatures. The anode is positioned at 0 nm, while the cathode is situated at 100 nm. a), d) and g) correspond to the base case while in b), e) and h) the extraction voltage V_{extr} was changed to 0 V with respect to the base case. In c), f) and i) the trap density was increased to 5x10^18 cm^-3. In d), e) and f) the electron densities for free (solid line) and trapped (dotted line) electrons are shown. The different colours from black (50K, start of the TSC experiment) through to yellow (330K, end of TSC experiment) denote the temperatures at which the electron and hole densities were extracted and correspond to the temperatures at which significant changes in the TSC curve take place (inset in a). Note: The peak maximum of the TSC occurs at different temperatures for different sets of parameters.

1.5   Conclusion

This study applies drift-diffusion modelling to generate TSC curves of organic semiconductors incorporating trap distributions with characteristic energy, density and capture rate. The synthetic data revealed valuable to validate trap parameter extraction commonly obtained from analytical equations based on simple physical models. The latter are based on a homogenous distribution of traps, the absence of space charge as well as a constant free carrier lifetime. Such conditions are hardly found in organic semiconductors. Advantageously, drift-diffusion simulation permits to track various local physical quantities during the TSC run. Charge carrier density of electrons and holes, carrier recombination as well as the electric field through the device can be analyzed in

detail for a large variation of parameters. This study reveals that not all underlying hypotheses of the standard physical model are fulfilled, i.e. the absence of space charge and minority carriers or the uniformity of the electrical field throughout the sample. Despite these discrepancies, the physical model based on slow recapture rate provides remarkable parameter extraction when fitted to the synthetic drift-diffusion data. It fails, however, regarding the prediction of the charge density by a factor of two. This electrostatic factor is indeed often neglected in the analysis of TSC curves and can be straightforwardly revealed by the drift-diffusion analysis. Furthermore, the effect of charge carrier diffusion of holes and electrons into the organic semiconductor cannot be neglected. Even at strong extraction fields and high temperatures, an appreciable density of charge carriers remains trapped and cannot be extracted. At low extraction field this effect is even more pronounced and also allows the free charge carriers to diffuse into the device leading to recombination losses. This particular mechanism leading to non-extractable trapped charge carriers has not been discussed or quantified so far.

Regarding the equations derived from the standard model based on slow retrapping, the so-called initial rise method appears to be very robust with respect to parameter variation. It provides accurate predictions for large ranges of trap energies, densities as well as extraction voltage and performs very well also for large sample thicknesses. Similar to the slow-retrapping formula, it fails at high capture rates where the hypothesis of slow recapture rates is clearly violated. Using the simplest formula based on the temperature T_{max} of TSC peak current is generally not successful for predicting the correct trap parameters. It requires the knowledge of other trap parameters, in particular the capture rate, which can be understood by the fact that the T_{max} method does not include trap dynamics.

Thus, drift-diffusion analysis not only allows to understand the electronic processes taking place inside the device during a TSC run, but can also provide useful information to the experimentalist in order to design samples and electrodes for a more accurate trap parameter extraction. The present approach provides a model system that can be developed further to include even more complex features. For example, exciton splitting by an external electric field could also be implemented in the case of organic semiconductors, where recombination first leads to strongly bound electron hole pairs. Above that, drift –diffusion modelling also allows to account for non-homogeneous trap densities, trap densities including electron and hole traps or various trap energy distributions. In standard analytical approaches, such intricated situations cannot be implemented.

1.6   Supporting information

1.6.1   Abbreviations

Table 1.1 Symbols and abbreviations used in drift-diffusion formulas.

Symbols	
J_n	Current density arising from electrons
e	Elementary charge
n	Density of electrons in the LUMO
μ_n	Electron mobility
$\vec{E}$	Electric field
D_n	Diffusion coefficient for electrons
t	Time
$R_{langevin}$	Langevin recombination rate
R_{nt}	Charge trapping and release
g_{opt}	Generation efficiency
G_n	Electron generation rate
ε	Relative permittivity of the medium
ε_0	Permittivity of space
N_D^+	Donor density
n_t	Density of trap sites occupied by electrons
e_n	Emission rate of electrons from traps
c_n	Capture rate of electrons
$N_{0,n}$	Density of states of electrons in LUMO
E_t	Trap energy with respect to closer band edge
N_t	Density of trap states
LUMO	Lowest unoccupied molecular orbital
HOMO	Highest occupied molecular orbital
T	Temperature [K]
k_B	Boltzmann constant
β	Heating rate

1.6.2   Drift-diffusion parameters

The most important parameters used for the simulations are presented in the following tables. For single parameter variations, one parameter at a time was changed systematically. The values used during the variation are specified in the main text. Table 1.2, Table 1.3 and Table 1.4 provide the parameters used for the base case.

Table 1.2 Material parameters. The parameters were chosen from a range of values commonly found for organic materials. They do not correspond to one specific material.

Material / device parameter	
Trap energy [eV]	0.35
Trap density [cm^{-3}]	1x10^{17}
Capture rate coefficient [cm^3/s]	1x10^{-14}
Mobility electron [cm^{2}V^{-1}/s]	2x10^{-4}
Mobility hole [cm^{2}V^{-1}/s]	5x10^{-4}
Langevin recombination coefficient [1]	0.1
Relative permittivity [1]	3.5
HOMO [eV]	5.35
LUMO [eV]	4.1
Anode workfunction [eV]	5.2
Cathode workfunction [eV]	4.15
Available DOS [cm^{-3}]	1x10^{21}
Semiconductor thickness [nm]	100

Table 1.3 Numerical details used for the drift-diffusion simulation

Numerical details	
Discretisation length [nm]	0.497
Timestep dt [s]	0.5

Table 1.4 Experimental parameters used for the TSC method

Experimental simulation parameter	
Heating rate [K/min]	10
Start temperature [K]	50
End temperature [K]	330
Extraction voltage (at anode) [V]	-2
Loading voltage [V]	1.05
Equilibration time (t$_{rest}$)[s]	120
Excitation wavelength [nm]	500

An ohmic injection model with Dirichlet boundary conditions is used. At the electrodes, thermal equilibrium is assumed such that $p_{|anode} = N_{0,p} \exp\left[(\Phi_a - \mathrm{HOMO})/k_B T\right]$ and $n_{|cathode} = N_{0,n}\exp\left[(\mathrm{LUMO} - \Phi_c)/k_B T\right]$, with p, n being the density of holes and electrons at specified location, $N_{0,p}$ $N_{0,n}$ the density of states of the transport levels and Φ_a, Φ_c the workfunction of the anode and cathode, respectively.

Optical parameters are not particularly important for the thermally stimulated current. However, since the device is loaded with charge carriers using light, an absorption profile needs to be defined. For all simulations, absorption data of a 1:1 P3HT:PCBM blend from Monestier et al [97] is used. The wavelength for the illumination is 500 nm. At this wavelength, n_{opt} and k of P3HT:PCBM are 1.87118 and 0.56966, respectively.

In organic semiconductors charge carrier transport is usually described by hopping processes between sites with different energy. Localized electronic states which are energetically distributed within the band gap of the semiconductor can be understood as charge carrier traps and are divided into shallow traps for localized states separated by the thermal energy kT from the respective band edge and deep traps, where the energetic difference from the band gap is several kT[29]. Shallow traps are ubiquitous in organic semiconductors since a major part of shallow traps originate from disorder within the material. Shallow traps therefore have to be considered when using drift-diffusion to simulate organic semiconductors. However, it could be shown that the most prominent effect of shallow traps is the reduction of mobility due to increase in disorder and activation energy[98]. Therefore, we can account for the effect of hopping transport and shallow traps by using a small charge carrier mobility of 2.0×10^{-4} cm^2 V^{-1} s^{-1} for electrons and 4.0×10^{-4} cm^2 V^{-1} s^{-1} for holes. These values are well within the range of mobilities found for different low disorder polymers like P3HT (pristine: 5.7×10^{-5} doped: 1.6×10^{-4} cm^2 V^{-1} s^{-1} measured by EFISGH)[99], BEH-PPV (2.0×10^{-5} cm^2 V^{-1} s^{-1})[100] , PTB7 (1×10^{-3} cm^2 V^{-1} s^{-1} measured by TOF)[101] or polymer blends like PCDTBT:PCBM70. Since hopping transport is strongly dependent on temperature and electric field and the presence of traps change the internal field within the device it is reasonable to assume a field and temperature dependence of the mobility. However, the use of field-temperature and temperature dependent electron mobility (while hole mobility is kept constant) has shown little influence on the TSC peak (S1.1). Therefore, a constant mobility was assumed for this study to improve convergence and to reduce calculation time and the number of parameters.

1.6.3 Temperature dependent Mobility

Temperature dependence is calculated according to [102]

$$\mu = \mu_0 * \exp\left[-\frac{E_a}{kT}\right] \qquad (1.8)$$

where μ_0 is the mobility pre-factor, E_a is the activation energy, k_B is the Boltzmann factor, T is the temperature. For the temperature dependent mobility, we used 0.1 eV as the activation barrier and μ_0 = 4×10^{-2} m^{2}V^{-1}/s
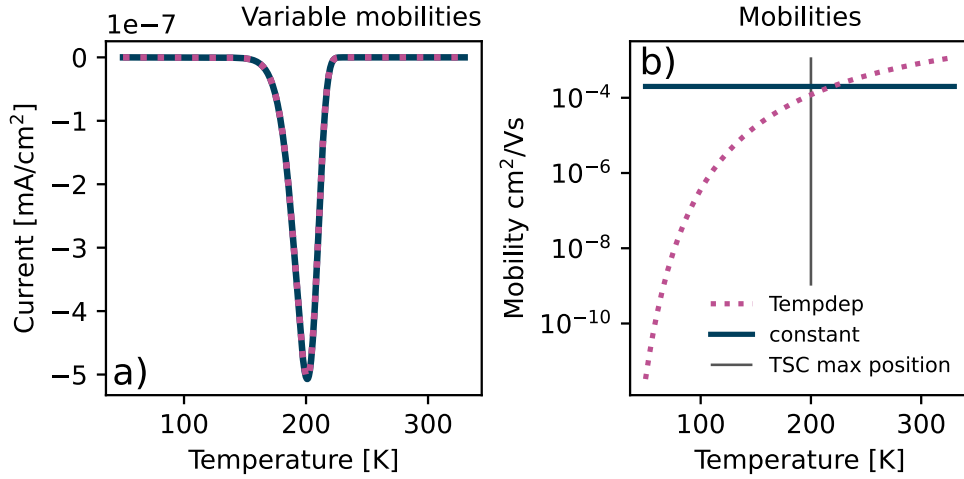
S1.1 Comparison of TSC simulations for constant mobility and temperature dependent mobility of the electrons. For the constant case the electron mobility is $2*10^{-4} cm^2/Vs$. In the temperature dependent case, $E_a = 0.1$ eV and $\mu_0 = 4x10^{-2}$ m²V⁻¹/s. In both cases, the hole mobility is constant with a value of $4*10^{-4}$ cm²/Vs. b) plot of the different mobilities as a function of temperature. the yellow curve is the temperature dependent mobility (no field dependent components) while the blue curve denotes the electron mobility for the constant case. The temperature of the peak maximum is marked by a fine black line.

The TSC peak for constant and temperature dependent electron mobilities are superimposable (S1.1a). The mobilities used for the simulations are displayed as a function of temperature in S1.1b). The temperature where the TSC peak reaches its maximum is marked. Using the full curve fit without taking the temperature dependence of the mobility into consideration, one receives a value of 0.35 eV for the trap energy. The input value of the simulation is 0.35 eV. Although the mobility in the temperature dependent mobility case varies over ten orders of magnitude, it is sufficient to use a constant mobility for the determination of trap state parameters from the analytical TSC. However, it is expected that a low mobility can lead to increased recombination and therefore a lower TSC peak intensity.

1.6.4 T4max derivation

By differentiating the slow formula (1.1) and setting equal to zero one can find following expression.

$$\exp\left(\frac{E_t}{k_B T_{max}}\right) = \frac{N_0 S v k_B T_{max}^2}{\beta E_t} \tag{1.9}$$

where T_{max} is the temperature where the TSC peak reaches maximum intensity. Here, the temperature dependence of density of transporting states N_0, electron mobility μ, thermal velocity v, trap capture cross-section σ and charge carrier lifetime τ is not considered for the differentiation and it is assumed that $E/kT_{max} \gg 1$

This equation can be rearranged to

$$E_t = k_B T_{max}\left[\ln\left(\frac{T_{max}^2}{\beta}\right) + \ln\left(\frac{N_0 v S k_B}{E_t}\right)\right] \tag{1.10}$$

For inorganic materials there exists a temperature dependence of N_0 of $T^{3/2}$ from

$$N_0 = 2\left(\frac{k_B T m^*}{2\pi\hbar^2}\right)^{3/2} \tag{1.11}$$

43

and for ν of $T^{1/2}$ from

$$\nu = \sqrt{\frac{3k_B T}{m^*}} \tag{1.12}$$

where m* is the effective mass of the charge carrier and $\hbar$ is the reduced Planck's constant.

This temperature dependence can be expressed explicitly giving

$$E = k_B T_{max} \left[\ln\left(\frac{T_{max}^4}{\beta}\right) + \ln\left(\frac{CS}{E}\right) \right] \tag{1.13}$$

with C a temperature independent constant between of 1×10^{16} to 6×10^{17}/sK^{-3} depending on the value of the effective electron mass. If the capture cross section S is in the range of 10^{-17} to 10^{-16} cm^2 and Tmax > 100 K, the first term in the formula dominates the second term and the formula therefore can be reduced to the known T4max formula [79]

$$E = k_B T_{max} \ln\left(\frac{T_{max}^4}{\beta}\right) \tag{1.14}$$

In organic materials, it is questionable whether the product of C*S is always close to one. Also, the temperature dependency needs to be examined. Therefore, this formula is not suited for the determination of trap energy in organic semiconductors.

1.6.5 Temperature dependence for the maximum current method
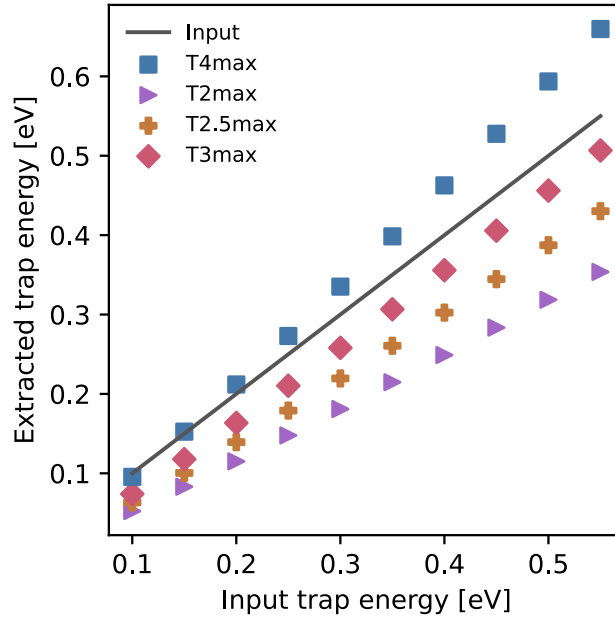
S1.2 T_{max} formulas with different dependences on temperature. T^4_{max} formula has a dependence of T^4, $T^{2.5}_{max}$ has a dependence of $T^{2.5}$ and so on. The trap energy variation has a similar gradient as the prediction of the T^3_{max} formula. It stands to reason that T^3 might be the more realistic temperature dependence for the constraints of our drift-diffusion model and the set of parameters given by the base case

In the drift-diffusion simulation, N_0 is independent of temperature. We therefore expect a different exponent in the T_{max} formula to fit the data better. Indeed, a factor of T^3_{max} reproduces the trend

more accurately (S1.2). However, since the product of C*S is not close to 1, the extracted trap energy values still are off and the formula therefore is not applicable.

1.6.6 Examples of single parameter variation of drift-diffusion data
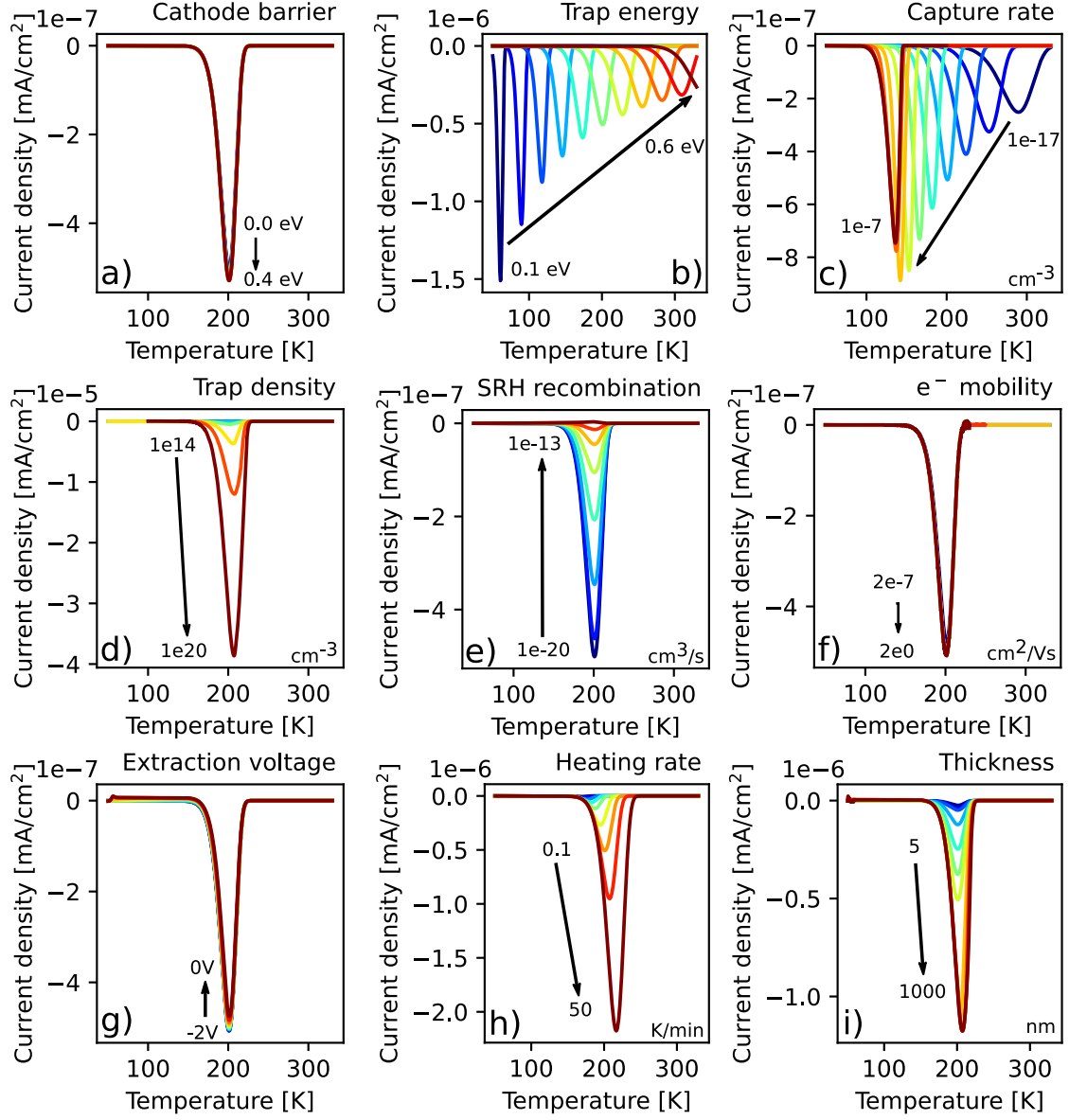
S1.3 Dark current subtracted TSC curves for different single parameter variations. Displayed are a) injection barrier variation of electrons at the cathode, b) variation of trap energy, c) changes in the capture rate, d) trap density variation, e) Shockley-Read-Hall recombination (variation parameter is hole capture rate of the electron traps), f) variation of electron mobility (constant), g) applied extraction voltage variation (+ applied at cathode), h) different heating rates, i) thickness variation of the semiconductor layer. In each subplot, the corresponding parameter is changed from low values (blue, number on blunt end of arrow) to high values (red, number at arrow head). The amount of change in the TSC curve upon parameter change is displayed by the length of the arrow (not to scale), while its direction shows the TSC peak shift in temperature.

1.6.7 Procedure for data extraction using the initial rise method

Often, the fit of the initial rising part of the TSC curve is done in a logarithmic plot where (1.2) can be expressed as $\ln(J_{TSC}) = \frac{-E_t}{1000 * k_B} * \frac{1000}{T} + const$. S1.3 displays the TSC data as the logarithmic plot of the current vs. the inverse of the temperature. For the initial rise fit three different lengths

of data – namely 50, 100 and 200 points - were used at different locations within the range of the initial rising part of the peak marked by the two dashed lines (total of 300 points, see S1.4 a and c). The most accurate trap energy values are received for midpoints at the inflexion point of the rising curve (5.9 [1000/K]) irrespective of the amount of data used for the fit (see S1.4c and d). However, if smaller data intervals are used for the fit, the extracted trap values are closer to the input value of 0.35 eV (black line). Close to the edges of the marked region, the extracted trap energy deviates up to 0.1 eV from the input trap energy (S1.4b). For this reason, a small data interval (50% of the initial rising data points) including the inflexion midpoint as described before is used for the fitting procedure in this work.
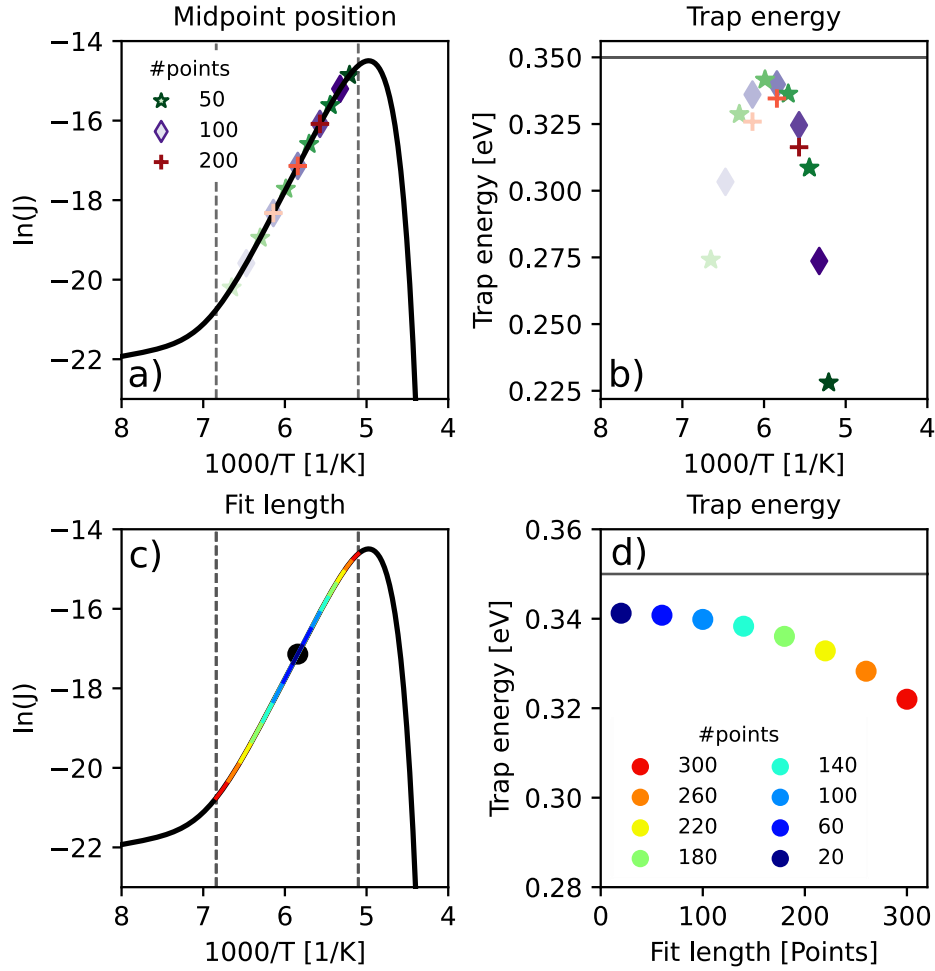
S1.4 Location of data range and fitting interval length dependency of the initial rise fit for the base case. a) logarithmic plot of the TSC peak vs 1000/T using different fitting midpoint positions. The data lengths used are either 50 points (green stars), 100 points (purple diamonds) or 200 (red plus- ses). In b) the extracted trap energy using the different lengths and fitting positions in a) is displayed. c) logarithmic plot of the TSC peak vs 1000/T using the inflection as data fit midpoint with different data intervals marked in color. Blue corresponds to the shortest interval (20 points), while red repre- sents the longest one (300 points). The overall range of the data considered is 300 points and lies between the dotted lines. d) Extracted trap energies for different data intervals used for the fit of c). The colour schematics corresponds to the one used in c).

1.6.8 Detailed contribution of holes, electrons and recombination to the TSC curve

S1.5 TSC simulation broken down into contribution from holes (red) and electrons (sky blue). The recorded current signal is denoted by a black solid line, while the calculated, ideal TSC peak is displayed with a black dotted line. The recombined charge carriers are displayed as a recombination current by a grey line. In a) the base case is displayed. In b), the extraction voltage was changed to 0V, while in c) and d) the trap density was changed to 1x10^{18} and 1x10^{19} cm^{-3}, respectively. In the last row, the current contribution for 250 nm (e) and 500 nm (f) thick active layers are displayed. All parameters which were not specifically mentioned correspond to the parameters used in the base case. To better resolve the overlapping lines in a), the lines denoting the recorded TSC peak (black) and the electron contribution (sky blue) are fattened.

Ideally in TSC measurements, recombination inside a device is prevented to maximize the number of extracted charge carriers. However, our studies show that this prerequisite is also necessary to correctly determine trap energy and capture rate. The reason for this is the peak distortion that arises due to contribution of both holes and electrons to the TSC signal beside recombination loss which shifts the peak to higher temperatures. In S1.5 TSC simulation broken down into contribution from holes (red) and electrons (sky blue). The recorded current signal is denoted by a black solid line, while the calculated, ideal TSC peak is displayed with a black dotted line. The recombined charge carriers are displayed as a recombination current by a grey line. In a) the base case is displayed. In b), the extraction voltage was changed to 0V, while in c) and d) the trap density was changed to 1x1018 and 1x1019 cm-3, respectively. In the last row, the current contribution for 250 nm (e) and 500 nm (f) thick active layers are displayed. All parameters which were not specifically mentioned correspond to the parameters used in the base case. To better resolve the overlapping lines in a), the lines denoting the recorded TSC peak (black) and the electron contribution (sky blue) are fattened. the peak distortion leads to an extracted trap energy value of 0.42 eV and 0.38 eV for trap densities of $1x10^{18}$ cm^{-3} (c) and $1x10^{19}$ cm^{-3} (d), respectively, using equation (1.1) for an input value of 0.35 eV. Also, for the case of no applied external field (b), the peak distortion and the decrease in peak intensity is already noticeable (0.38 eV, $4x10^{16}$ cm^{-3} vs input of 0.35eV and maximum measurable trap density of $4.5x10^{16}$ cm^{-3}). In the base case (a), the concentration of free holes is not significant. The TSC peak therefore only reflects the contribution from de-trapped electrons and the application of formula (1.1) yields accurate values.

This analysis can also be applied to the bimolecular recombination equation (1.4). In case of bimolecular recombination, it is assumed that one prominent effect in the device is the retrapping of charge carriers. However, this effect is only considered at the decreasing part of the TSC curve. In simulation series with high capture rates and extraction voltages of -2V, the field in the device is sufficiently high to extract the electrons at the electrodes before significant retrapping can occur. Therefore retrapping at this position is usually not observed. (exceptions are for example thick devices without applied extraction field). At the increasing part of the TSC peak though retrapping occurs due to the shielding of the extraction field originating from the space charges of the trapped electrons. The fit of bimolecular recombination to the simulated data performs badly at the rising and falling part of the TSC curve. This may explain the failure to extract accurate trap parameters when fitting simulated data with equation (1.4).

Eventually we note that extraction voltage, trap density or film thickness are not the only parameters affecting peak shape. Electron capture rate can have a strong effect on peak shape, as illustrated by the TSC signals for both fast (S1.6 a) and slow (S1.6 b) capture rate, respectively. The simulation reveals factors that prevent retrapping or mask the latter effect. First, capture rate and emission rate are coupled leading to high emission rates for high capture rates. Under these conditions, emission is nearly instantaneous after trap activation and the TSC curve therefore decreases steeply (S1.6 a). Retrapping cannot be observed, since the trap at that time is already in equilibrium (equal capture and emission rates). On the other hand, an extraction voltage is applied which increases extraction. Retrapping and extraction are competing processes. Increasing the latter will therefore lead to reduced retrapping. Effects from retrapping therefore are hard to see.
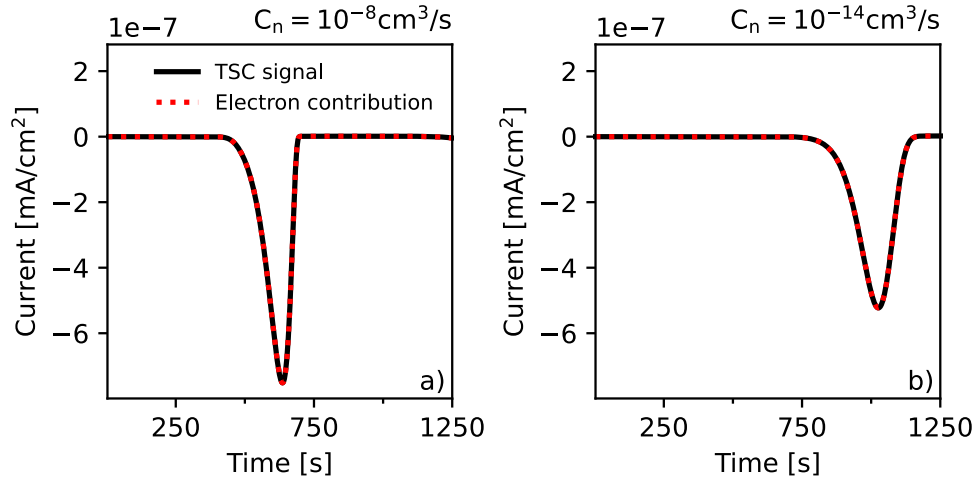
S1.6 The TSC signal (black) and the contribution from electrons towards the TSC signal (red dotted) for a) a fast electron capture rate c_n of 10^{-8} cm³/s and b) a slow electron capture rate of 10^{-14} cm³/s. The latter capture rate is the same as used in the base case (applied voltage of -2V)

1.6.9 Equilibrium concentration of trapped and free charges

The rate of change of the density of occupied traps is given by:

$$\frac{dn_t}{dt} = nc_n(N_t - n_t) - N_{0,n}e_n n_t$$

The emission rate of the charge carriers is defined in the drift-diffusion model as $e_n = c_n exp\left(-\frac{E_t}{k_B T}\right)$

In equilibrium, trap occupation does not change, thus

$$nc_n(N_t - n_t) = N_{0,n}c_n \exp\left(-\frac{E_t}{k_B T}\right)n_t$$

The capture rate falls out of the equation. By dividing the expression by n_t one obtains:

$$n\frac{N_t}{n_t} - n = N_{0,n}\exp\left(-\frac{E_t}{k_B T}\right)$$

Which leads to the trap occupation ratio in equilibrium:

$$\frac{n_t}{N_t} = \frac{n}{n + N_{0,n}\exp\left(-\frac{E_t}{k_B T}\right)}$$

1.6.10 Analysis

For parameter variation, we wrote a python script which

- changed a specific parameter within a defined range
- created an input file for the simulation tool
- uploaded all input files onto a remote Linux simulation system
- start a maximum of 6 simulations simultaneously to stay within allocated CPU capacity
- download finished simulations
- clean up and close connection to remote system

We also used Python for data extraction, fitting and plotting.

Chapter 2: Electron trap evolution in Super Yellow polymer light-emitting diodes

2.1 Introduction

The first polymer light-emitting diode (PLED) was reported in 1990 by Friend et al. [46]. It was based on poly(p-phenylene vinylene) (PPV) emitting green-yellow light with an external quantum efficiency (EQE) of 0.05%. Since then, much effort has been put into understanding the underlying physics and improving device performance leading to an EQE of around 4% for single-layer devices based on superyellow-PPV – the best-performing PPV derivative. For more complex devices, performance records of up to 23.5% were achieved[4].

PLEDs have many advantages over conventional inorganic light-emitting diodes. For example, PLEDs can be fabricated with low-cost all-solution processes[103], inkjet printing[104] and even large-scale fabrication methods like roll-to-roll techniques[105]. In addition, PLEDs are mechanically flexible[106][107], and their emission spectrum is highly tuneable by varying building blocks or adding dopants, making it possible to fabricate devices emitting within a spectrum ranging from deep blue (415nm)[108] to near-infrared light (696nm)[109]. Also, PLEDs have a fast response time (< 10 μs)[110], exhibit a high brightness (142'000 cd/m^2) [111] and require low driving voltage (<10 V)[112].

However, there remain some challenges to be addressed. For example, PLEDs have a short lifetime and low efficiency[113]. The latter can largely be attributed to the low and unequal mobility of charge carriers, while the former often is an effect of degradation due to the low stability of constituting layers – especially the cathode, formation of pin-holes[114] or build-up of trap states[115][116]. Furthermore, the fabrication of multi-layered devices presents another difficulty. For each layer, solvents that do not redissolve the underlying layer must be found.

Trap states can severely limit the efficiency of a PLED. There inherently are shallow trap states in PLEDs originating from the random ordering of the polymer chains, leading to an uneven spatial distribution of accessible transport states with variable hopping lengths in-between. Consequently, also a distribution of energies is associated with the transport states. Some transport states energetically extend into the band gap, still participating in but hindering charge carrier transport leading to a decreased charge carrier mobility.

In addition to shallow trap sites that decrease charge carrier transport, deep trap sites can also exist. Most commonly, deep trap sites originate from dopants, chemical impurities, and chemical reactions like oxidations and reductions impurities, which locally change the energy landscape so drastically that states generated by those impurities are energetically isolated and lie deep within the bandgap of the semiconductor. Charges captured in these states can hardly escape thermally and either are trapped permanently or recombine with a charge carrier with the opposite sign. Deep trap states thus mainly reduce the number of free charge carriers, which is especially notable when only a few free charge carriers are available (i.e. driving at low voltage). It is commonly assumed that trap sites will persist once they are formed.

Trap states and their effect on a device can be mitigated in several ways. One approach is introducing heavy doping into the device to fill the trap states and achieve quasi-trap-free charge transport[39]. Another possibility is to dilute trap states by introducing a large bandgap semiconductor[117]. Furthermore, trap states of a specific energy with respect to the vacuum level can be avoided by choosing a semiconductor material where the present impurities do not lead to

isolated states within the bandgap but to states within the HOMO or LUMO[37]. Also, purification of the polymer used in the device can minimize disorder and thus reduce the level of trap sites[118].

Water and oxygen are prominent sources of impurities forming trap states within many organic semiconductors, which lead to the universal formation of trap states at 3.6 eV with respect to the vacuum[37].

In our work, we investigate the temperature-dependent kinetics of such deep trap sites in a model PLED based on superyellow (SY), a yellow-emitting poly(1,4-phenylene-vinylene) (PPV) derivative. The trap sites originating from oxygen and water are expected to be found in SY at 0.7 eV below the LUMO, corresponding to a deep trap with an affinity for electrons. We found such trap sites and observed that the changes in the device associated with the deep trap sites take place on a much slower time scale than would be expected from mere filling and emptying of deep trap sites that are permanently present. Also, a recovery of the devices is recorded, indicating a more dynamic behaviour of deep electron trap states[119]. We now investigate the temperature-dependent behaviour of those trap states within a framework of a potential mechanism for trap generation and deactivation governed by the diffusion of water and oxygen.

2.2   Methods and materials

2.3   Methods
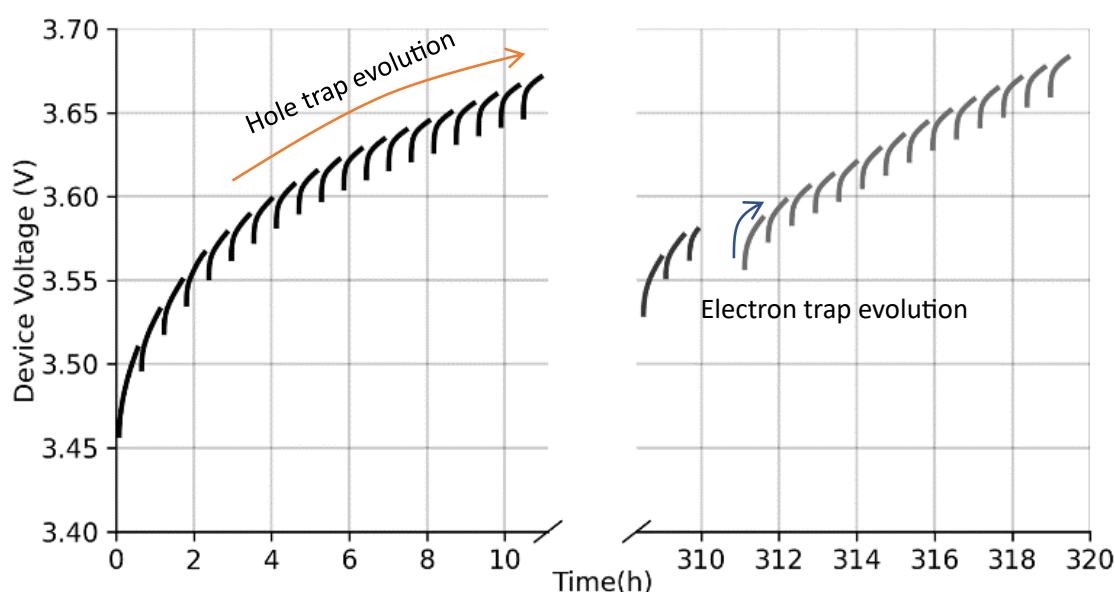
Figure 2.1 Example for the stressing experiment. Stressing was performed at 10 mA/cm² for 30 min with breaks of 5 min at 0 V in between for several stressing cycles. Two longer breaks were applied: 280 h and 90 min. The decrease in voltage between each cycle is attributed to the deactivation of electron trap states. Even for long break times, the voltage does not recover to the initial voltage value. This irreversible voltage increase is due to the development of hole trap states.

The primary measurement technique used in this work is the stressing of a device by application of a constant current (10 mA/cm² if not stated otherwise). It was shown that the change observed in the voltage of the SY device could be attributed to the development of hole trap states[120]. We adapted the method by introducing a series of breaks during stressing, during which the device is kept at short circuit conditions for 300 seconds. We could show that the observed change on a short time scale of minutes is due to the development of deep electron trap sites[121]. An example

of this measurement is presented in Figure 2.1. The time scale for generating hole and electron trap sites is marked.

The method was adapted in several fashions to investigate further the generation of deep electron trap sites. The stress time between breaks was set to 5 minutes to minimise the influence of hole trap generation. The break time was varied between 3 to 900 seconds to study the trap sites' dynamics. Changes in the generation rates were investigated by changing the stressing current density to 5 or 20 mA/cm^2 or changing the temperature within a range of 230 K to 330 K.

Filling pre-existing trap sites in the device takes 80-200 µs in each stressing cycle[121] (see SI). However, the averaging time per measurement point is around 300 ms. Therefore, all existing trap sites are filled immediately at the beginning of the experiment and thus are not the cause for the voltage increase observed.

The influence of Joule heating, the migration of ionic impurities or the reorientation of internal dipoles was excluded as a cause for the voltage increase during stressing[23].

To extract the number of trap sites generated during the experiment, the device is modelled in a 1D drift-diffusion setting.

2.3.1 Materials
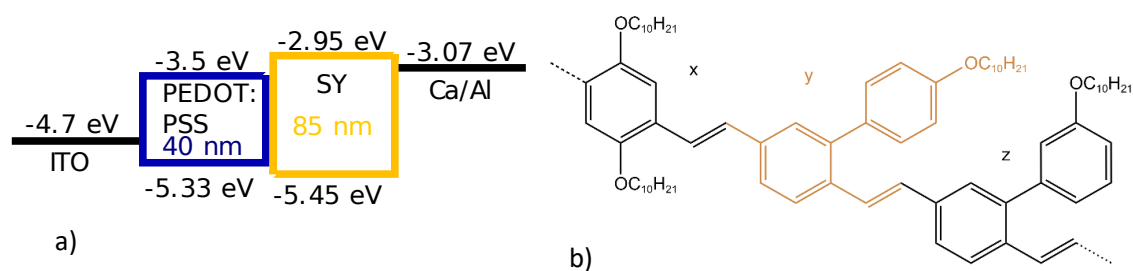
Figure 2.2 a) Structure and corresponding energies of electrode work functions and HOMO/LUMO of the PLED device used for the measurement. b) Structure of the superyellow (SY) polymer used as emitter in the PLED. The middle building block is marked in brown to help differentiate between the building blocks.

PLEDs with the structure of glass/ITO 135nm/PEDOT:PSS 40nm/active layer 85nm/Ca 10 nm/Al 70nm were fabricated by members (Tao Zhang, Wei-Hsu Hu) of the Laboratory for Functional Polymers at Empa Figure 2.2(a). The active layer used is SY, a commercially available PPV-derived copolymer bought from Merck with a composition as displayed in Figure 2.2b. Devices were sealed with a sealing glass and encapsulation epoxy (Ossila, cured for 5 min. with a Hg lamp, 100 W (UVA cube 100 Hönle)) to prevent ingress of water and oxygen which both would lead to a fast degradation via formation of dark spots. The device fabrication steps were reported elsewhere[121]. For the structure of PEDOT:PSS, refer to S2.1.

2.3.2 Measurement

The measurements were performed with the Paios measurement system from Fluxim AG. For temperature-dependent measurements, the devices were placed on a Paios Peltier cryostat outside the glove box. To prevent the build-up of condensate and ice during cooling, the cryostat chamber was flooded with dry nitrogen. The pristine devices were preconditioned at 20 mA/cm^2 for 5 minutes or 10 mA/cm^2 for 10 minutes to reach a state where the device's performance was stable over the following measurements. To minimize the influence of hole trap development, devices were run 5 minutes at a time before a resting period.

Temperature-dependent measurements were performed on the same pixel according to a temperature cycle depicted in S2.2. In addition, intermediate measurements at 300 K were performed regularly to see whether the device performance deteriorated over time; no deterioration besides the generation of deep trap sites was found over the course of the experiment.

In a second set of experiments, a new pixel was used for each temperature to prevent the device's ageing. The trends seen in both experiments were the same.

2.3.3   Simulation

It is not possible to directly simulate a constant current experiment using drift-diffusion. In drift-diffusion simulation, the influence of the charge carriers present in the device, the electric field originating from the voltage difference applied, the concentration gradient of charge carriers etc., are used as input parameters to calculate the current that flows through the device as an output parameter. However, the design of our experiment would require using the current as an input parameter. Since this is not yet possible in the software Setfos 5.2 (Fluxim AG) used for the simulation, we circumvented this issue by emulating a constant voltage experiment with the following procedure:

For a given voltage extracted from the experiment at time t=0, the most relevant parameters, such as injection barrier, relative permittivity, (constant) charge carrier mobility and electron capture rate, were adjusted until the simulation yielded 10 mA/cm^2. This adjustment approach in the simulation requires the simultaneous change of at least two parameters at once. Otherwise, it is not possible to achieve a constant current of 10 mA/cm^2 since the change of only one parameter will either increase or decrease the resulting current density.

In a second step, the voltage used in the simulation was adjusted to the voltage measured at 50 s, 100 s, 200 s and 300 s in the experiment. Concurrently, the trap site density was increased to keep the current density at 10 mA/cm^2. The trap site density is the parameter we want to extract from the simulation. All other parameters were fixed at the values determined at t=0.

2.3.4   Simulation parameters

The relative permittivity was extracted from the high-frequency part of an impedance measurement according to $\varepsilon_r = \frac{C_{geom}*d}{A*\varepsilon_0}$ with C_{geom} the geometric capacitance measured in the experiment, d the thickness of the active layer, A the area of the device and ε_0 the relative permittivity of space. The thickness of the active layer was measured at 6 different locations using a profilometer and amounted to 84 ± 1 nm. The area of the top-electrode mask used to fabricate the device was 0.0314 cm^2 for small pixels and 0.0707 cm^2 for large pixels.

For the presented simulations, a symmetric barrier height of 0.12 V was assumed for the injection of holes and electrons. The stack for the electrical simulation consisted of three layers, namely PEDOT:PSS as an anode, SY as the active layer and calcium as the cathode.

For the simulation, the device was assumed to be trap free initially. It was shown that the intrinsic trap-free mobility of holes and electrons in PPV derivatives is the same[39]. Therefore, one set of mobilities (mobility for holes and mobility of electrons) was chosen to be equal. In an actual device, however, shallow electron trap sites are present. It is known that the presence of shallow electron traps reduces the apparent mobility of electrons. Also, from the simulation side, shallow trap sites mainly decrease mobility without significantly influencing the free charge carrier density[98] (see S2.3). It is therefore argued that shallow trap sites can be emulated by assuming lower mobility.

To account for shallow electron traps in an actual device (density$\approx 10^{17}$ cm^{-3}[121]), the mobility of the electrons in the simulation was chosen to be one order of magnitude smaller than the hole mobility in a further simulation series.

The capture rate of the electron trap for electrons as well as holes (SRH recombination) was coupled to the mobility according to $C_{n,p} = \left(\frac{q}{\varepsilon_0 \varepsilon_r}\right) \mu_{n,p}$ [122] with $C_{n,p}$ the capture rate of electrons or holes, respectively, q the elementary charge, and $\mu_{n,p}$ the mobility of electrons or holes, respectively. We also investigated cases where the capture rate was decoupled from the mobility and fixed $C_{n,p}$ to 5x10^{-13} cm^3/s.

For the additional mobility simulations, we used hole mobility values extracted from the space charge limited region from a JV measurement as input and calculated the required electron mobility to satisfy the 10 mA/cm^2 condition. The SCLC data were extracted from pristine bipolar devices assuming no significant shallow trap sites were present. The extracted mobility, therefore, is different than expected from a monopolar device under the assumption of trap states and consists of a contribution from hole and electron mobility. However, it is assumed that the electron mobility is smaller than the hole mobility by at least one order of magnitude, and thus the extracted mobility is mainly comprised of the contribution from the hole mobility.

The most crucial parameters for the simulation are presented in the following table.

2.3.5   Parameters

Table 2.1 Parameters used in the simulation.

Electrodes			Electron capture rate [cm^3/s]	$C_{n,p} = \left(\frac{q}{\varepsilon_0 \varepsilon_r}\right) \mu_{n,p}$
Workfunction PEDOT:PSS [eV]	5.33		Electron capture rate fixed [cm^3/s]	5x10^{-13}
Workfunction Ca [eV]	3.07		Electron trap energy [eV]	0.7
Injection barrier anode [eV]	0.12		Impurities	
Injection barrier cathode [eV]	0.12		Water diffusion (298K) [cm^2/s]	3x10^{-9} - 3x10^{-8}
SY			Oxygen diffusion (298K) [cm^2/s]	1.2x10^{-8}[123]
Rel permittivity [1]	4.5		Water diffusion (230K) [cm^2/s]	4x10^{-12}
Hole mobility [cm^2/Vs]	3x10^{-6}		Oxygen diffusion (230K) [cm^2/s]	3x10^{-10}
Electron mobility [cm^2/Vs]	6x10^{-7}		E$_{activation}$ water diffusion [kJ/mol]	40-64
HOMO [eV]	5.45		E$_{activation}$ oxygen diffusion [kJ/mol]	35-40
LUMO [eV]	2.95		Number of water molecules [1/cm^3]	10^{17}
Electron trap density [cm^{-3}]	0-5x10^{17}		Number of oxygen molecules [1/cm^3]	10^{17}

2.4   Results/Observations

The driving voltage required to drive a device at a constant current density increases over time. We further refer to this as voltage increase. It is an expression of the decreasing performance of the device. However, if the device is left to rest at short-circuit conditions for a certain time after being driven – the rest time - the driving voltage required to achieve the same constant current density is lower than the driving voltage required just before the break. We refer to this decrease in driving voltage during a break as voltage drop or recovery. A graphical representation of our definitions is presented in S2.4.
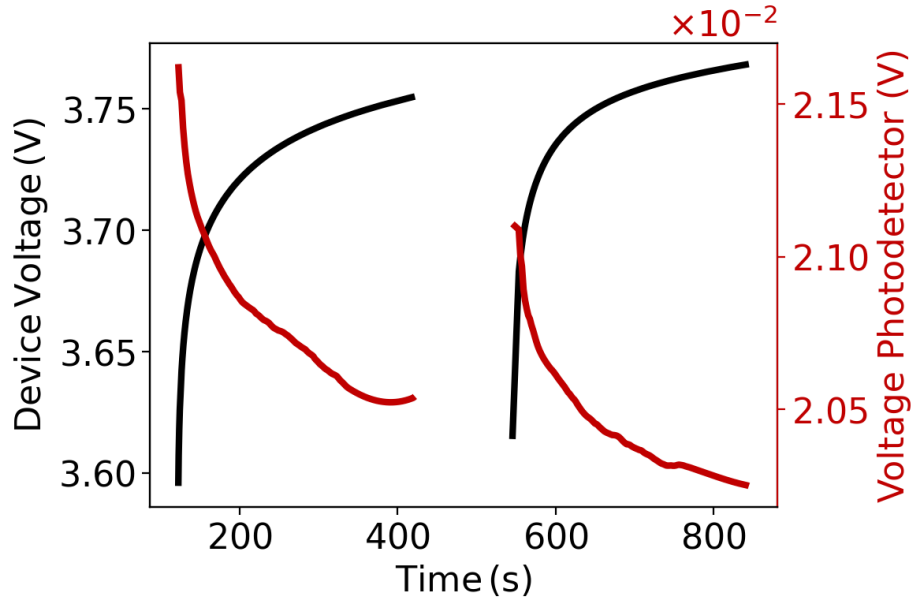
Figure 2.3 Voltage (black) and voltage of the photodetector (red) development for a device at 300 K stressed for 2x5 minutes at a constant current density of 10 mA/cm² with a break of 2 minutes in between. The measured voltage across the photodetector is a means to express the luminance of the device.

Displayed in Figure 2.3 is the behaviour of an SY-PLED under constant current stressing at 10 mA/cm² and a temperature of 300 K. First, the device was run for 5 minutes, followed by a break of 2 minutes at short circuit conditions. Subsequently, the device was rerun for 5 minutes. While running, the voltage needed to maintain the constant current of 10 mA/cm² increased from 3.59 V to 3.76 V (first cycle, 4.7% increase) and from 3.61 V to 3.77 V (second cycle, 4.4% increase). Concurrently, the voltage across the photodetector caused by light emitted from the PLED decreased from 21.6 mV to 20.5 mV (first cycle, 5% decrease) and from 21.1 mV to 20.2 mV (second cycle, 4% decrease). The voltage across the photodetector was used to express the luminance of the device. During the break, a partial recovery of the performance took place. This was visible as an increased luminance and a decreased voltage of the device at the start of the second stress cycle compared to the luminance and voltage at the end of the first stress cycle. During the second stressing cycle, the performance of the device worsened again, reaching higher voltages and lower luminance at the end of the second cycle compared to the first cycle. However, although the voltage in the second cycle started and ended at a higher value than in the first cycle, the overall increase in voltage during the second cycle was smaller (0.16 V vs 0.17 V). Likewise, the luminance started and ended at lower values during the second cycle than the first, but the overall decrease in luminance was smaller (0.9 mV vs 1.1 mV).

Several possible processes could explain a short-term recovery in device performance.

From our experiments, we suspect the generation of reversible deep trap sites for electrons based on complexes formed by water and oxygen to be responsible for the observed decrease and recovery of the performance. However, since it is impossible to prove the presence of oxygen-water complexes by electrical measurements alone, we show in the following sections experiments which led us to dismiss other explanations for the observed device behaviour.

Most of the processes leading to a decrease and recovery of performance, like the filling of existing trap sites (microseconds, see calculation in SI), the generation of permanent trap sites via oxidation (hours)[114] or the degeneration of contacts (days)[124] have a different time scale than observed in the experiment and thus are not considered.

Other processes leading to performance changes with the appropriate time scale are Joule heating or the movement of ionic impurities which accumulate at the electrodes. While the device is operated, the temperature of the device might increase, although the sample was temperature controlled on a Peltier element. This temperature increase is possible since the sample substrate–the part in contact with the Peltier element - does not efficiently conduct heat, and a local heating up of the sample still could be possible. A temperature change can change the mobility within the device and thus influence its performance. The recovery of the device's performance could then be explained by the cooling down of the device during the break.

2.4.1   Effects of heating and cooling on the voltage response of the device
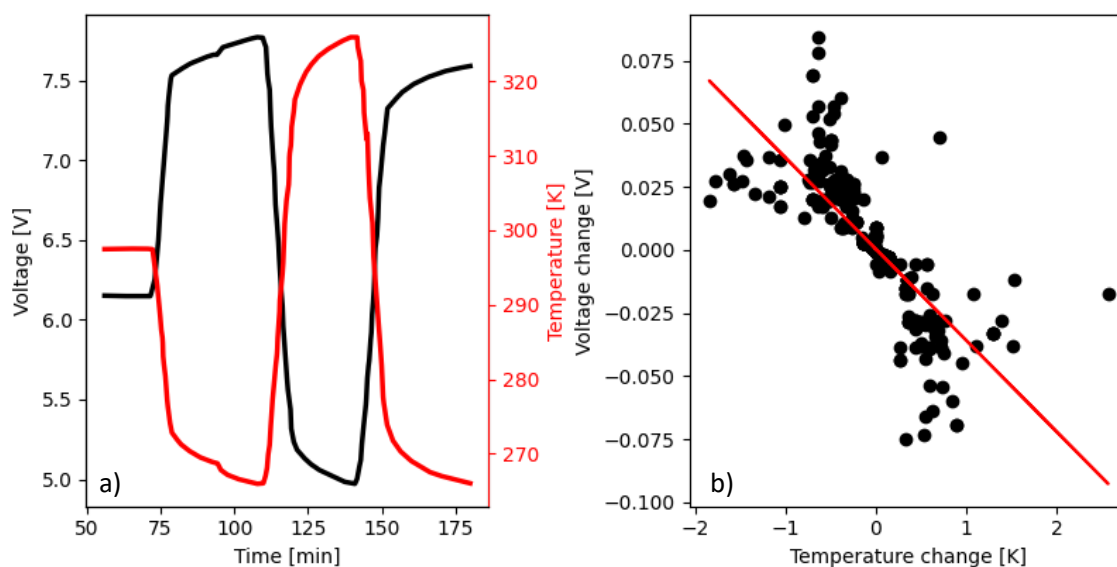
Figure 2.4 a) Applied temperature profile and corresponding voltage response of a SY device. Increase in temperature leads to a decrease in voltage and vice versa. b) Change in voltage as a function of change in temperature. The change in voltage has the same order of magnitude as the voltage change observed in the experiment – but with reversed sign.

a) is adapted from Diethelm, M., Bauer, M., Hu, W.-H., Vael, C., Jenatsch, S., Blom, P. W. M., Nüesch, F., Hany, R., Electron Trap Dynamics in Polymer Light-Emitting Diodes. Adv. Funct. Mater. 2022, 32, 2106185.
https://doi.org/10.1002/adfm.202106185 with permission from copyright holder © 2019 WILEY-VCH Verlag GmbH & Co. KGaA

We investigated the effect of temperature on the measured voltage to see whether the observed features during stressing can be attributed to the heating of the device. For the experiment, a constant current of 10 mA/cm² was applied, and the voltage was measured. During the measurement, the temperature was changed, and its value was recorded as a function of time. The results

are presented in Figure 2.4a. A decrease in temperature led to an increase in voltage and vice versa. Although the voltage change per 1 °C change in temperature has with 25 mV a comparable order of magnitude (Figure 2.4b) as the voltage increase observed during stressing (20-150 mV), the sign of the change is opposite. This means we would expect to see a decrease in voltage while driving the device and heating it, but not an increase in voltage as observed. Therefore, we exclude the device's heating as the origin of the observed voltage increase.

2.4.2   Device recovery under illumination
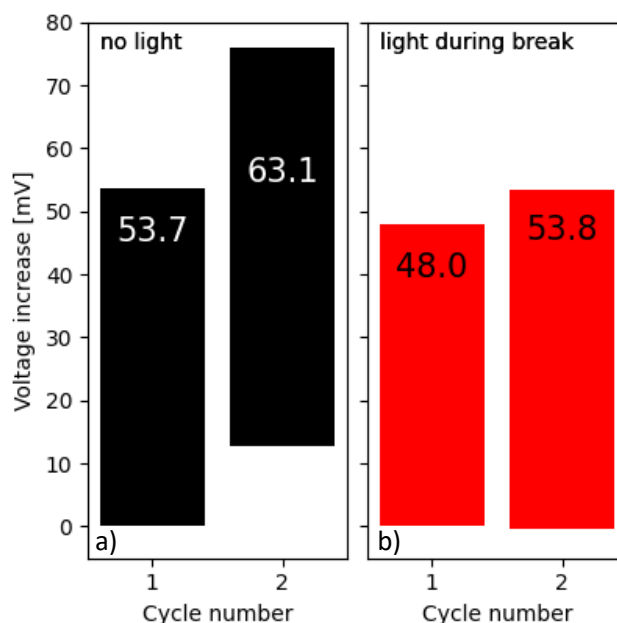
Figure 2.5 Increase in voltage for a device at 230 K during two cycles of stressing at 10 mA/cm^2 for 5 minutes and a break at short circuit conditions for 158 seconds. In a) the device was kept in the dark during the break time. In b), the device was illuminated with light at 830 nm wavelength during the break time.

During the manufacturing process, residual ions from ionic impurities in the polymer solution or the solvent or dissolved ions from the partial dissolution of ITO[125][126] could enter the device's active area. If present, mobile ions will react to an applied external field by drifting towards the electrodes. To which electrode the drift happens depends on the ionic charge and the bias of the field. Under forward bias, cations will drift towards the cathode (calcium), and anions will drift towards the anode (ITO). For a prolonged runtime of the device, mobile ions will accumulate close to the electrodes, changing the internal field and thus the injection and distribution of free charge carriers and, ultimately, the performance of the device. Upon a runtime break, the ions are expected to diffuse back to an equilibrium distribution. We expect that the diffusion of ions is not influenced by the presence or absence of light illuminating the sample. In addition, the diffusion coefficient of mobile ions is strongly dependent on temperature. Reducing the temperature would, therefore, significantly reduce the diffusion coefficient and thus greatly increase the recovery time of the device.

We therefore carried out device performance recovery experiments at 230 K in the presence of an external LED light source. The SY device was stressed for 2x5 minutes at 10 mA/cm^2 with a break time of 158 s in-between the stressing cycles. In one set of stressing cycles, the device was rested in the dark at short circuit conditions (Figure 2.5a, black bars). In another set of stressing cycles,

the device was illuminated with light at 830 nm during the break time (Figure 2.5b, red bars). The choice of wavelength had a strong influence on the device response. For a discussion of the wavelength choice, see S2.5.

During the first stressing cycle, the voltage increased by 53.7 mV; during the second, the voltage increase was higher with 63.1 mV. Also, after a break time of 158 s, the initial voltage was 15 mV higher than in the first stressing cycle. Thus, the chosen rest time was insufficient to recover the device entirely. Furthermore, the recovery slowed down compared to the stressing at room temperature (72% recovery at 230 K vs 87.5% recovery at RT, even though the recovery time at 230 K was 32% longer, data not shown). However, the observed increase in recovery time is not significant enough to be explained by a reduced diffusion of mobile ions.

When the device was illuminated with light during the break, the initial voltage of the second stressing cycle was nearly the same as in the first cycle (bottom line of red bars align). Thus, illumination with a light considerably accelerated the recovery of the device. In addition, the voltage increase in the second stressing cycle was higher for both measurement series than in the first. This contrasts with the trend observed at higher temperatures and shorter break times.

Also, experiments with light-emitting electrochemical cells show that the accumulation of ions close to the electrodes tends to decrease injection barriers and thus improve the device's performance[119]. In SY devices, however, we observe a decay in device performance.

Therefore, we exclude that ionic impurities are the reason for the observed device performance trends.

2.4.3   Device performance loss and recovery caused by reversible trap sites

The observed effects in SY-PLEDs are neither caused by an increase in temperature nor the presence of ions. The time scale in the range of minutes is too large to fill existing trap states, which would explain the decrease in the device performance. Further in this work, we explore the possibility of non-static trap sites, which are generated and filled during stressing of the device, but which also decay when the device is rested. There exist universal trap states in SY, which have a trap energy of around 0.7 eV corresponding to the trap depth we measured[121].
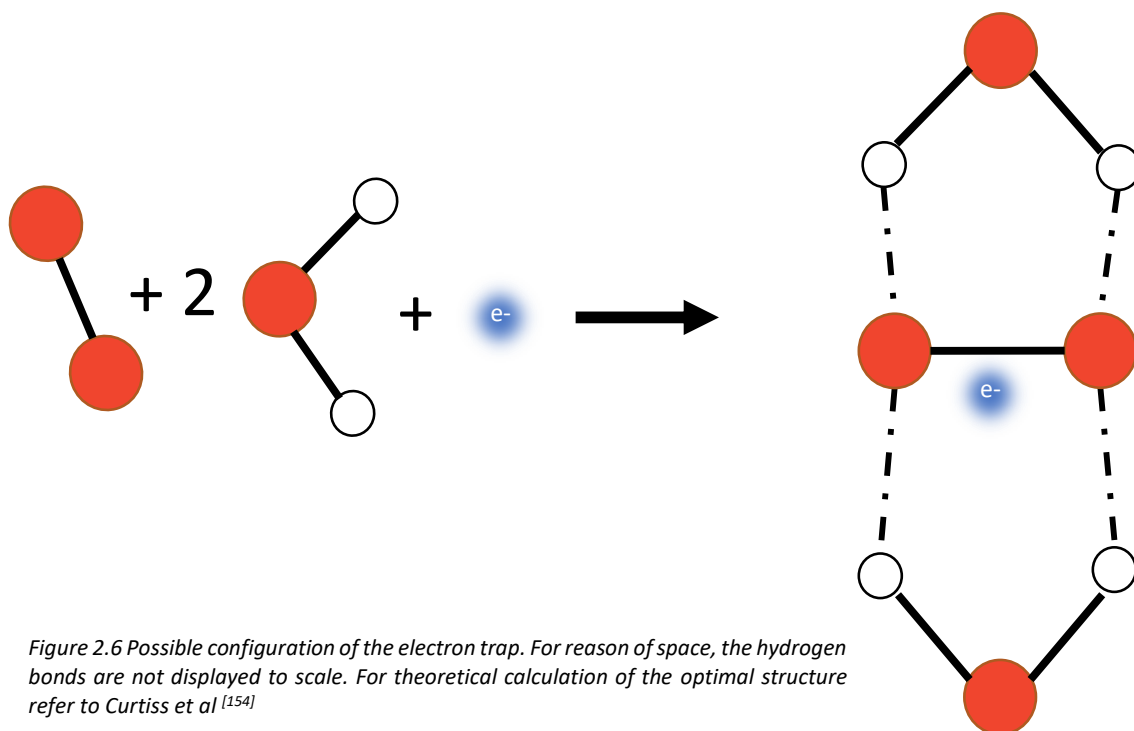
Figure 2.6 Possible configuration of the electron trap. For reason of space, the hydrogen bonds are not displayed to scale. For theoretical calculation of the optimal structure refer to Curtiss et al [154]

A complex of negatively charged oxygen and water molecules was identified as the possible origin of the universal trap states found in numerous semiconducting polymers[37]. The complex can consist of different numbers of water and oxygen molecules[38]. However, the complex leading to deep trap sites in SY is likely composed of one oxygen and two water molecules. A schematic representation of the structure is displayed in Figure 2.6

The binding energy of a neutral $O_2 \cdot H_2O$ complex is between 0.016 eV[127] - 0.02 eV[128], and thus room temperature provides enough thermal energy (approximately 0.025 eV) for the complex to dissociate. The binding energy of the neutral $O_2 \cdot (H_2O)_2$ complex is 0.3 eV without considering zero point energy correction (ZPEC) and 0.18 eV with considering ZPEC[128]. However, it is not known whether such complexes are stabilized or destabilized in superyellow.

The estimated solid-state electron affinity for the $O_2^- H_2O$ complex is at around 3.0 eV, and for $O_2^- \cdot (H_2O)_2$ at around 3.6 eV[38][129]. In SY, the latter amounts to an energy of about 0.7 eV below the lowest unoccupied molecular orbit (LUMO) and therefore qualifies as a filled deep trap. The former qualifies as a shallow trap site and mainly affects charge carrier mobility. A schematic showing the different energy levels is presented in Figure 2.7.

It is important to note that with this hypothesis, only filled deep trap sites exist within the device. Upon de-trapping, the trap site dissociates within minutes. Formation of new deep trap sites requires the concurrent presence of four components (1 O_2, 2 H_2O, 1 electron), considerably increasing formation time.

Vacuum energy 0eV

LUMO SY   2.95 eV

$O_2^-(H_2O)$ 3.0 eV
$O_2^-(H_2O)_2$ 3.6 eV

HOMO SY   5.45 eV
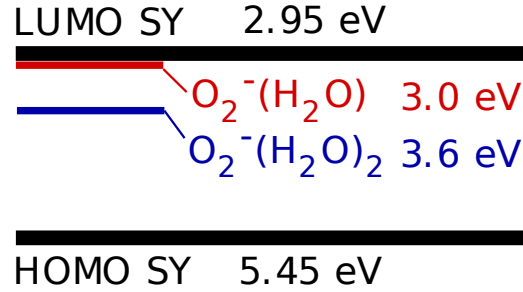
Figure 2.7 Electron affinities of the different water-oxygen complexes with respect to the vacuum level. The LUMO and HOMO of SY is marked in black. The scheme is not to scale.

2.4.4   Mechanism

It is well known from experiments under high vacuum that water cannot be removed from any surface without heating considerably beyond 100 degrees [123]. Removing water from the PE-DOT:PSS layer requires prolonged heating at 130 °C[130]. Since our devices cannot be heated beyond 60°C without introducing significant changes to the structure of SY, it is expected that water molecules are always present in samples, even though they are prepared in a glove box with a dry nitrogen atmosphere. Also, using ITO as the anode can provide a source of oxygen[131]. An estimate of the water content in P3HT amounted to $2 \times 10^{19} cm^{-3}$ at 60% relative humidity [31] and lowers when we try to keep water content in the atmosphere low. The oxygen content was estimated to be around $1.2 \times 10^{18} cm^{-3}$ in P3HT in pure O_2[132]. Note, though, that the water and oxygen content were measured for P3HT and values for SY are not reported. Still, it is reasonable to assume that also oxygen is present in the device.

If no voltage is applied, water and oxygen molecules present in the device can diffuse within the active layer and form neutral complexes upon collisions. Since no free electrons are present under those conditions, the complex is not stabilised by reduction. The complex therefore decays quite fast. A thermodynamic equilibrium between free and complexed water and oxygen molecules exists, favouring free molecules. Free electrons are injected into the device if an external electric field is applied, which can encounter a short-lived complex and stabilise it. A stable, filled deep trap is generated. Those filled trap states can undergo Shockley-Read-Hall (SRH) recombination when the device is under operation and enough free holes are available. In this case, the number of free electrons is high enough to immediately reduce a de-trapped oxygen-water complex again; thus, the number of complexes enters a steady state that is determined by the ratio between free holes and free electrons. When the device is turned off, no further SRH recombination will occur since the number of free holes decreases rapidly.

In addition to SRH, trapped electrons can also de-trap thermally within a time t given by $t = \frac{1}{e_n} = \frac{1}{c_n N_{0,n}} \exp\left(\frac{E_t}{k_B T}\right)$ where e_n is the emission rate, c_n is the capture rate, $N_{0,n}$ is the density of states of the free electrons, E_t is the trap energy with respect to LUMO, k_B is the Boltzmann factor, and T is

the temperature. $N_{0,n}$ is assumed to be 1×10^{-21} cm^{-3}, corresponding to one state per nanometre cube[129].

If the break between two stressing cycles is short, the water and oxygen will still be in close proximity or still bound in a complex, and thus the probability of deep trap site formation is higher than for an equilibrium distribution of water and oxygen.

Deep trap sites can only be generated when there are free electrons present. This is achieved by driving the device at a constant current or voltage. The number of free electrons in the device depends on current density, mobility, and temperature. It will likely be the limiting factor for trap formation since more water and oxygen molecules are present than electrons for a substantial part of the device (S2.6). The distribution of free electrons inside the device will also influence the position of the majority of developing deep trap sites. Since the concentration of free electrons is highest close to the cathode, most trap sites are expected to be close to the cathode.

2.4.5   Trap evolution and decay trends at different current densities
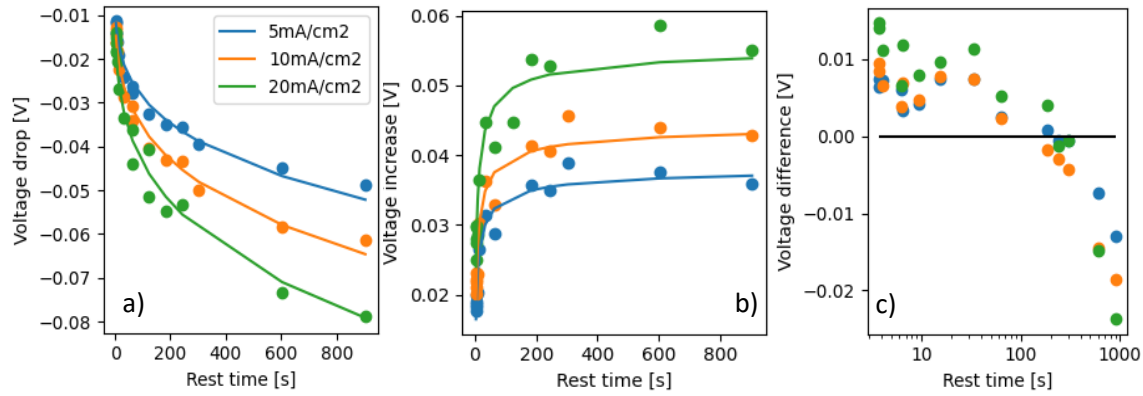
Figure 2.8 Dependence of voltage drop (a) and voltage increase (b) of subsequent stressing cycles on the time in between two stressing cycles (i.e. rest time) and applied current density. The lines in a) correspond to a power law fit with an exponent of 0.27 and in b) the lines correspond to a 3rd order kinetic fit a rate k of 3×10^{-3}. c) Difference between the increase in voltage during the stressing cycle and the voltage drop during the rest time of a previous stressing cycle as a function of rest time. Marked in black is the line where the difference between voltage drop and subsequent voltage increase is zero. Note that the scale for the voltage drop is negative since it denotes the subtraction of the last recorded voltage from the previous stressing cycle (which is higher) from the initial voltage (which is lower) from the following stressing cycle.

To investigate the device behaviour at different current densities, the device was driven at room temperature at a constant current of either 5 mA/cm^2, 10 mA/cm^2 or 20 mA/cm^2 for 16 consecutive stressing cycles with a duration of 5 minutes each. The rest time between the cycles was varied between 3 and 900 seconds. To ensure there is no correlation between the age of the device - i.e. the number of stress cycles – and the rest time, the rest time was chosen according to a specific pattern (see S2.7). Two observations were made from the experiment. First, the longer the break between two stressing cycles, the lower the initial driving voltage for the second stress cycle became. This is displayed as an increased voltage drop for longer rest times in Figure 2.8a. A power law can very well represent the increase in voltage drop with a fractional exponent of 0.27.

Second, the increase of the driving voltage on subsequent stressing cycles also depends on the rest time. Up to a resting time of 300 s, the voltage increase is more pronounced for longer resting times. At rest times longer than 300 s however, the voltage increase in a subsequent stressing cycle levels off and reaches a plateau. The trend of reaching a plateau is independent of the chosen current density and is best described using a third-order kinetic model (Figure 2.8b). Conversely, no plateau is observed for the voltage drop in Figure 2.8a even for long rest times. A reason for

this is the dependency of this experiment on the device history. Further explanations are found in the SI (S2.4).

The second observation was that for increasing current densities, the voltage increase as well as the voltage drop are more pronounced.

It is possible to infer the time needed for the device to fully recover. This is done by comparing the voltage increase with the voltage drop for 14 cycles and extracting the time at which the voltage drop has the same magnitude as the voltage increase (Figure 2.8c black line). We find that a rest time between 184 s for stressing at 5 mA/cm^2 and 244 s for stressing at 10 and 20 mA/cm^2, respectively seconds is sufficient to recover the voltage increase which developed during 5 minutes of stressing. While increasing the current density applied during stressing led to larger observed voltage increases, we also can see a higher voltage drop during the breaks – possibly hinting to a faster recovery rate for devices stressed at higher current densities.

2.4.6 Trap evolution trends at different temperatures
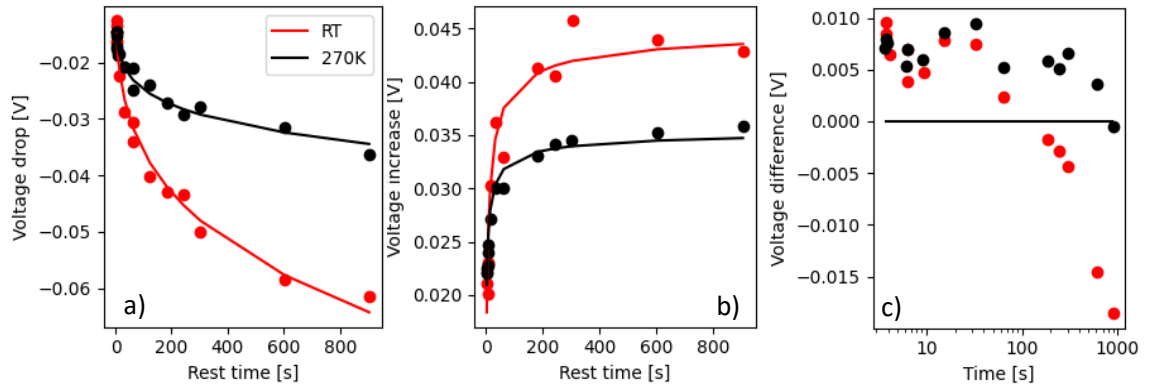
Figure 2.9 a) Voltage drop of a device for different rest times at room temperature (red) and at 270 K (black). The voltage drop follows a power law dependence. b) measured voltage increase as a function of the rest time length. The voltage increase follows a third order kinetics with a fast increase at short rest times and a levelling of at long rest times. The changes in voltage are more pronounced at a higher temperature than at a lower temperature. c) Difference between voltage increase during a cycle and the voltage drop during a break for different break time lengths for fourteen stressing cycles. The black line marks the situation where voltage increase during stressing is equal to the voltage drop in the following break. Values above this line correspond to a situation where the break time is too short to allow the device to fully recover. Values below the line are measured when the break time is long enough for voltage increases built up in previous cycles to recover. This only works if there was an excess built-up of voltage in some previous stressing cycles.

In Figure 2.9 the temperature dependence of the voltage drop a) and voltage increase b) is presented. In this experiment, 16 stressing cycles at a constant current density of 10 mA/cm^2 were applied for a device at room temperature and at 270 K, respectively. As for the current dependent experiment, the rest times were chosen between 3 and 900 seconds. Devices at temperatures lower than 270 K did not fully recover during the rest times applied in the experiment and thus are not displayed here.

The observed voltage drop is lower at lower temperatures than at high temperatures and can be described using a power law with an amplitude of -0.0105 V for room temperature and 270 K. The fractional exponent decreases from 0.27 at room temperature to 0.18 at 270 K.

Similar to the case with different current densities, the voltage increase also levels off for different temperatures and can be described by third order kinetics. However, the time to reach a plateau is greatly increased at low temperatures exceeding 1000 s (Figure 2.9b).

The time for the device to return to initial voltage conditions is strongly dependent on the temperature. In Figure 2.9c displayed is a comparison between voltage increase and voltage drop for 14

stress cycles. We find that at 270 K the device needs close to 900 s to fully recover while at room temperature 244 s are sufficient.

In simulation, power law dependence of the device recovery is observed for Shockley-Read-Hall recombination with free holes diffusing into the device (S2.5).
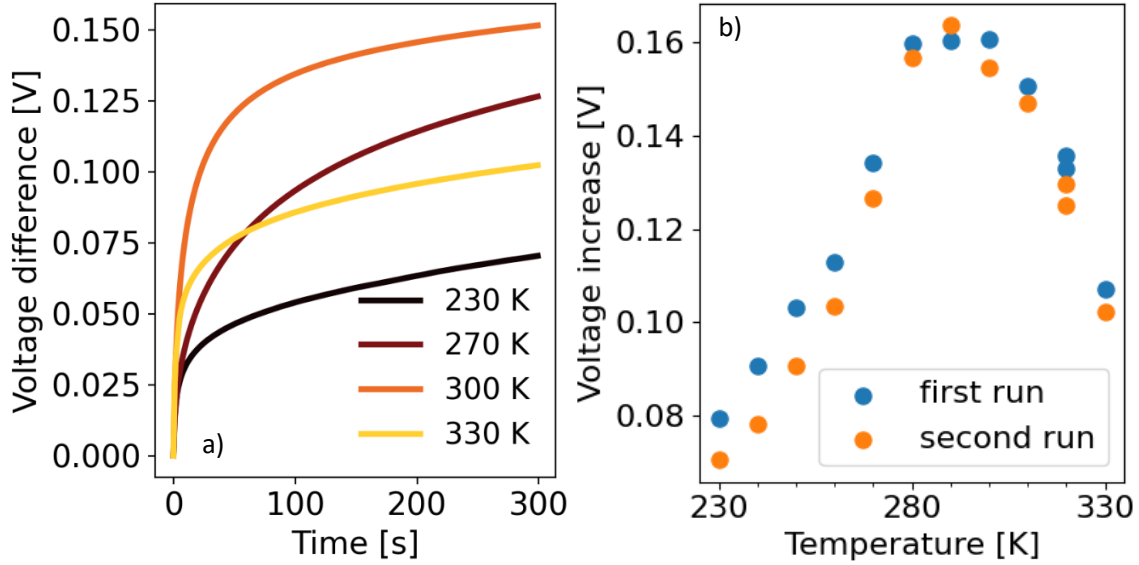
Figure 2.10 a) Measured increase in voltage at different temperatures for a stressing cycle of 5 minutes duration at 10 mA/cm² and a 2-minute break in-between. b) the total voltage increase during two different 5-minutes stressing periods (blue for the first, orange for the second cycle) at different temperatures and 10 mA/cm² current density. Largest increase is observed for a temperature around 290 K.

Displayed in Figure 2.10a is the increase in voltage observed during the second stressing cycle with a duration of 5 minutes at a constant current of 10 mA/cm² for different temperatures. The voltage increase observed after 5 minutes is 0.07 V at 230 K, 0.15 V at 300 K and 0.1 V at 330 K and follows different kinetics (curve shape) depending on the temperature. Further experimenting at different temperatures show that the largest voltage increase occurs around 290 K. Repeating the stressing at the same temperature after a break of two minutes leads to the same voltage increase pattern, but generally with a lower voltage increase (Figure 2.10b). It is notable that after 300 K the voltage increase trend in the device reverts and the voltage increase is less pronounced the higher the temperature gets. However, this change could also be attributed to morphological changes within the devices, as the temperature approaches the glass transition temperature of SY around 80°C[133].

2.5   Discussion

The evolution of trap states is dependent on the rest time between two stressing cycles. The more time there is in between two stressing periods, the more trap states are generated in the subsequent stressing cycle. However, there is a limit at which a further increase in rest time will not lead to a higher number of trap states in the subsequent cycle. At even longer rest times, even a decline in trap site generation can be seen. This can be explained considering two effects. During 5 minutes of stressing, only a limited number of trap sites can form. This limit is governed by the probability that three molecules (2 water, 1 oxygen) collide and form a trap when the complex is reduced by an electron.

The numbers of water and oxygen molecules within a device are assumed to be constant. That means oxygen and water are neither entering nor leaving the device after the fabrication process since the devices are sealed. The number of trap sites which can form during the stressing therefore is limited by the availability of oxygen and water. With increasing number of trap sites already formed, the probability that the remaining water and oxygen molecules collide and form a complex decreases. Consequently, also the trap formation rate upon further stressing decreases, resulting in a lower voltage increase in a subsequent stressing cycle.

The trap states present in the device are generated during stressing, either during one prolonged stressing cycle or many subsequent short stressing cycles where the break time in between was insufficiently long for trap states to decay – leading to a culmination of filled trap states. When no more free water and oxygen molecules are present, no more electron trap sites can be formed. This effect leads to a levelling off of the voltage increase. The drop in voltage increase observed at very long rest times can be explained by the decay mechanism of the trap sites.

When a trap decays, the water-oxygen complex decomposes. But the water and oxygen molecule stay in close vicinity from each other for some time until they diffused sufficiently far away. If current is applied to the device while the molecules are still near each other, the probability for trap formation is increased with respect of a more random distribution of water and oxygen within the device. The voltage increase in the subsequent stressing cycle thus is higher than the voltage increase expected to be seen for a random distribution of water and oxygen. This effect was visible at low temperature and when we used light to de-trap electrons.

For rest times long enough, all generated trap sites will be deactivated, and the constituent molecules diffuse until they reach equilibrium positions. The plateau and dip observed in voltage (Figure 2.8b and Figure 2.9b) increase thus arise from trap formation starting at equilibrium distribution of water and oxygen within the device.

The behaviour of the device at lower temperatures is consistent with this picture. At lower temperatures, the diffusion of water and oxygen decreases substantially, and we expect diffusion coefficients for water at 270 K in the range of $1x10^{-8}$ to $1x10^{-9}$ cm^2/s, for oxygen between $4x10^{-8}$ to $9x10^{-9}$ cm^2/s. The values were calculated using an Arrhenius relationship and values for oxygen diffusion in P3HT [132] and water diffusion in nylon[134] - both at room temperature. Therefore, the probability of trap formation decreases at lower temperature, and the voltage rise thus is lower than observed at room temperature. Consequently, the voltage drop as a function of rest time is lower, since there are less trap states present which can decay. Also, since less thermal energy is available, the lifetime of the filled trap states increases substantially, as can be seen from the time needed for full recovery, increasing from 244 s at room temperature to 900 s at 270 K. However, the times required for the devices to fully recover are not consistent with thermal de-trapping as the only recovery process. For an assumed trap capture rate of $5x10^{-13}$ cm^3/s, a density of states of $1x10^{21}$ cm^{-3} and a trap energy of 0.7 eV, the calculated de-trapping time at RT (297K) for 63% de-trapping is 1511 s. At 270 K – assuming that the capture rate does not change with temperature – the time required for thermal de-trapping is 23'287s.

However, when repeating this experiment on a device with more trap sites present, we observed a further decrease in the recovery time (see S2.8) which hints at an electron release mechanism including the involvement of further trap sites via a trap-trap recombination process or additional pathways for complexes to dissolve. The presence of a further recovery mechanism is supported by the results from the current density dependent rest time experiment (Figure 2.8). Here we see a power law dependence of the observed voltage drop on the current density. The higher the

current density is, the larger the voltage drop became. If the recovery mechanism solely would depend on thermal de-trapping, we would expect to see an exponential decrease in voltage drop.

2.5.1 Simulation of trap site density
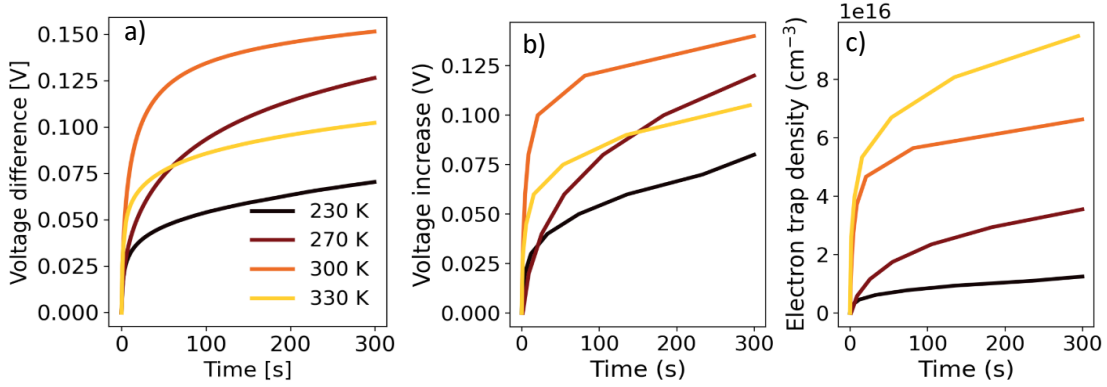
Figure 2.11 a) Voltage development of a SY device at different temperatures. b) Replication of the observed voltage behaviour using 1D drift-diffusion simulation. c) The resulting trap density extracted from the simulations in b).

It is not possible to directly infer the number of trap sites evolving during the increase of the observed voltage since the relationship between voltage and trap site density is not necessarily linear. This was already observed by Niu et al[120] during their investigation of hole trap sites in SY. Therefore, we generated a 1D SY stack in a drift-diffusion environment and recreated the steady state of the device at different times of the experiment (Figure 2.10a, for easier comparison, the Figure is displayed again in Figure 2.11 a). The resulting voltage increase vs time plot is displayed in Figure 2.11b). For the simulation at different temperatures, only the hole and electron mobility were adjusted. The capture rate was kept constant at $5x10^{-13}$ cm^3/s for both holes and electrons. From the simulations in Figure 2.11b), the trap site density can easily be extracted, giving a trap density evolution for electrons displayed in Figure 2.11c). The evolution of electron trap sites is strictly monotonously increasing with temperature. The higher the temperature is, the more trap sites develop. This is in contrast to the voltage increase observed in Figure 2.11a) where the voltage increase at temperatures above 300 K are smaller than at 300 K. The trap site density, which had to be added into the simulation in order to account for the increase in voltage are in a reasonable range and comparable to the number of traps measured in experiment[121].
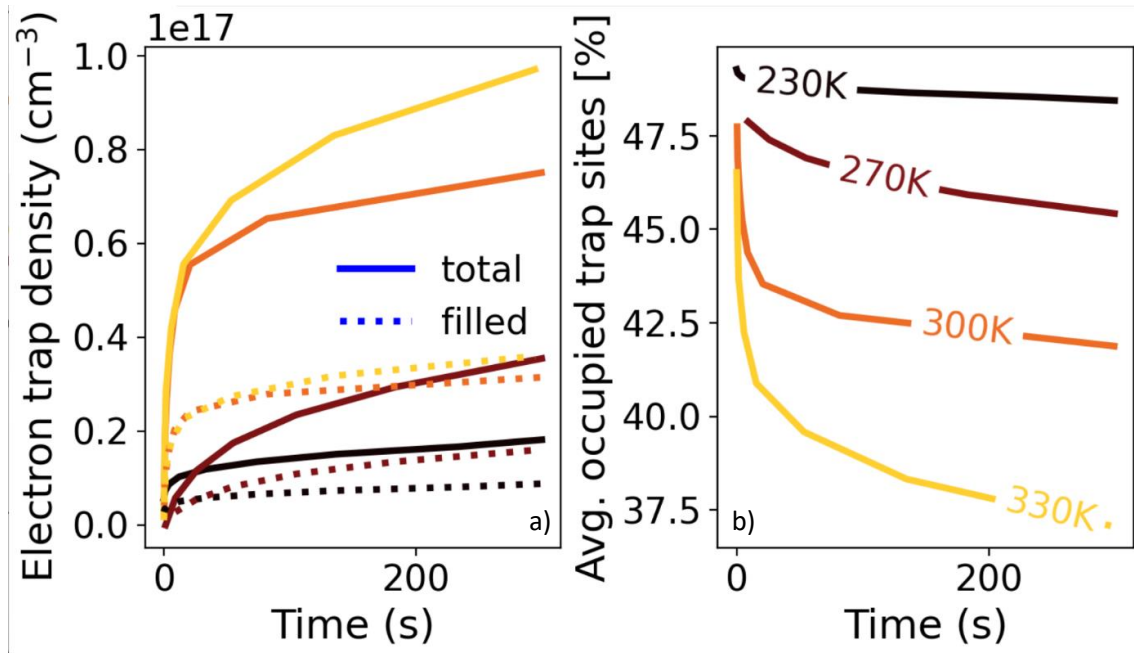
Figure 2.12 a) The electron trap density as calculated by the simulation for different temperatures (solid line). Not all trap sites are filled. An integration over the thickness of the active layer was performed to determine the average filled trap states per cm³ for specific times (dotted line). In b) the filled trap sites are expressed as percentage of total available states.

Drift-diffusion simulations usually have the total number of available trap sites N_t as an input parameter and calculate the number of filled trap states as an internal parameter according to $n_t = \frac{c_n n N_t}{c_n n + e_n + c_p p}$ (the emission of an electron from the HOMO into a trap state is here neglected since the energy needed for this process exceeds 1.85 eV and therefore does not occur during the duration of the experiment) with n_t the number of filled trap states, $c_{n,p}$ the capture rates for electrons and holes, respectively, n,p the number of free electrons and holes, respectively and e_n the emission of electrons into the LUMO. This is a good model for conventional trap sites. However, in the case of reversible trap states, a trap state only 'exist' when it is occupied by an electron. This means that $N_t = n_t$ for all temperatures. However, in the current drift-diffusion framework, it is not possible to set both parameters to equal. We therefore calculated the average number of filled trap sites for each temperature from the trapped electron profile at specific times. The averaging was done since the number of filled trap sites is not constant throughout the whole device. Trap sites located near the cathode usually are filled to a higher degree, since more free electrons are present. (see Figure S2.9).

The results from the calculations are displayed in Figure 2.12 a and b. The higher the temperature is, the lower is the trap occupation in percent. Also, the more trap sites are present, the less of the trap sites are filled. However, the total number of filled trap states increases monotonously with temperature and is highest for 330 K. The increase in N_t from a low temperature to a higher one is large enough to compensate for the smaller trap site occupation in percent at the higher temperature. This means that we can use the total number of trap sites to estimate the density of reversible trap sites in a device. The deviation between simulated total trap site density and the trap site density in the device is the factor $\frac{c_n n N_t}{c_n n + e_n + c_p p}$.

To simulate the SY-stack, several parameters are required which are difficult to determine experimentally and therefore have a large uncertainty associated with them. One set of such parameters

is the mobility of electrons and holes and correspondingly the capture rate which is related by $C_{n,p} = \left(\frac{q}{\varepsilon_0 \varepsilon_r}\right) \mu_{n,p}$. Also, some strong assumptions like the device being free of traps initially need to be tested. We used different mobilities and capture rates to investigate the dependence of the simulation on those critical input parameters.
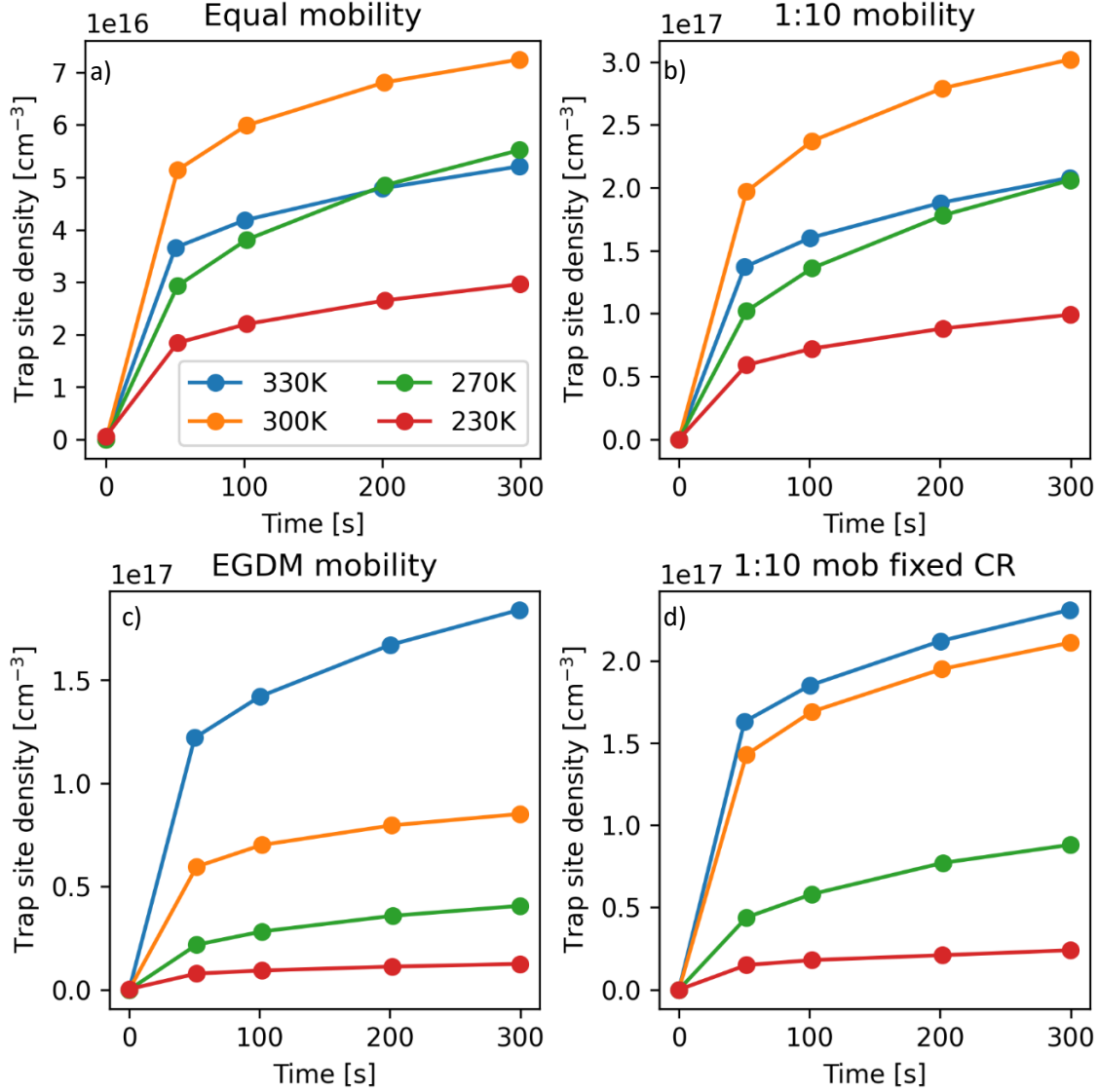
Figure 2.13 Electron trap site evolution when a) equal mobility of holes and electrons is assumed, b) the hole mobility is 10 times larger than the electron mobility, c) hole mobility values measured on bipolar devices and fitted with a EDG model are assumed and d) the case in b) but with a fixed capture rate of 5x10^-13 cm³/s for both holes and electrons is applied. As a basis for the simulation, the data from Figure 2.10a) were used.

In Figure 2.13 the resulting electron trap density for different assumptions concerning the hole and electron mobility is displayed. In a) it is assumed that no initial trap sites are present, and the mobility of holes and electrons is equal. For the different temperatures, hole and electron mobility as well as the capture rate were adjusted (see orange curve in Figure 2.14 for the values of the mobilities). Both mobilities and the capture rate increase monotonously with temperature. For a mobility chosen such way, the largest increase in trap site density is found at 300 K while the trap site density at 330 K is even lower at the end of the experiment than at 270 K.

A similar trend can be seen when a ratio of 1:10 between electron and hole mobility is chosen (Figure 2.13 b), while the capture rate is coupled to the mobility. The mobility of the electrons and

therefore the electron capture rate is lower than in case a). The SRH recombination is thus less significant, and the trap sites do have less impact on the device. This is reflected by the increased number of trap site which must be added in the simulation to see an influence on the device. The number of trap sites is up to a factor of 3 higher than for the simulation case with equal mobilities.

If the capture rate is not coupled to the mobility and instead takes on the value of 5×10^{-13} cm^3/s, we see a higher trap site evolution for 330 K than for 300 K (Figure 2.13d). The same trend as in Figure 2.13d) is visible in Figure 2.13c) where the hole mobility was determined from SCLC measurements on a bipolar device and recreated using an extended gaussian disorder model (EGDM). However, in order to be able to apply the experimental hole mobilities, an electron mobility trend had to be chosen which decreases with temperature (see Figure 2.14b). The mobility values extracted from two different devices were used. Though the trend for the electron mobility decrease with temperature does not change. Usually, it is assumed that mobility in organic semiconductor increases with temperature. The reason for this is the increased injection of charge carriers and increased hopping rates at higher temperatures, which increases the charge carrier density. EGDM is dependent on charge carrier density. The difference in mobility, that is expected to occur due to the use of different mobility models is shown in S2.11

However, in the simulation the EGDM mobility cannot be used in conjunction with SRH recombination. This means for simulations using EGDM no trap assisted recombination mechanisms are included. The missing effect has to be emulated by changing other parameters. The change of electron mobility is one way. The effect of SRH recombination is most prominent at low voltages as were applied at high temperatures (3.2 V at 330 K vs 5.05 V at 230 K). Therefore, changes to the electron mobility need to be more pronounced at higher temperatures. This can be seen as a higher reduction of electron mobility at high temperature than at lower temperature. Decreasing the electron mobility has the effect of increasing the number of free charge carriers. The additional charge carrier present in the simulation are the fraction that would recombine via SRH.

Note, the numbers displayed here correspond to N_t from the drift-diffusion and therefore are higher than the number of filled trap states.

Figure 2.14 a) the hole mobility values used for the different simulations, and b) corresponding electron mobility values.

Conventional trap filling time is only dependent on the relative ratio between trap filling and trap emptying events. Only the emission from the trap sites is implicitly dependent on the trap depth

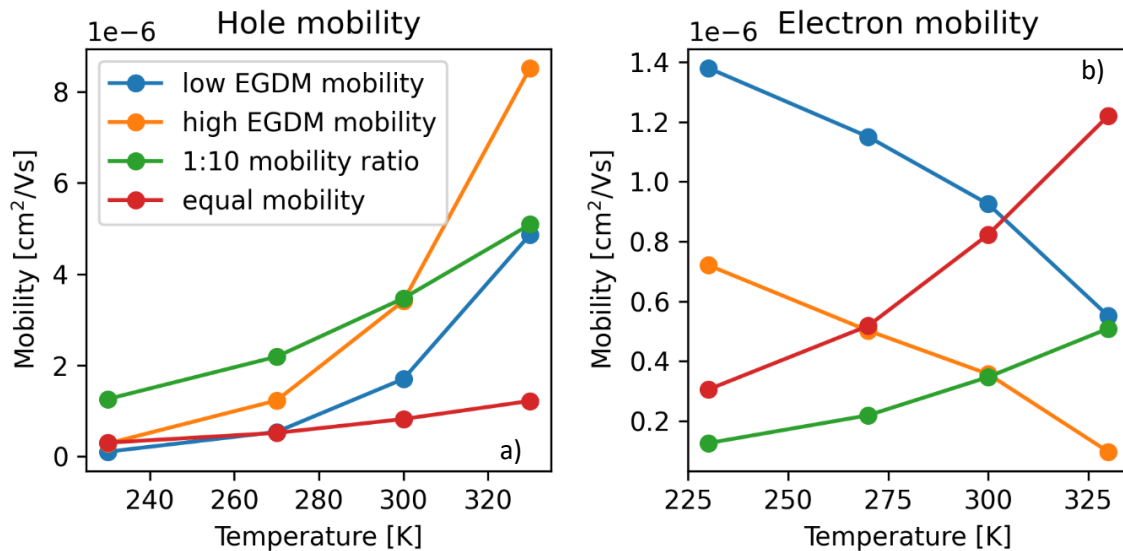and temperature. Emission from deep traps can be neglected for trap filling experiments since its time frame is much longer than the filling itself. This means the filling of deep trap sites should be nearly as fast as for more shallow trap sites (see calculation in SI). Measurements showed that deep trap sites in superyellow PLEDs fill within 200 μs[119]. However, the effects we found in our experiments exhibited a time frame of minutes to hours and thus is not explained by mere trap filling.

The mobility of the electrons has a large influence on the number of trap sites which must be added in the simulation. If the electron mobility is very small, it is unlikely that a trap site in the simulation is occupied. The ratio of filled to total trap sites is therefore small and thus a high numbers of trap sites must be added into the simulation.

The simulation shows that there is a large dependence of the required trap sites on the capture rate, the mobility of the charge carrier and the temperature. The dependence on those parameters is large enough to change the trends in the number of trap sites which must be added in the simulation in order to achieve 10 mA/cm^2. If the capture rate is fixed as a constant the highest number of trap sites generated is at 330 K. For other mobility models used or mobility dependent capture rates are applied, the largest trap site generation takes place at 300 K.

It stands to reason whether the capture rate of the trap states should be coupled to the mobility of the charge carriers or whether fixing it at a reasonable constant value is more accurate. The formation of the water-oxygen complex is much lower (seconds to minutes) than the filling of empty trap sites (microseconds). On the time scale of complex formation, the capturing of an electron can be thought of as an instant process if enough free electrons are available. In a steady state drift-diffusion simulation, the capture rate in combination with the emission rate gives the percentage of filled trap sites. Since the capture rate is dominating the term (emission is comparatively small and takes hundreds of seconds while capture rate has a time scale of microseconds) and trap states only exist if they trapped an electron, we could assume that 100% of the trap sites are filled.

2.6   Conclusion

We observed a drop in performance of a SY light-emitting diode upon running it at a constant current density for as little as 5 minutes. This performance drop is reversible, and the device recovers fully within a time frame dependent on the temperature if let to rest at short circuit conditions or illuminating it with light of a wavelength of 830 nm. The timeframe of seconds to minutes for the performance reduction cannot be explained by the mere filling of trap sites present in the device, Joule heating or the presence of mobile ionic impurities.

Instead, we proposed that the dynamics of the formation and decay of a notoriously famous kind of deep trap – namely reduced water-oxygen complex – is responsible for the observed effect. We believe that the water and oxygen molecules only form trap states if an external field is applied, and that these trap states decompose once the device is turned off. This contrasts the general belief that such trap states are permanent and present upon device fabrication.

In order for deep traps based on water-oxygen complexes to decompose, the trapped electron has to be removed. We propose the presence of at least two possible pathways for the removal of trapped electrons. At high temperatures, there is enough energy present for charge carriers to detrap thermally within a reasonable time. At lower temperatures, other de-trapping mechanisms like trap-trap recombination are dominant. The presence of trap-trap recombination is supported by experiments on samples with lower quality (i.e higher driving voltage needed). They exhibit a

shorter recovery time at low temperatures than samples with a higher quality. It is likely that in low quality samples the number of hole trap sites is substantially larger than in good quality samples – promoting trap emptying via trap-trap recombination.

We investigated the temperature and current density dependent response of SY-PLEDs and found the resulting observation to support our thesis about the reversible trap states. The slowdown of device recovery for lower temperatures is consistent with a decrease in oxygen and water diffusion. Also, the lower voltage increase for large break times can be explained by a trap formation starting at equilibrium distribution of water and oxygen molecules as opposed to more accumulated distributions at lower rest times.

Experiments could be modelled but it turned out that the simulated trap-vs-time-vs-temperature depends strongly on the input parameters. Especially the mobility values for electron and holes and correspondingly the respective capture rates have a strong influence on the simulation outcome. It is intrinsically difficult to determine the simulation input parameter with the precision required to make sensible estimates for the trap density. It is a commonly known issue in the determination of for example charge carrier mobility[135] that the uncertainty in the measured parameter may exceed one order of magnitude. The uncertainties in the input parameter were too large to reliably determine absolute numbers for the trap states present within our devices. However, we could show the trends of trap evolution for different temperatures. The higher the temperature is, the more trap states form within the device for the same period of time.

Further investigation regarding the trap formation and decay needs to be done. Diffusion of oxygen and water within SY needs to be studied.

2.7 Supporting information

2.7.1 Structure of PEDOT:PSS
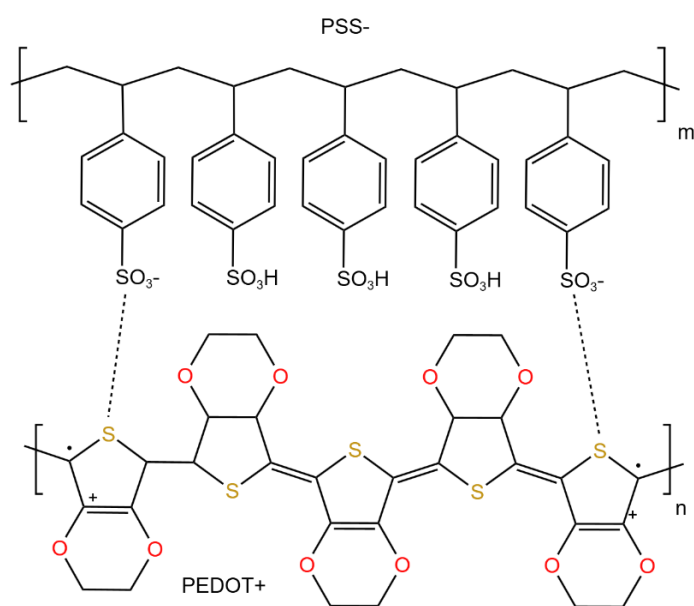
S2.1 Structure of PEDOT:PSS

Poly(3,4-ethylenedioxythiophene) doped with poly(styrenesulfonate) known as PEDOT:PSS. This material has been used as a solution-processable hole conductor. It is transparent, exhibits a high mobility for holes and a high ductility and is easy to process.[136]

2.7.2 Measurement steps for temperature dependent experiments
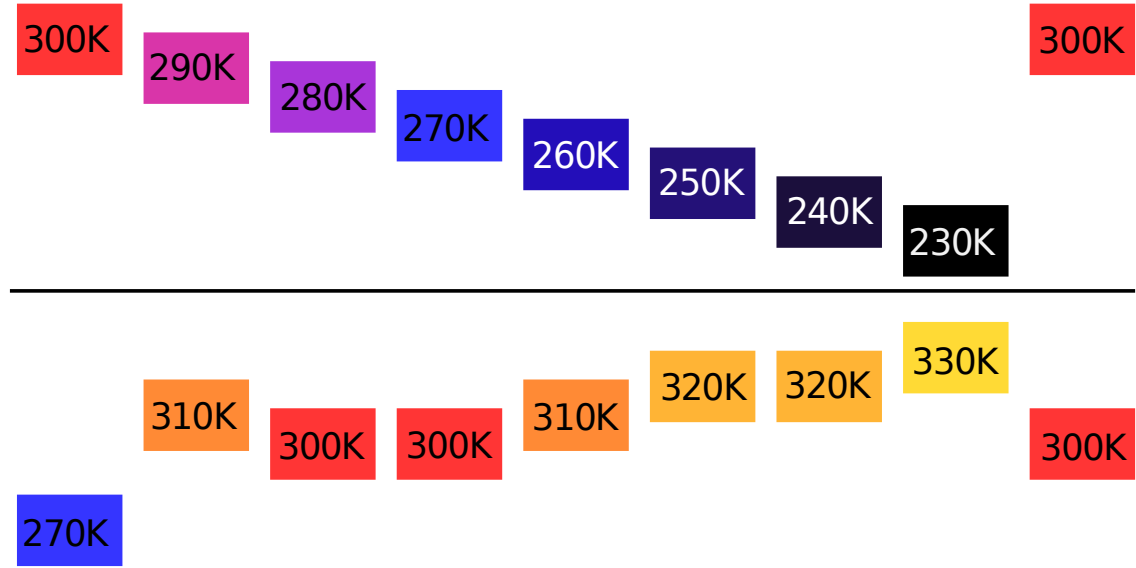
S2.2 Temperature cycle used for the temperature dependent stressing in the main text. The progression starts top left, goes to top right and then continues on the bottom left ending in the bottom right.

In order to prevent increased deterioration of the device, first the influence of low temperatures on the device voltage behaviour was measured. The applied temperature cycle is displayed in S2.2. Especially at high temperatures, multiple measurements were done at the same temperature in order to assess the device deterioration. For long breaks in between the measurements, the device performance recovered fully and thus no permanent deterioration was observed.

2.7.3 Calculation of trap filling time

The change in trap site occupation is given by trap filling and trap emptying processes according to

$$\frac{dn_t}{dt} = c_n * n * (N_t - n_t) - e_n * n_t - c_p * p * n_t$$

where n_t is the number of occupied trap sites, $c_{n,p}$ is the electron or hole capture rate, respectively, e_n the electron emission rate, N_t the total number of trap sites present, n the number of free electrons in the device and p the number of free holes in the device. The first term describes the capturing of a free electron in the LUMO, the second term gives the thermal emission of a captured electron into the LUMO and the last term stands for the rate of filled electron traps capturing a free hole from the HOMO i.e release of the electron into the HOMO (Shockley-Read-Hall recombination). This equation can be rewritten as

$$\frac{dn_t}{dt} = c_n * n * N_t - n_t * (c_n * n + e_n + c_p * p)$$

Which corresponds to a differential equation with the form

$$\frac{dx}{dt} = -ax + b$$

With $x = n_t$, $a = c_n * n + e_n + c_p * p$ and $b = c_n * n * N_t$

The solution to this differential equation is

$$x(t) = \frac{b}{a} + c_1 e^{-at}$$

Using initial conditions x(t=0) = 0 we get

$$n_t(t) = \frac{b}{a}(1 - e^{-at})$$

The time needed to approach equilibrium conditions i.e. $\frac{dn_t}{dt} = 0$ can be estimated by setting $t = \frac{4}{a}$. This time corresponds to a case where 98.2% of the time needed to reach equilibrium has passed. For a deep trap, $e_n = c_n * N_{0,n} * \exp\left(\frac{-E_t}{k_B T}\right)$ can be neglected since the thermal de-trapping probability has an exponential dependency on the trap depth E_t, giving $a = c_n * n + c_p * p$. $N_{0,n}$ is the density of LUMO states. With a capture rate of $c_n=c_p=5\times10^{-13}$ cm³/s, a total trap density of 1×10^{17} cm^{-3} and an average density of free charge carriers of $n=p=2\times10^{16}$ cm^{-3} we get a filling time of 200 µs.

For trap sites with an energy below 0.3 eV, emission is significant and thus must be considered. At 300K and with an energy of 0.25 eV for the trap sites, the filling time is 78 µs.

2.7.4 Effect of initial trap site density >0 on the simulation
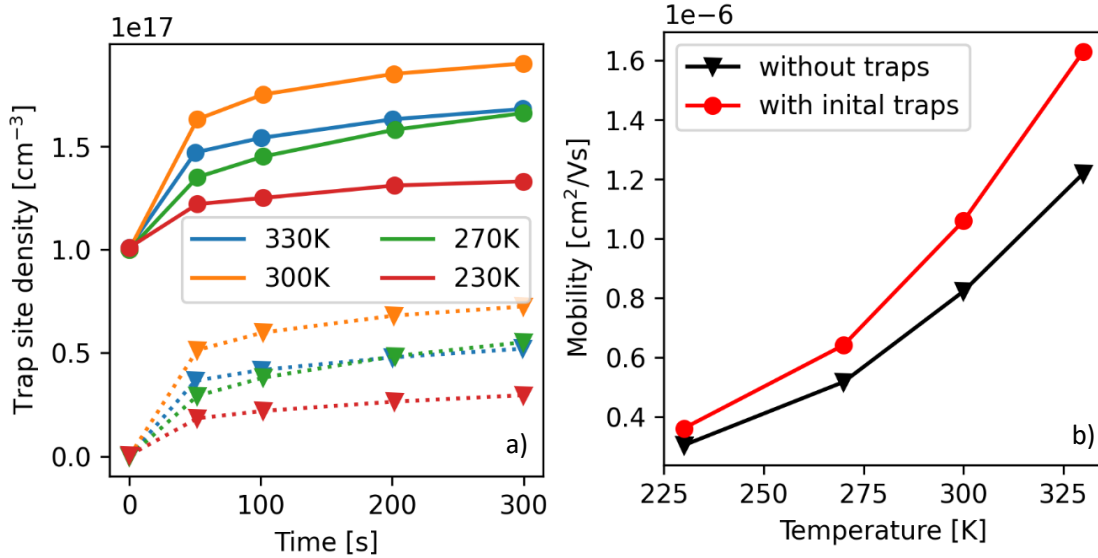
S2.3 a) Trap site density at different stress times for different temperatures. Two cases were investigated. In one case, there are no initial trap sites present (triangle marker), in the other case an initial trap site density of 1x10^{17} cm^{-3} was assumed (round marker). b) Displays the mobilities used for holes and electrons as a function of temperature for the case without any initial trap sites (black line, triangle marker) and with initial trap site density of 1x10^{17}cm^{-3} (red, round marker).

Figure S2.3a) displays two simulations for the evolution of a trap site density with stressing time for a device at 330 K, 300 K, 270 K and 230 K. The difference between the simulations is the assumed initial trap site density which is 0 for one simulation and 1×10^{17} cm^{-3} for the other simulation. The input parameter besides initial trap site density are described in Table 2.1. The capture rate for the trapping of electrons in the deep trap and for SRH recombination is coupled to the charge carrier mobilities via $C_{n,p} = \left(\frac{q}{\varepsilon_0 \varepsilon_r}\right)\mu_{n,p}$. The mobilities chosen for holes and electrons are equal. The simulations were generated following the procedure described in the main text.

The trend in trap evolution is the same for both simulations with the highest amount of trap states generated at 300 K. For the case with 1×10^{17} cm^{-3} initial trap sites, the number of trap sites which have been generated at t=300 s in addition to the ones present at t=0 is 12 to 30% higher than for

the case of no initial trap sites. However, this can be explained by the different mobility used for both cases. In order to achieve 10 mA/cm^2 in the simulation with initial trap sites, the mobility of holes and electrons was increased by 18 to 33% (see S2.3) as compared to the case without initial trap sites present. Without this adjustment, the current density in the simulation would be below 10 mA/cm^2 since free charge carriers are trapped and recombine via SRH reducing the total number of free charge carriers. The presence of a substantial number of trap sites in a device can thus be compensated by a low increase in mobility of a factor less than 1.5.

2.7.5   Recovery time of a device
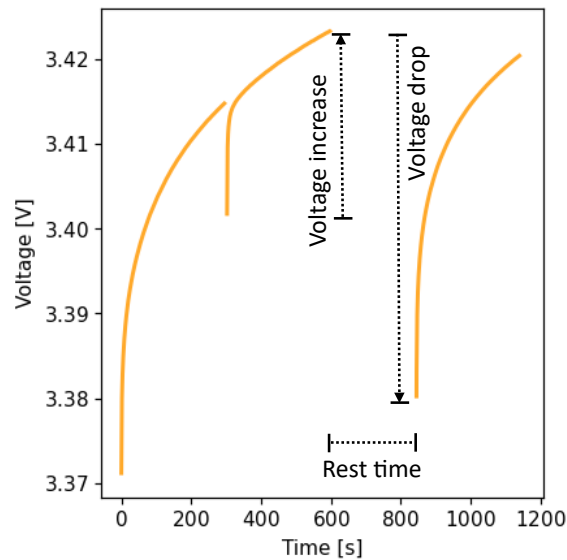
S2.4 Stressing series at room temperature with 3 stressing cycles at 10 mA/cm^2 with a duration of 5 minutes each and a rest time of 3.8 and 244 seconds, respectively, in between. Marked are the ranges making up the voltage increase during one stressing cycle, the voltage drop during the rest time and the rest time. The voltage drop during the break can by larger than the voltage increase during the previous stressing cycle if the break is long enough.

Marked in S2.4 is the graphical definition of 'voltage increase' and 'voltage drop' as used in the main text.

It is anticipated that the voltage drop will stabilise over long rest periods, as the number of electron trap states created during a 5-minute stress period is limited, leading to a finite number of states that can decay during rest periods. However, in the experiment described in the main text, the voltage drop does not level off due to the carryover of non-decayed electron trap states from short rest periods to the next stress cycle. This results in an increased number of initial trap states and thus higher initial voltage in a subsequent stress cycle. The number of excess trap sites accumulates with short rest periods and decays during long rest periods. This is demonstrated in S2.4, where the voltage increases during the first stress cycle due to formation of electron trap sites, but not all electron trap sites decay during the short rest period. Consequently, the remaining electron trap states lead to a higher initial voltage in the subsequent stress cycle, resulting in more overall trap states than can be generated during one stressing cycle. Therefore, the number of decaying trap sites during a long rest time is higher than the number of trap sites developed during one stress cycle. This device history thus prevent levelling of the voltage drop in the experiment from

the main text. The voltage increase in stress cycles after a short break is less pronounced due to slower trap site formation.

2.7.6 Trap emptying trend
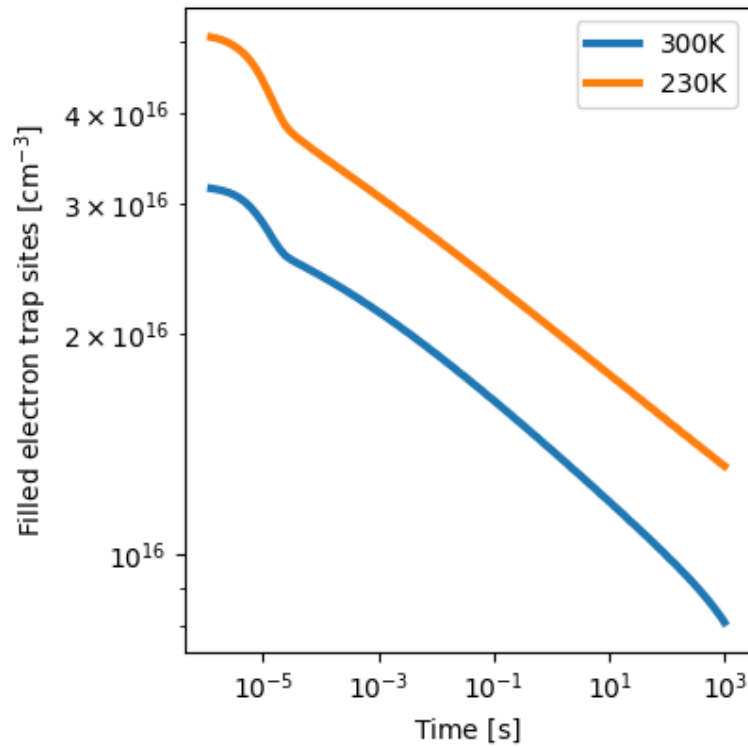
S2.5 Trap emptying at 0V as a function of time for 300K (blue) and 230K (orange). The trap site density corresponds to an averaged value across the whole device.

In S2.5 displayed is a simulation for the trap emptying as a function of waiting time. The device started from steady state with a constant current of 10 mA/cm^2 and a constant trap site density of 2x10^{17} cm^{-3}. At t =0.2 us, the device was set to 0V and the transient behaviour up to t=1000s was simulated. Since the number of occupied trap sites in a device is strongly dependent on the position within the device (see S2.10), an average trap occupation was calculated using the geometrical mean. After initial emptying of trap sites due to recombination with residual free holes, the trap emptying exhibits a power law trend for 300K and 230K. At late times (t>300s) thermal de-trapping start to occur for the case at 300K. At this time the trap emptying process deviates from a power law behaviour. The main contribution for the observed de-trapping originates from SRH recombination. The free holes required for the recombination process come from injection at the anode and subsequent diffusion towards the cathode. It can be argued that the limiting step of trap state decay is the de-trapping of the trap states.

2.7.7   Processes involved in de-trapping via light
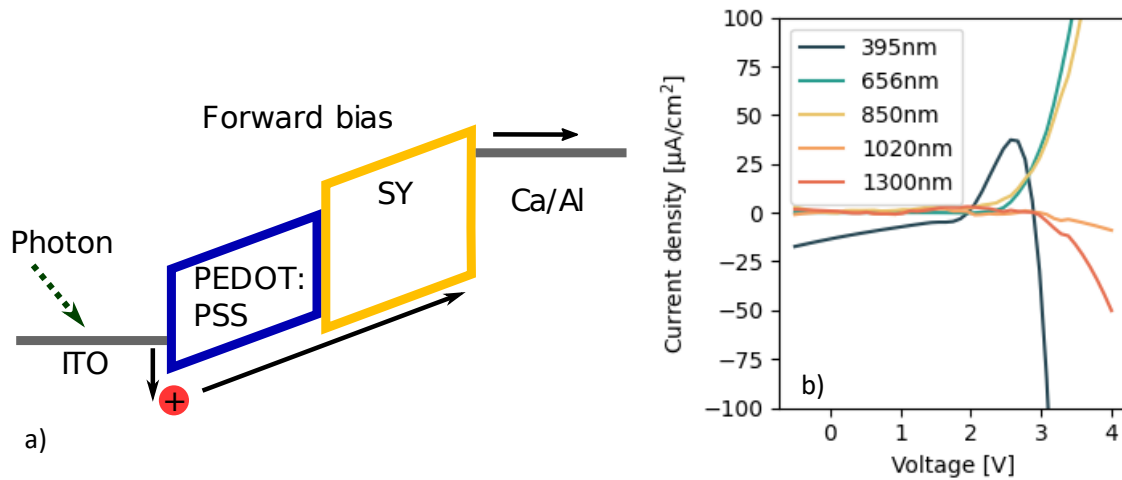
S2.6 a) Schematic representation of internal photoemission. Under forward bias light of appropriate wavelength is absorbed at the ITO and stimulates the injection of holes into the device. The holes are transported across the device and extracted at the cathode. b) current-voltage plot arising due to illumination of the device with light of different wavelengths. Charge carrier extraction leads to a negative current while injection takes place at positive current.

When the device is illuminated with light of appropriate wavelength, the electrodes absorb some of the photons and inject charge carriers into the device. This process is called internal photoemission and can be used to determine injection barriers at the metal-semiconductor layer. Whether a hole is injected at the anode or an electron at the cathode is determined by the bias direction (forward, reverse) and the type of the semiconductor (hole transporting or electron transporting)[137]. For a device based on SY, holes are injected under forward bias (S2.6a). The holes are transported across the device and extracted at the cathode. However, when there are filled electron trap sites present -as is the case after stressing experiments - some of the holes recombine with the trapped electrons. This effect can be used to decrease the recovery time for the device since de-trapping is increased. Depending on the wavelength of the light used for illumination, different processes take place. The effects of those processes on a current-voltage curve are displayed in S2.6b. For this plot, two JV curves were measured. One under dark condition and the other under illumination. The dark JV curve then was subtracted from the JV curve under illumination. Wavelengths between 370 and 500 nm are absorbed in the SY layer and lead to the generation of bound charge carrier pairs. Under reverse bias and at high forward bias, those charge carriers can be separated and extracted, giving a negative current density. Since both kinds of charge carriers are present, the rate of trap emptying cannot be increased at those wavelengths. Light between 650 and 860 nm is absorbed by the electrodes and leads via the internal photoemission to an injection of holes (positive current) into the device under high forward bias. At wavelengths between 1200 and 1400 nm – corresponding to an energy between 1 and 0.88 eV the trapped electrons can be optically de-trapped giving a negative extraction current under high bias. Both latter ranges of wavelengths are suitable to decrease the recovery time of the device.

2.7.8 Distribution of free electrons
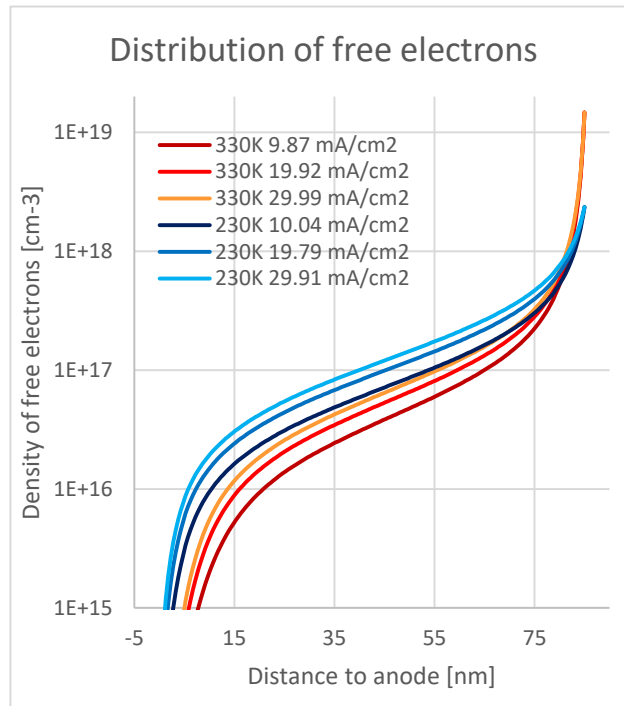
S2.7 Distribution of free electrons inside the active layer with 0 nm the position of the anode and 85 nm the position of the cathode. Displayed in blue are three electron densities for an applied current of about 10, 20 and 30 mA/cm² at 230 K. In red, the free electron density at 330 K is displayed for the same three different current densities.

The number of free electrons inside a device is dependent on the position within the device, the applied current density, and the temperature (and therefore also the mobility). The closer free electrons are to the cathode, the more are present. By getting closer to the anode, the free electron density decreases by several orders of magnitudes. Decreasing the temperature or increasing the current density both can increase the free electron density by a factor of 2.

Except for the case of low temperature and high current densities, the average of the free electron density is below $1x10^{17}$ cm^{-3}. Since the content of water in polymers can reach $1x10^{18}$-$1x10^{19}$ cm^{-3} [38]and the oxygen content is around $1x10^{18}$ cm^{-3} .It is argued that the availability of electrons is the limiting factor for the evolution of reversible trap states. Note though that the water and oxygen content were measured for P3HT and values for SY do not exist.

2.7.9   Influence from age of the device
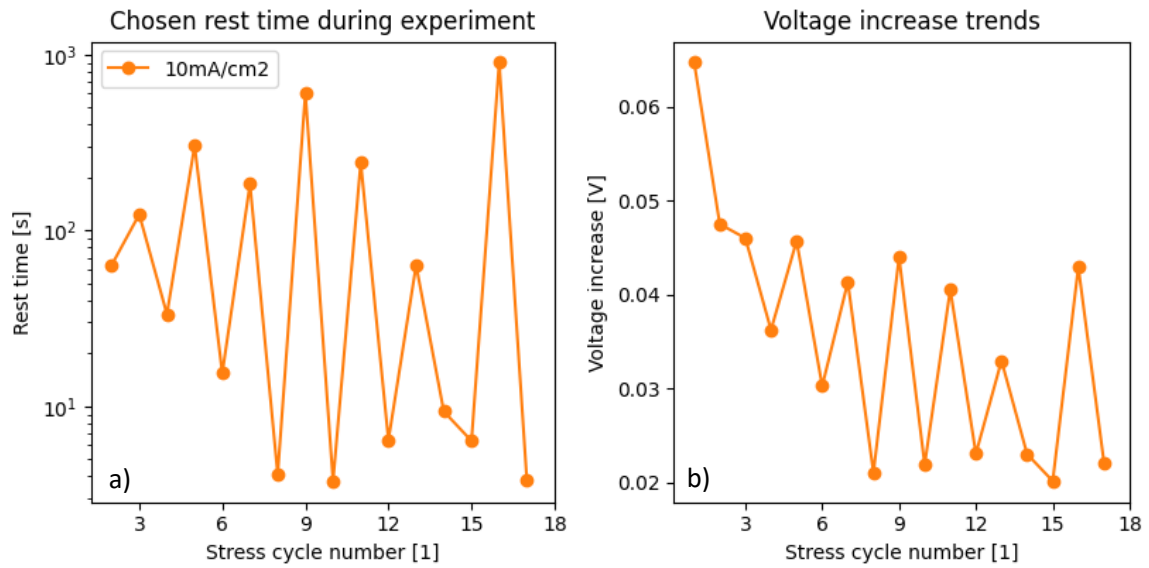
S2.8 distribution of free electrons inside the active layer with 0 nm the position of the anode and 85 nm the position of the cathode. Displayed in blue are three electron densities for an applied current of about 10, 20 and 30 mA/cm² at 230 K. In red, the free electron density at 330 K is displayed for the same three different current densities.

To see a clear trend in the stressing experiments, the rest times between the stress cycles were chosen to not increase linearly (S2.8a). This allows to decouple the age of the device represented by the cycle number from the increase in voltage. As can be seen in S2.8b, the voltage increase depends on the rest time and not the device age. The only exception can be seen in the first three cycles where the influence from burn-in still is visible as a higher voltage increase than expected for the chosen rest time. To prevent this behaviour in the measurement, preconditioning of devices was introduced for all further experiments.

2.7.10   Effect of higher trap density on device recovery
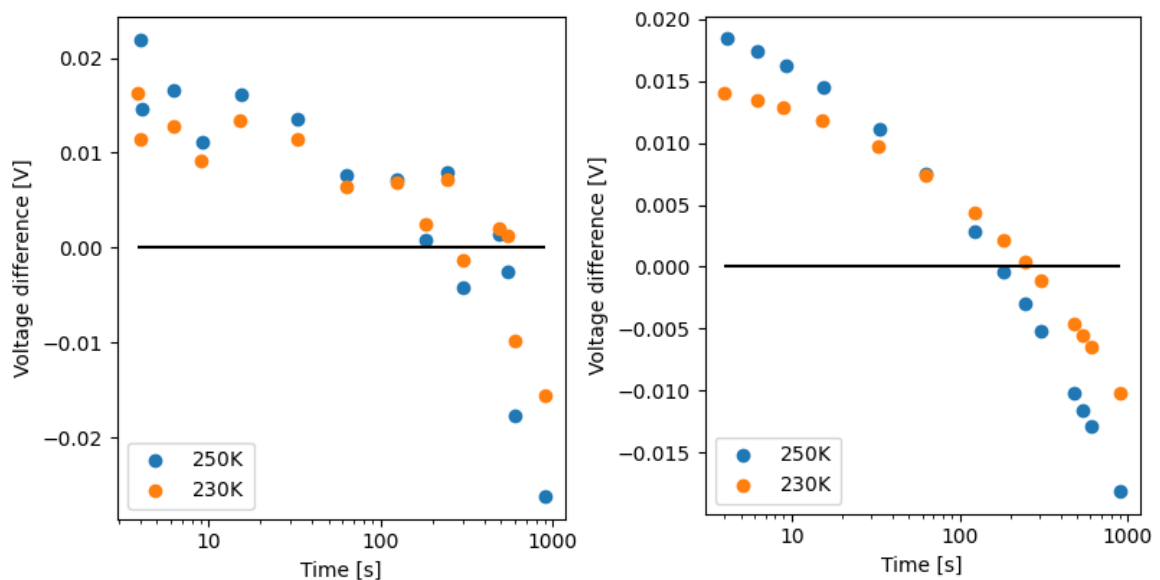
S2.9 a) Difference between voltage increase and voltage drop as a function of rest time for two different temperatures. b) Fit of the data presented in a) to show the trends more clearly.

S2.9 displays the difference between the voltage increase and the voltage drop for subsequent stressing cycles as a function of resting time for two different temperatures, 230 K and 250 K. To

present the trends more clearly, the data has been fitted in b). The device used for this measurement had a lower quality as the devices shown in the main text – the driving voltage to reach 10 mA/cm^2 was 3.9 V as opposed to 3.52 V. Also, the combined electron and hole mobility is lower (1x10^{-5} vs 7x10^{-5} cm^2/Vs). The worse parameters hint to the presence of more trap states in this device than found in the devices used in the main text. The trend exhibited by this device for the voltage increase and the voltage drop follow the trend exhibited by the device in the main text. The increase in voltage is more pronounced at higher temperatures, as is the voltage drop. However, the absolute change in voltage is larger for the sample with lower quality. Remarkably, the times required for the devices to fully recover is substantially reduced compared to the device in the main text. For 250 K, 180 s are required while for 230 K 250s are sufficient. The device in the main text required 900 s at 270 K to fully recover. We reason that the presence of more trap states – especially trap states with an affinity for holes – reduce the recovery time of the device. This can be achieved by a trap-trap recombination pathway, where a trapped electron can recombine with a trapped hole if both are within a reasonable distance.

2.7.11 Trap occupation as a function of position

Density of trapped electrons
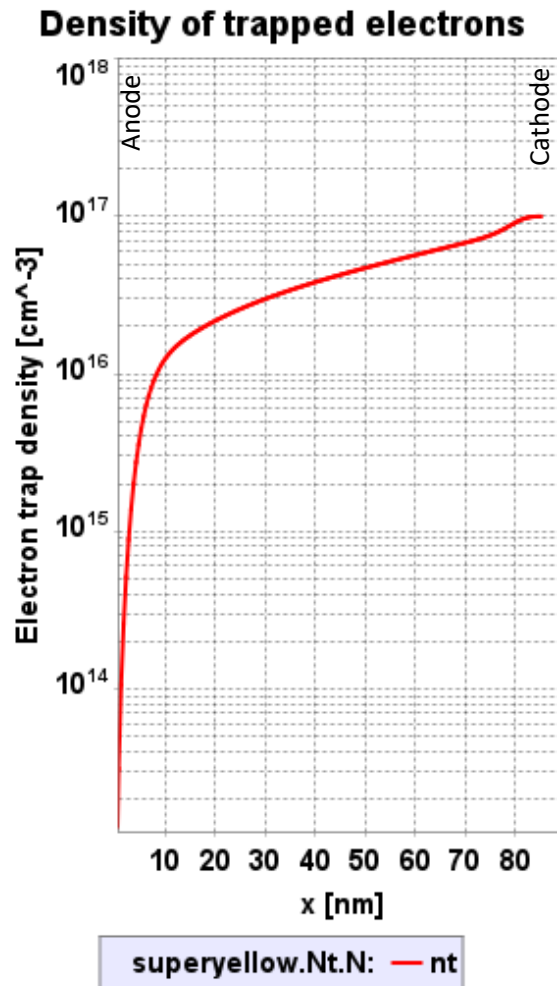
S2.10 Profile of trapped electrons at t=300 s, T=330 K, and N$_t$=1x10^{17} cm^{-3} trap sites. At the anode side, the number of filled trap sites is smaller than at the cathode side.

S2.10: Distribution of filled trap sites across the device. The closer the trap sites are to the cathode, the more of the trap sites are filled. Close to the anode, the density of filled trap sites decreases by several orders of magnitudes. The average of the filled trap states is obtained by integration over the whole device. Trap sites close to the cathode cannot be emptied since electrons diffusing from the cathode will fill them again.

2.7.12 Impact of the choice of mobility
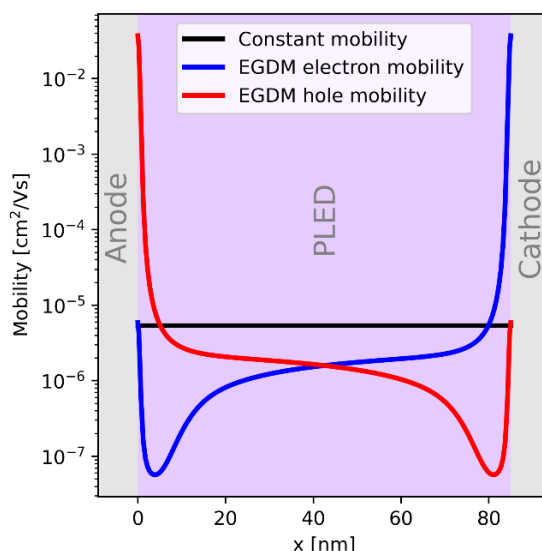
S2.11 EGDM and constant mobility for a simple simulation stack. Both simulations yield the same current for the voltage applied.

In drift-diffusion modelling, the application of a constant mobility as opposed to the EGDM mobility reduces the calculation time. Also, more complex mobility models are not implemented for all simulation modes. This restriction also applied to the combination of EGDM and Shockley-Read-Hall recombination in transient simulations. We therefore mainly applied the constant mobility model and only used EGDM for specific simulations to estimate the error introduced due to this simplification. At the electrodes, mobility as calculated from the EGDM deviates strongly from the constant mobility. However, the EGDM mobility only slowly changes in the bulk of the material. It is therefore possible to choose a constant mobility that represents an average of the EGDM mobility within the bulk. It is expected that the difference between the two models are smaller for thicker devices where the bulk is dominating.

Chapter 3: Upconverter devices based on superyellow as emitting layer

On the Response Speed of Narrowband Organic Optical Upconversion Devices

Wei-Hsu Hu[1,3], Camilla Vael[2,3], Matthias Diethelm[1,3], Karen Strassel[1,3], Surendra B. Anantha-raman[1,3], Abdessalem Aribia[4], Marco Cremona[5], Sandra Jenatsch[2], Frank Nüesch[1,3], and Roland Hany[1]*

[1] Empa, Swiss Federal Laboratories for Materials Science and Technology, Laboratory for Functional Polymers, 8600 Dübendorf, Switzerland
[2] Fluxim AG, Katharina-Sulzer-Platz 2, 8400 Winterthur, Switzerland
[3] EPFL, Institute of Materials Science and Engineering, Ecole Polytechnique Fédérale de Lau-sanne, Station 12, 1015 Lausanne, Switzerland
[4] Empa, Swiss Federal Laboratories for Materials Science and Technology, Thin Films and Photo-voltaics, 8600 Dübendorf, Switzerland
[5] Optolectronic Molecular Laboratory, Physics Department, Pontifical Catholic University of Rio de Janeiro (PUC-Rio), Rio de Janeiro 224543-970, Brazil

* corresponding authors: roland.hany@empa.ch

Declaration of contribution

C.V. contributed to the project by generating the upconversion simulation stack, performing drift-diffusion simulations, thoroughly analyzing the simulation data, and fitting it to the measurement data.

In this chapter, the simulation of upconverter devices and the analysis of the profiles is expanded in more details than in the paper Hu, W.-H., Vael, C., Diethelm, M., Strassel, K., Anantharaman, S. B., Aribia, A., Cremona, M., Jenatsch, S., Nüesch, F., Hany, R., On the Response Speed of Narrow-band Organic Optical Upconversion Devices. *Adv. Optical Mater.* 2022, 10, 2200695. https://doi.org/10.1002/adom.202200695. Data used from the paper with permission from copyright holder © 2019 WILEY-VCH Verlag GmbH & Co. KGaA.

3.1   Introduction

Upconverter devices

The perception of the human eye is limited to light from the visible spectrum with a wavelength between 380 to about 750 nm. However, light with wavelength beyond 750 nm (NIR near infrared, SWIR short wave infrared and MIR mid-infrared) can provide vital information about various processes and effects ranging from monitoring environmental pollution to night vision goggles, animal warning systems in automobiles, machine vision systems and functional bio imaging [138]. We therefore need a way to convert the infrared light to a signal which can be read out electrically or optically. A commonly chosen approach gaining more popularity is the serial combination of a photodetector with a sensitivity in the range of 1000 nm (NIR) with an emissive layer which emits in the visible spectrum. Thereby, a NIR scene can be directly converted into a visible image[139][140][141]. In this work, we combine a NIR cyanine dye photodetector with a fluorescent superyellow polymer light emitting diode (PLED) to fabricate a so-called all-organic upconversion device (OUD). Contrary to OUD reported in literature, we observed a decrease in response speed with increasing applied

voltage. We use drift-diffusion simulation to understand the processes governing the behaviour of the OUD and use the gained insight into the device operation to suggest some improvement to the design of the OUD.
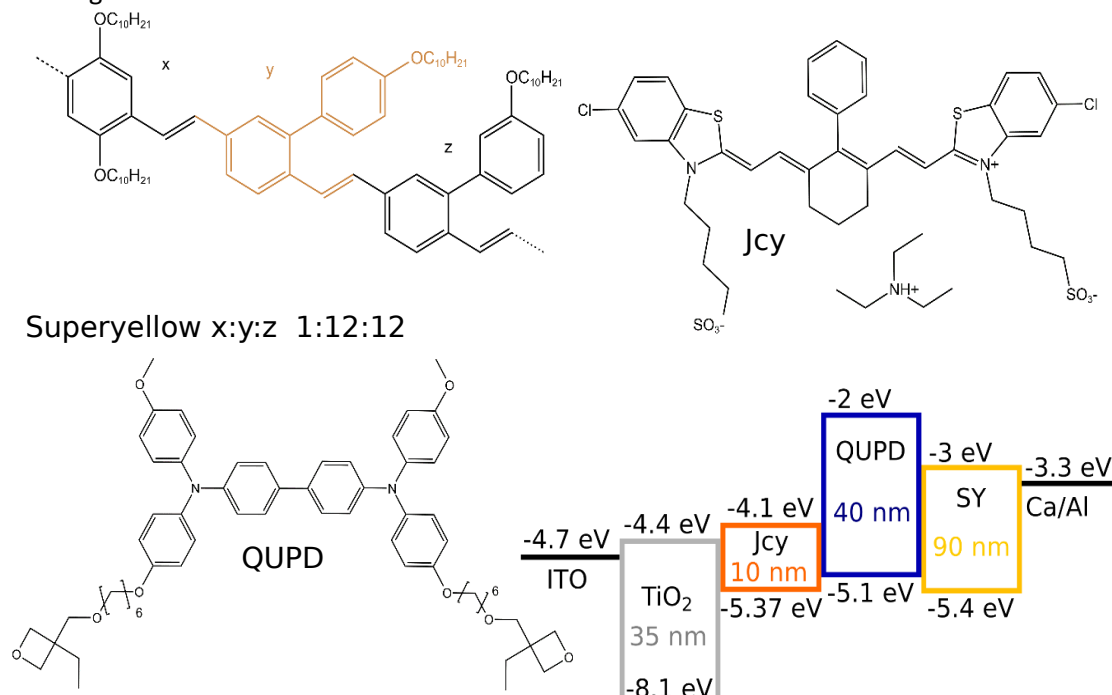
Figure 3.1 Chemical structure of the organic components. Top left superyellow (SY) the light-emitting layer. The y polymer block is displayed in brown to facilitate the distinction between the three polymer building blocks. top right a heptamethine J-aggregated polymethine cyanine dye for generation of charge carriers, bottom left QUPD a electron blocking layer and bottom right the full stack of the upconverter device with corresponding layer thicknesses and frontier orbital energy levels.

3.2 Materials and methods

3.2.1 Preparation of the devices

The device consists of a transparent ITO anode, a TiO_2 layer to block the injection of holes into the device, a heptamethine J-aggregated polymethine cyanine dye (Figure 3.1b (referred to as Jcy)) for the absorption of NIR light and generation of charge carriers, a QUPD layer (Figure 3.1c) which blocks the drift of electrons and a superyellow (SY) layer (Figure 3.1a) where recombination of charge carrier under the emission of photons takes place. The cathode consists of a calcium layer which is covered by an aluminium layer to ensure a better contact and protect the calcium layer. The stack architecture of the device is displayed in Figure 3.1d.

Jcy coated from 2,2,2-tri-fluoroethanol exhibits a narrow absorption band in the NIR spectrum with a full width at half maximum (FWHM) of 52 nm and a peak absorption at 995 nm (S3.1a). The light emitted from a superyellow PLED. in the configuration ITO/QUPD/SY/Ca/Al has a peak at 552 nm and a FWHM of 100 nm (S3.1b). In a full upconverter device, the NIR photodetector based on Jcy and the superyellow PLED are combined. Our device reached highest efficiency converting 980 nm light to yellow visible light and exhibited a FWHM of 130 nm [142].

Since the absorbance spectrum of Jcy is very narrow and only in the IR region, the visible light emitted from the SY layer is hardly reabsorbed in the Jcy layer (the device transmittance in the visible was 85%). This allows to build a device where the emitted light exits on the same side as

the infrared light enters. Therefore, it is possible to use an opaque electrode at the cathode side, facilitating device fabrication.

The preparation and the measurement of upconverter devices was carried out by Wei-Hsu Hu and is described elsewhere [142].
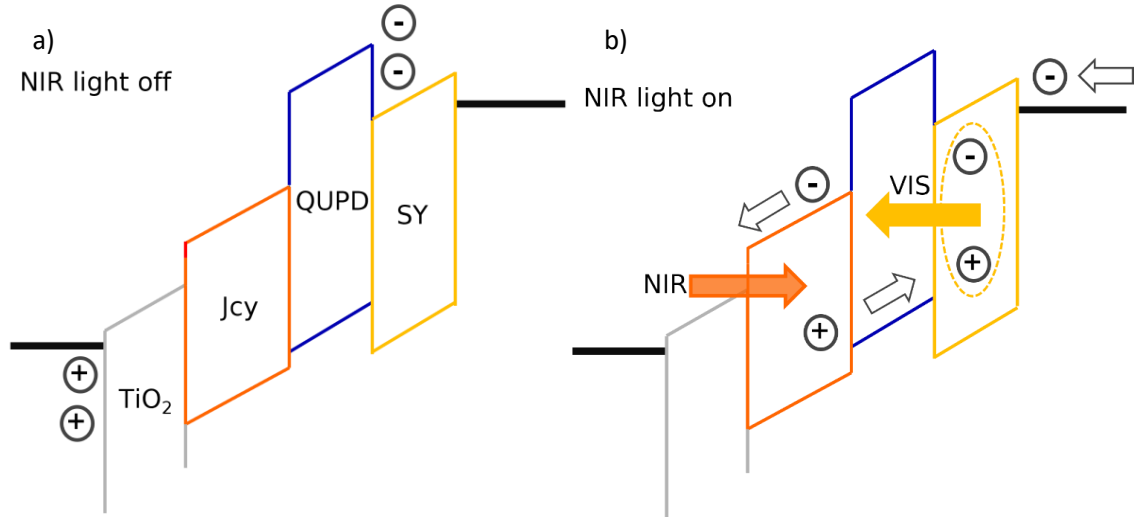
Figure 3.2 Working principle of the upconverter device. a) No NIR illumination is provided. Holes accumulate at the anode, while electrons pile up at the interface between QUPD and SY. b) NIR illumination is turned on. Electrons and holes are generated in the Jcy layer. The generated holes cross the device and radiatively recombine in the SY layer. Electrons are extracted at the anode. The device is biased in both the NIR off and the NIR on state.

3.2.2   Device working principle

NIR off-state (Figure 3.2a):

When a voltage is applied to the device, free holes accumulate in the ITO electrode, while free electrons accumulate at the interface between QUPD and SY. Since no charge carriers move across the whole device, no current can be measured. Also, both kinds of free charge carriers are spatially separated, so no radiative recombination can occur, and thus no light is emitted. In an actual device, some charge carriers can overcome the imperfect barriers and a current and luminance (referred to as dark current and dark luminance) are measured. This is seen in our devices for voltages of 8 V and beyond. We can address this issue experimentally by increasing the quality of the TiO_2 and the QUPD layer.

NIR on-state (Figure 3.2b):

When in addition to a voltage also an infrared laser (980 nm, 49 mW cm^{-2}) is used to illuminate the device, charge carriers are generated in the Jcy layer. The generated electrons drift towards the anode, where they are extracted. The generated holes drift through the QUPD layer and recombine in the SY layer with the electrons injected from the cathode, generating photons with a

wavelength of around 550 nm (yellow). The turn-on voltage required for the emission is 3.5 eV.
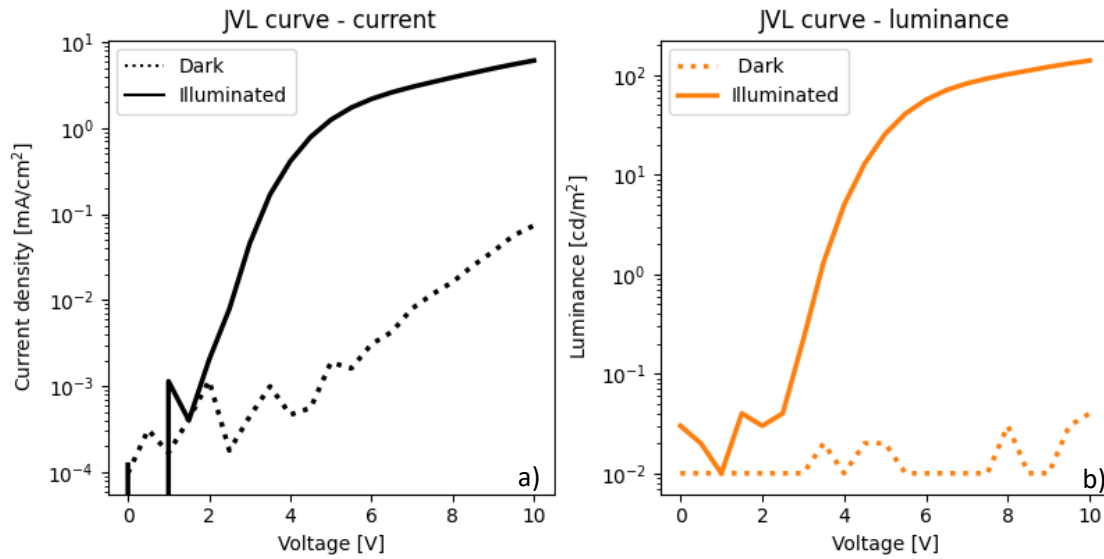
Figure 3.3 a) JV part of a JVL measurement and b) VL part of a JVL measurement in the dark (dotted line) and under illumination (solid line) of a SY-OUD.

3.2.3 JVL curve

In a current-voltage-luminance (JVL) measurement, the voltage is increased from 0 to 10 V and the current and the luminance are measured simultaneously. An example for the resulting curves is presented in Figure 3.3a) for the current density and in Figure 3.3b) for the luminance of an SY-OUD device.

For an upconverter device. the JVL curve is measured in the dark (off-state) and with an additional illumination by an infrared laser (on-state). One figure of merit measured by this experiment is the maximum on-off ratio. This on-off ratio is determined by a comparison of the luminance in the off-state and the on-state at the voltage where the difference of the luminance between on- and off-state is largest.

To measure the JVL curve, a Keithley 2400 and a Konica Minolta L/S10 luminance meter with a close-up lens 110 were used. The illumination was provided by a NIR laser (980 nm, 49 mW/cm^2, Thorlabs, CPS980)

3.2.4 Transient photocurrent response measurement

Another important figure of merit for upconverter devices is their response speed.

The speed of the device response is determined by the time it takes to generate charges after switching on illumination, the time to transport the photogenerated holes into the emission layer and the time needed to achieve a steady recombination rate in the emissive layer with the electrons injected at the cathode and transported to the recombination zone.

The response speed of a device can be measured by increasing the frequency of a modulated light pulse until the measured photocurrent has dropped to 71% of the value measured under continuous illumination (steady state). This frequency corresponds to the 3dB cut-off frequency. The cut-off frequency can also be described by the time it needs after light turn-on until the photocurrent has increased from 10% to 90%, or the time when the current after light turn-off has decreased from 90% to 10%.

The response speed of the SY-OUD was measured on the Paios system (Fluxim AG, Switzerland) using modulated rectangular pulses from a LED with a wavelength of 950 nm and a nominal light intensity of 25.4 mW/cm². The current measured at 6 V at the 3dB cut-off frequency and 100% light intensity was 0.3 mA/cm². This value was used as a target value to adjust the light intensity in the drift-diffusion simulation.
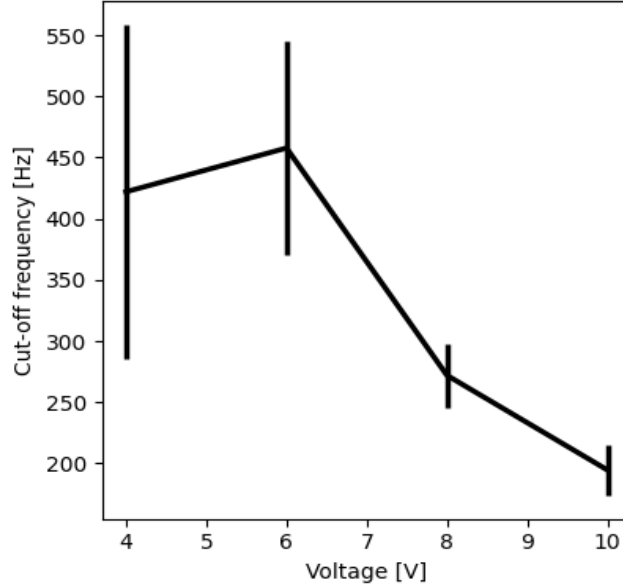
Figure 3.4 3dB cut-off frequency of SY-OUD. Here, 4 measurements were performed. The bars show the standard deviation while the line corresponds to the mean value of the measurements.

The response time of the SY-OUD in general was very slow. At 4V, a cut-off frequency of 420 Hz was measured (averaged over 4 measurements) while the cut-off frequency decreased to an average of 200 Hz at 10V (see Figure 3.4). In general, it is expected that the response speed of an upconverter device increases with voltage, since the transport of charge carriers is faster at higher electric fields. Here, we see an inverse trend. This observed unusual behaviour was further investigated using drift-diffusion simulation.

The resistance-capacitance (RC) time of our SY-OUD was measured to be around 50 ns. The RC time limited cut-off frequency for our SY-OUD was $f_{RC} = \frac{1}{2\pi RC} = 3 MHz$ [11] which was faster than the measured response speed. The device response speed therefore was not limited by the charging of the geometrical capacitance.

3.3 Simulation

We used the Setfos version 5.2 (Fluxim AG) to create a drift-diffusion model of our device.

3.3.1 Model

We combined a light absorbing and charge carrier generating layer with a light emitting layer- separated by an electron blocking layer. Hole blocking was achieved by introducing a layer between the anode and the light absorbing layer using a material with a low HOMO. The stack used corresponds to the stack displayed in Figure 3.1d and directly mimics the actual device architecture. Energy levels and mobilities were adopted or estimated from the literature, the values and corresponding sources are displayed in Table 3.1. For all layers, a density of states of 10^{21} cm⁻³ is applied.

The photoluminescence spectrum for the emission layer and the absorption spectrum for the absorbing layer can be found in the supporting information (S3.1). The injection at the electrodes is ohmic i.e it is not limiting. The illumination source chosen in the simulation is based on a 950 nm LED. Two different light intensities were applied to account for the different light sources used in the experiment. For the JVL curve, a light intensity was chosen to correspond to a peak light intensity of 49 mW/cm^2. To simulate the results from the transient photocurrent response measurement, a maximum intensity of the illumination source corresponding to 0.76 mW/cm^2 was chosen.

The goal of the simulation model was to understand the electronic processes occurring inside the device rather than achieving a good fit between experiment and simulation. We therefore used a model with only few free parameters. This has the advantage of reducing the complexity of the simulation, the risk of overfitting and the calculation time. However, using a low parameter model might lead to a less ideal quantitative agreement between experiment and simulation albeit exhibiting the features also observed in experiment.

Simplifications introduced in the simulation are

- Constant mobilities in all layers
- No trapping
- Direct generation of charge carriers i.e no exciton dynamics
- Constant generation efficiency of charge carriers independent of applied voltage

Table 3.1 Most relevant parameters for the simulation. The LUMO of Jcy is estimated by adding the optical band gap to the HOMO.

Electrodes		Jcy continued	
Workfunction ITO [eV]	4.7 [143]	HOMO [eV]	5.37 [144]
Workfunction Ca [eV]	3.3	LUMO [eV]	4.1
Injection barrier anode [eV]	3.4	QUPD	
Injection barrier cathode [eV]	0.3	Rel permittivity [1]	4
TiO$_2$		Hole mobility [cm^2/Vs]	4e-6 [145]
Rel permittivity [1]	100 [7]	Electron mobility [cm^2/Vs]	4e-6
Hole mobility [cm^2/Vs]	1e-8	HOMO [eV]	5.1 [146]
Electron mobility [cm^2/Vs]	0.01 [147]	LUMO [eV]	2 [146]
HOMO [eV]	8.1 [143]	SY	
LUMO [eV]	4.4 [143]	Rel permittivity [1]	3
Jcy		Hole mobility [cm^2/Vs]	3e-6 [148]
Rel permittivity [1]	4	Electron mobility [cm^2/Vs]	6e-7
Hole mobility [cm^2/Vs]	1e-6 [149]	HOMO [eV]	5.4 [150]
Electron mobility [cm^2/Vs]	1e-6 [149]	LUMO [eV]	3 [150]

3.3.2   Simulation of transient photocurrent response measurement

Instead of simulating a periodically changing illumination pattern and adjusting the frequency to achieve the measured current at 3 dB, we used a transient model. In a transient simulation, the response of a device to a change of a parameter is simulated as a function of time. The transient simulation usually starts from a previously calculated steady state. At some point in time a parameter is changed. We simulated the device behaviour in a range of 0.1 µs to 10 s with 50 steps for each decade. The steady state used as a starting point for the transient simulation is calculated in the dark at a constant voltage (6 V unless other specified) and at t = 5 us an illumination source is activated. At the end of the transient simulation, a new steady state is reached. We adjusted the illumination intensity in such a way that the current density in the new steady state at 6 V

corresponded to 0.3 mA/cm^2. This is the current density at 3dB frequency measured in the transient photocurrent response measurement. To be able to compare the frequency from the transient photocurrent response measurement with the time to reach steady state in the transient simulation, the time constant was calculated as the inverse of the frequency.

3.4   Results
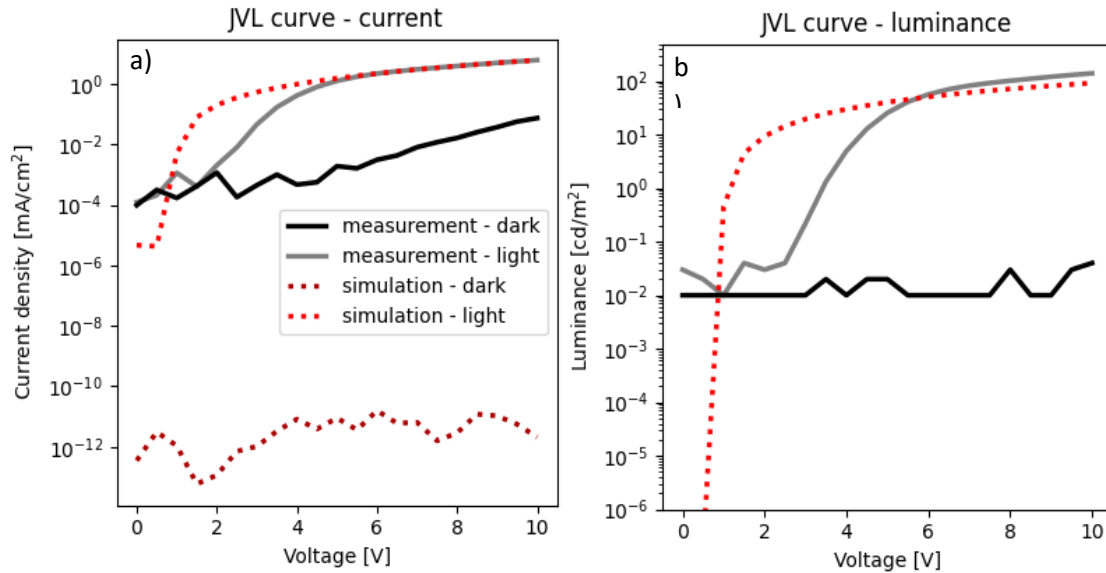
Figure 3.5 a) Current from a JVL measurement and corresponding simulation. b) luminance from a JVL measurement and corresponding simulation. Dark colours (dark red, black) correspond to measurement and simulation under no illumination condition, while red and grey corresponds to illumination condition. Red colour tints and dotted lines are used for simulation, while black and grey solid lines are used for the measured data. In b) the simulated luminance in the dark is zero and therefore not displayed on the log scale.

3.4.1   Dark case

(see Figure 3.5a and b, dark red and black lines)

In the case where no illumination is applied, a dark current is measured which increases with voltage from 9.72×10^{-5} mA/cm^2 to a value of 0.07 mA/cm^2 at 10 V. This corresponds to an increase by a factor of 756. This increase in dark current is attributed to free electrons crossing the device due to an imperfect barrier at the QUPD-SY interface. This is further supported by the low measured dark luminance (signal at detection limit). For dark luminance to occur, free electrons and holes are required. The absence of luminance and the presence of current under dark conditions suggests only one kind of free charge carrier exists within the device. The type of charge carrier present in the device was determined by changing the quality of the TiO$_2$ layer. When TiO$_2$ was deposited by a sol-gel process, a less dense layer was achieved than by using atomic layer deposition. It is therefore likely that pin holes exist within the TiO$_2$ layer which facilitates injection of free holes into the device. Indeed, we measured an 8-fold increase in dark current for devices with sol-gel deposited TiO$_2$. Also, a dark luminance of 0.3 cd/m^2 was measured at 10V (30 fold increase)[142]. We therefore conclude that the charge carriers present in a device with a TiO$_2$ layer deposited by atomic layer deposition are electrons.

The calculated current from the simulation is up to 10 orders of magnitude smaller than the measured current (Figure 3.5). This difference arises since we cannot simulate an imperfect barrier like pinholes or tunnelling pathways within our model. The barrier at the TiO$_2$ is 3.4 V which is high

enough to completely suppress hole current. Therefore, the current in the simulation only corresponds to the low number of electrons which can thermodynamically cross the barrier of 1 eV between SY and QUPD. Since there are virtually no holes present in the simulation, the generated luminance is also zero. The zero line for the onset of luminance is chosen to be 10^{-6} cd/m^2 which corresponds to the lower end of the human scotopic vision range [151]. Below that luminance, a human will likely not perceive any light.

3.4.2 Illuminated case

(See Figure 3.5a and b, bright red and grey lines)

The current in the measurement starts to rise around 1.5 V, which corresponds to the expected work function difference between both electrodes. In the simulation, the current onset is already at 0.7 V (baseline of onset chosen to be 10^{-4} mA/cm^2). At this voltage, the charge carriers generated in the Jcy layer are separated and the free holes have enough energy to overcome the low hole barrier (0.3 eV) between QUPD and SY. The electron density in the SY layer at 0.5 V is very low. The holes therefore recombine at the cathode which is recorded as current. At low voltages, the simulated current is up to 2 orders of magnitude larger than the current measured in the experiment. The difference can be attributed to trap states which are present in the device but not considered in the simulation.

Below 2.5V, a very low luminance can be observed due to charge carriers absorbing NIR photons and thus gaining enough energy to radiatively recombine in the SY layer. However, the significant luminance onset in the experiment is around 2.5 V, which corresponds to the energy gap between the HOMO and LUMO of the SY light emitting layer. Only at around 6 V the luminance levels with the simulated luminance. Below that voltage, there are two processes diminishing the luminance output. On one hand there is the lower efficiency in separating the excitons generated in the Jcy layer which leads to fewer free holes which can cross the device and radiatively recombine in the SY layer. On the other hand, there are trap states present within the device. Trap states enable an additional recombination pathway which competes with radiative recombination especially at low voltages. The measured luminance therefore is decreased. At high voltages where the free charge carrier densities are large, the relative impact of the trap-assisted recombination compared to the radiative recombination is smaller which leads to a large luminance. Both mentioned processes are not considered in the simulation. Therefore, the simulated luminance is higher at low voltages compared to the measurement. Also, the onset of the simulated luminance is around 0.7 V which corresponds to the band gap of the Jcy dye. This early onset arises due to the simple coupling model between absorption and emission. There, only the number of particles is strictly conserved, while the energy is not considered explicitly. This means if free charge carriers are present in the SY layer, they will recombine and emit photons according to the photoluminescence spectrum of the layer – without checking the energy state of the charge carriers. Also not considered in the simulation is the increase in emission efficiency at large voltages which leads to a slight underestimation of the luminance in the simulation. The maximum on/off ratio is measured at 9 V with a value of 12'120. Though mind that this ratio also depends on the detection limit for emitted photons of the detector. The dark luminance in the simulation is too low to allow a sensible determination of the on/off ratio.

At high voltages, the current increase slows down and eventually levels off. At which current and voltage this leveling off occurs depends on the chosen illumination intensity (S3). This indicates that at high voltages the device efficiency is limited by the number of photogenerated holes while at low voltages device performance is limited by another process.

3.4.3   Transient simulation
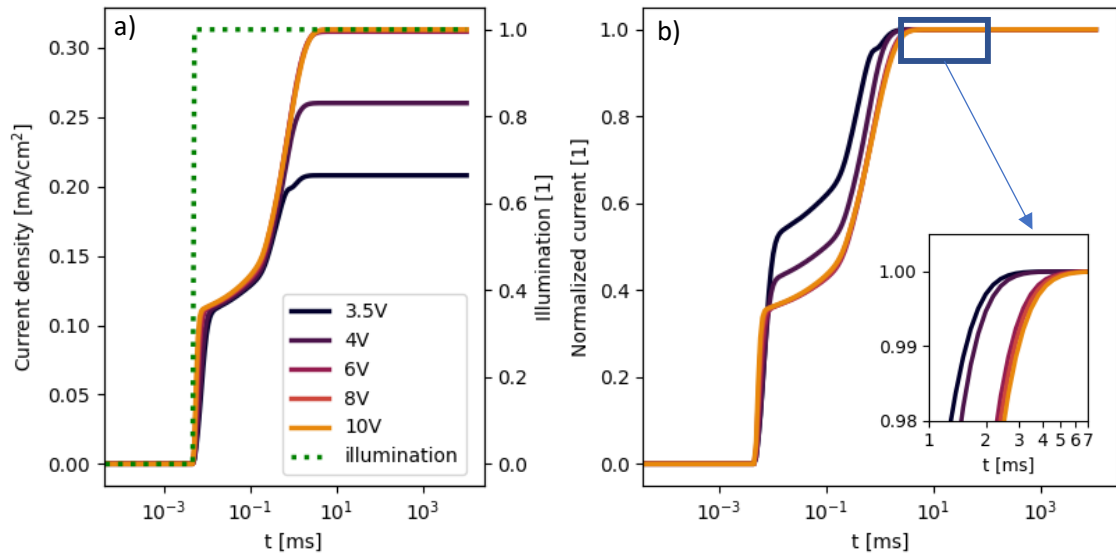
Figure 3.6 a): The development of the current density after the device is illuminated. Onset of illumination is at t=5 us. The illumination profile is marked with a green dotted line. b) normalized current during turn-on with zoom to the region around 1 to 7 ms. The blue rectangle marks the region which is magnified in the inset. To not obscure interesting features, the rectangle is larger than the zoomed in region. The light intensity for all simulations is 0.76 mW/cm² corresponding to 100% light intensity.

Displayed in Figure 3.6a is the illumination turn-on simulation for different applied voltages. When illumination is turned on (marked by the green dotted line), the current starts to increase in two to three (at 3.5 V only) distinct steps. The steady state current – the current at the end of the transient simulation – increases with increasing voltage up to a value of 0.31 mA/cm² at a voltage of 6 V and thereafter reaches a plateau. Increasing the voltage further does not further increase the current. This contrasts with the speed experiment, where the current continues to increase with voltage and reaches 2.08 mA/cm² at 10 V. However, at 4 V the current reaches 0.14 mA/cm² in the experiment while it plateaus at 0.2 mA/cm² in the simulation. The data from the experiment is provided in S3.6. The reason for the difference in current density between the experiment and the simulation is attributed to the increase in efficiency of the charge generation in the Jcy layer with increasing voltage. For the simulation, a charge generation efficiency of 100% is assumed. For this reason, the current density at 6 V at the end of the transient simulation corresponds to the maximum photocurrent density which can be achieved at an illumination 0.76 mW/cm². The maximum photocurrent density only depends on the illumination intensity and not on the applied voltage, leading to the plateau at and above 6 V seen in the simulation. At 4 V, the generation efficiency of charge carriers in Jcy is lower than at 6 V, reducing the current density in the experiment further than the current density in the simulation.

During the first sharp current increase, the device with the highest applied voltage is fastest. The speed goes down for decreasing voltage. To see whether this trend is also visible in the second increase, a normalization was applied on the data (Figure 3.6 b). To allow better visibility, the relevant section is magnified in the inset of Figure 3.6b. In the second current rise, we can see the opposite trend from the first current rise. For increasing voltage, the time for the current rise increases. Since this is the last current increase step before the device reaches steady state, this is also the step determining the overall time to reach steady state. The device therefore slows down with increasing voltage. This trend is also observed in the transient photocurrent experiment (see Figure 3.8c).

The first current increase is governed by the generation and separation of charge carriers in the Jcy layer. A factor reducing the current is the displacement current due to a change in electric field caused by the newly present charge carriers. The separation of the photogenerated charge carriers is faster at higher voltages which is reflected by the faster speed of the current increase. The second sharp current increase is governed by the transport of photogenerated charge carriers through the device and the change in recombination rate in the recombination zone. The reason for the speed trend will be elaborated in the discussion section.
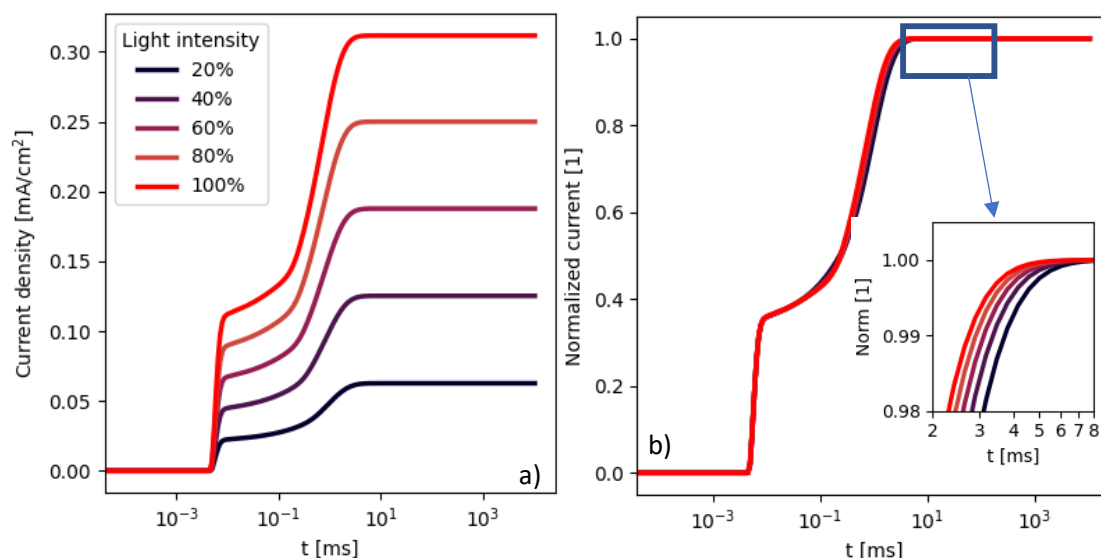
Figure 3.7 a) development of the current density at turn on for different light intensities. b) normalized current density during turn on. Inset: zoom to the region denoted by the blue rectangle. The voltage is 6 V for all simulations.

Displayed in Figure 3.7a is the transient current simulation for different light intensities at 6 V. To better evaluate the time needed to reach steady state, a normalization was performed, displayed in Figure 3.7b. The relevant portion of the curve is shown in the inset. As for the case with different voltages, we see two distinct times with sharp increase in current density. The first increase in current density is independent of the chosen illumination intensity albeit showing different current densities. This further confirms that the initial rise is due to the generation of charge carriers. The number of generated charge carriers differs for the different light intensities leading to different current densities. However, the separation of charge carriers is equally fast for all cases since the same voltage is applied. The speed therefore is the same for all light intensities. The second increase in current exhibits different speeds depending on the illumination intensity. The higher the intensity, the faster the device reaches a steady state. The same trend is also seen in the experiment.

In the transient photocurrent experiment on SY-OUD only a one-step increase in current was observed (one period of the experiment is displayed in Figure 3.8a). However, this is attributed to the low time resolution of the experiment; the experimental time resolution was 0.3 ms while the initial current density rise in the simulation has a duration of 3 µs. The same experiment on an OUD with a different emitter (iridium-based host-guest system) recorded at higher time resolution exhibits two distinct increases in current (Figure 3.8b), as observed in the simulation. It stands to reason that a device based on SY, which has a lower response speed than a device using an iridium emitter, would exhibit the same two-stage current density increase when measured with a sufficiently high time resolution. The current increase and the time to steady state exhibited by both the SY and the iridium-based OUD follow the trends observed in the simulation.
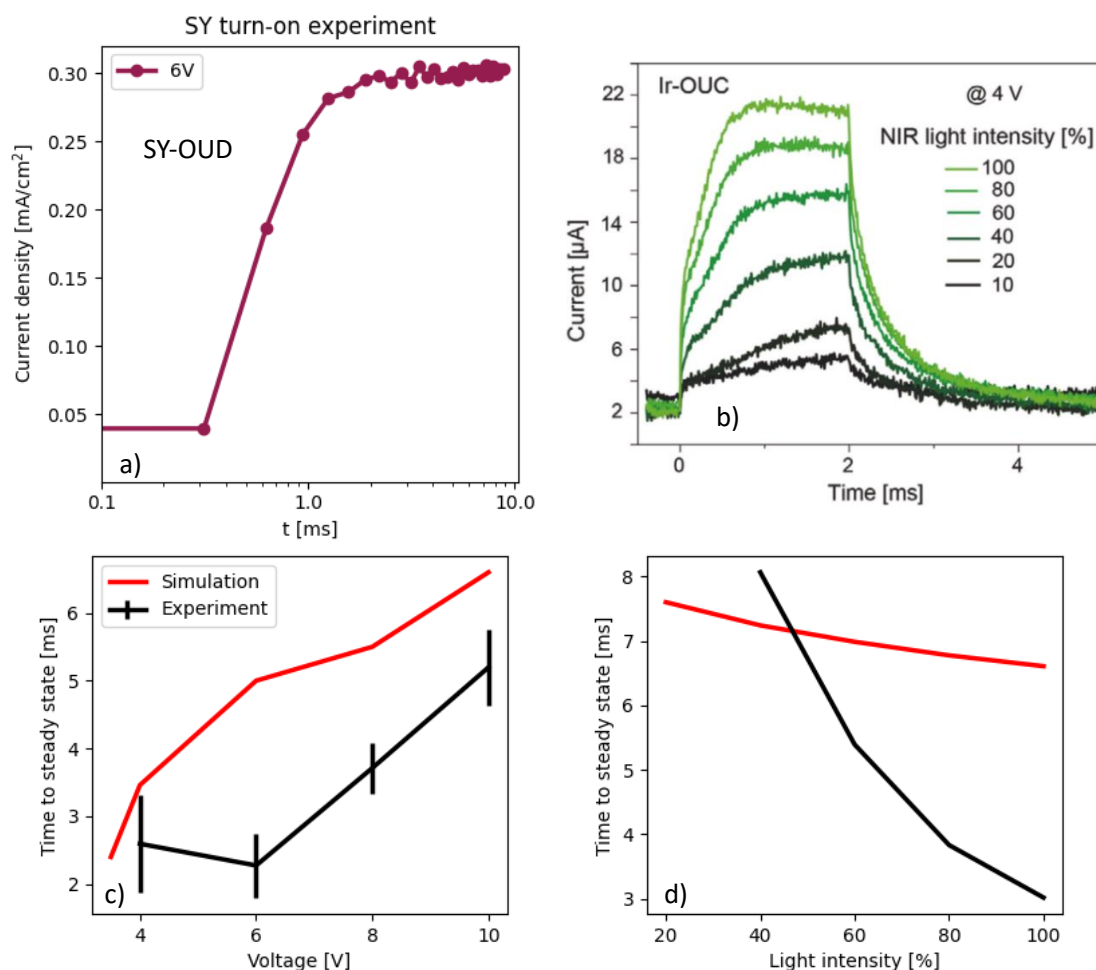
Figure 3.8 a) zoom in to one period of the transient photocurrent experiment at 6 V. b) one period of a photocurrent transient experiment on a device with an iridium host-guest emitter at different light intensities with high resolution in time. A fast and a delayed increase in current is observed. c),d) The time needed to reach steady state for experiment (black, variation denoted with bars) and simulation (red line) for different voltage (c) and different light intensity (d).

The times to reach steady state for the experiment and the simulation have been extracted and are plotted in Figure 3.8c as function of the applied voltage, and in Figure 3.8d as function of the light intensity. For both the experiment and the simulation, the time to steady state increases with increasing voltage. Also, the times are similar between the experiment and the simulation. However, at 6 V in the experiment, the device reaches steady state fastest, faster than at lower voltages. This is not reflected by the simulation. There are error bars added in the extracted times for the experiment to denote the spread of measured time to steady state. The increase in time to steady state is larger than the spread in the measurement.

The decrease of time to steady state for increasing illumination intensities is much more pronounced in the experiment than seen in the simulation (Figure 3.8d). This could originate from the low light intensity used in the simulation (25.4 mW/cm^2 vs 0.76 mW/cm^2).
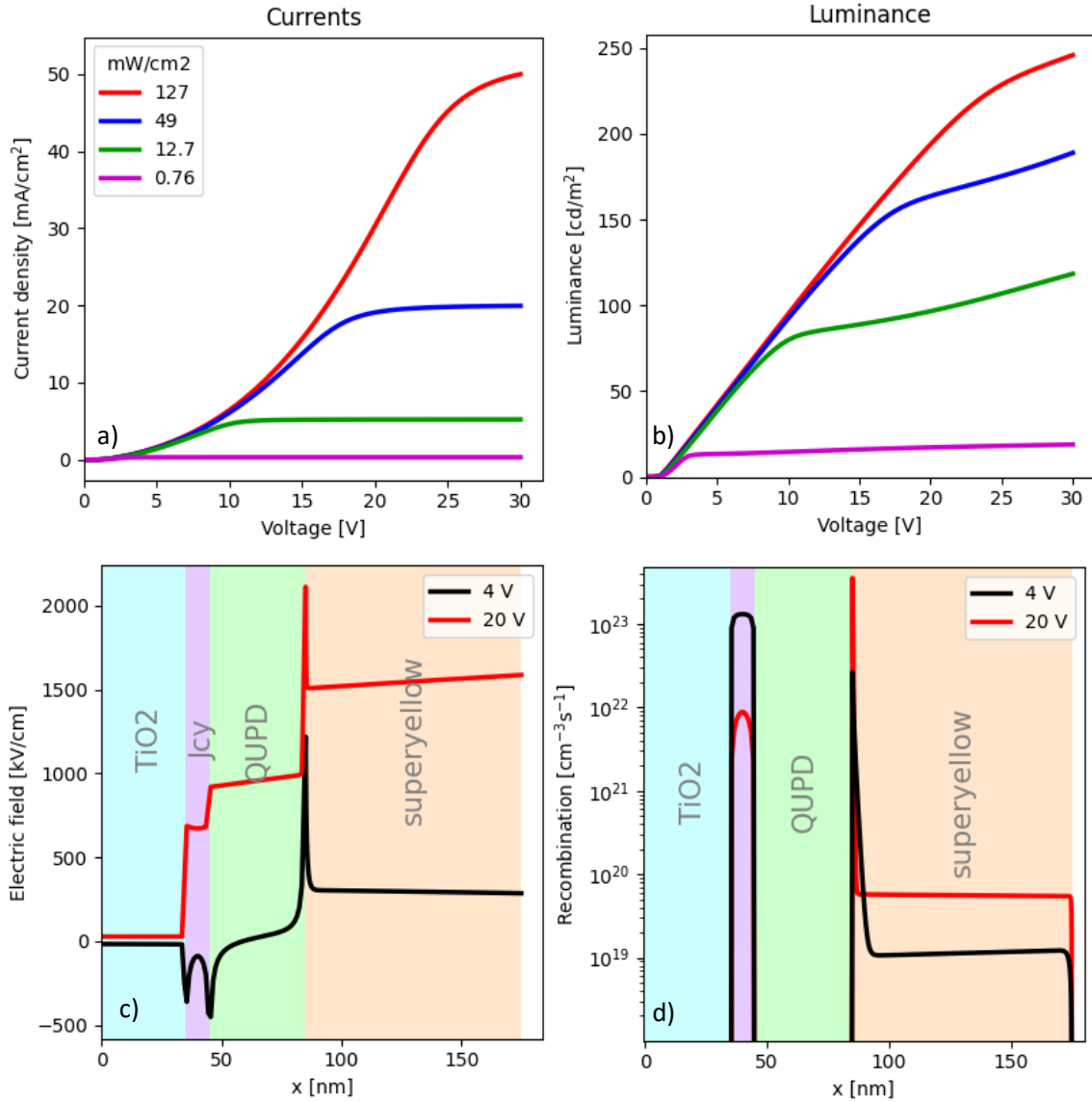
Figure 3.9 a) JV curve at different illumination intensities. b) LV curve at different illumination intensities. The blue line corresponds to the illumination intensity used in the JVL curve in the main text. c) electric field for 49 mW/cm² illumination at 4 V and 20 V. d) Recombination rate for 49 mW/cm² illumination at 4 V and 20 V. At each displayed voltage, the electric field and the recombination rate are at thermodynamic equilibrium.

3.4.4 Current density limit

There are two main contributors limiting the current density in an upconverter device. One factor is the generation of photocurrents. Only a limited number of charge carriers can be generated upon illumination of a photodetector with light. This limit is governed by the absorption capabilities of the photodetector, its charge generation and separation efficiency and parasitic absorption of incident photons in other layers.

The limit posed by photogeneration of charge carriers is visible at high voltages, where a plateau is reached. At which voltage a plateau is reached depends on the applied illumination intensity. In Figure 3.9a, JV curves at different illumination intensities are displayed. At a low illumination intensity of 0.76 mW/cm² as used for transient simulations, the plateau is reached at 4.5 V at 0.3 mA/cm². For the illumination intensity of 49 mW/cm² as used in the JVL experiment, a plateau in the simulation is reached around 30 V at a value of 19.95 mA/cm². This high required voltage explains why no plateau was seen in the experiment where measurements were only possible up to

10 V. In the simulation, the photocurrent generation is independent of the voltage since no exciton dynamics is included and thus the photocurrent is constant (S3.3).The plateaus reached in Figure 3.9a correspond well to the photocurrent limit simulated in S3.3. This shows that the plateau is indeed due to limited photocurrent generation.

The second factor limiting the current density is parasitic recombination. With the term parasitic recombination, we refer to all recombination processes which occur besides the radiative recombination in the SY layer. In the experiment this means non-radiative recombination in all layers as well as trap assisted recombination and quenching at electrodes and the QUPD-SY interface. In the simulation, quenching and trap assisted recombination are omitted.

At low voltages, the electric field in Jcy is low and charge carrier separation therefore is inefficient. More so, the presence of a high number of generated charge carriers completely screens the applied field in the Jcy layer. Therefore, the only driving force affecting the charge carriers in this layer is diffusion. Since there are no holes present in the TiO_2 layer and no electrons present in the QUPD layer (seeS3.4), the holes diffuse towards the anode while the electrons diffuse towards the cathode. This is the opposite direction than would be observed for drift. The electric field generated by those free charge carriers therefore is negative which can be seen in (Figure 3.9c) The low charge carrier separation limits the simulated current at 49 mW/cm^2 illumination to 0.97 mA/cm^2 at 4 V and to 19.08 mA/cm^2 at 20 V. The increase of voltage Figure 3.9c) and thus reduce the number of free charge carriers still present. Therefore, the recombination probability of the newly generated charge carriers in Jcy decreases (Figure 3.9d) and more holes reach the emissive SY layer where they recombine with electrons injected from the cathode. This leads to an increase in luminance also at high voltages where the current already is constant.

3.5   Discussion

It commonly is expected that the speed of an OUD increases with voltage, since the voltage leads to a higher drift velocity and consequently increases transport of charge carriers across the device. However, in OUD based on superyellow we observe the inverse trend. The reason for this inversion is an interesting interplay between transport of holes through the QUPD layer and the transport of electrons through the superyellow layer.

At the start of the transient photocurrent experiment, only a voltage is applied, and the device is in equilibrium. Electrons are present mainly in the superyellow layer where they pile up at the QUPD superyellow interface (Figure 3.10a) and in TiO_2. The higher the voltage, the more electrons are present at the interface while the electron number in TiO_2 decreases. At this time, the device is completely free of holes (Figure 3.10c). The threshold density for having a single charge carrier somewhere inside our device is about 2*10^{6}cm^{-3} according to $\frac{1}{Device\ volume} = \frac{1}{175nm*3.14mm^2}$. This distribution of charge carriers inside the device leads to a high electric field inside Jcy and QUPD where only little charge carrier can screen the externally applied field. In TiO_2 and superyellow, many electrons are present and thus the electric field is shielded (Figure 3.10e). Notably, the electric field is the same in superyellow for all applied voltages.

When the device is illuminated and is in thermodynamic equilibrium (at the end of the transient simulation), the number and distribution of charge carriers drastically changes. There are more electrons present throughout the superyellow layer (Figure 3.10b) and the zone where electrons pile up narrows down to 5 nm in width. Especially in the Jcy layer electrons are present since they are generated in this layer. The higher the voltage is, the less electrons are present in Jcy, improving

charge carrier separation and the narrower the pile up zone gets. Under illumination, a significant number of holes is present in the device, mainly concentrated in the Jcy layer and at the interface between QUPD and superyellow (Figure 3.10d). The holes pile up at the QUPD and superyellow interface because a barrier of 0.3 eV is present between both layers. With increasing voltage, the number of holes in the device decreases since the holes are driven towards the recombination site by a higher electric field (Figure 3.10f). The number of holes in QUPD also determines the shielding of the external field. The more holes are present, the larger the screening gets and consequently, the driving force for the hole drift diminishes.

With the initial and the end state of charge carrier distribution and electric field, we have the means to understand what happens during the illumination turn on simulation at the different voltages.

We see that at high voltages, the transport of holes through the QUPD layer is indeed faster than at lower voltages. At 10 V the speed of holes and electrons in QUPD corresponds to 6.9 cm/s in the dark and 4.7 cm/s under illumination. For 4 V, the speed is 2 cm/s in the dark and on average 0.16 cm/s under illumination. The transient current up to the second sharp increase therefore is increasing faster at high voltage. However, in the emissive layer, the electron transport is slow due to low electron mobility and low electric field in this layer. At x=110 nm in the device in the dark, the speed of the electrons is 0.01 cm/s regardless of applied voltage. Though mind that closer to the interface the speed increases while closer to the electrode the speed of the electrons diminishes. The electric field across the device is shielded in superyellow. This means that at the time the illumination is turned on, the speed of the electron in the SY layer is the same irrespective of the applied voltage. At high voltages, fast photogenerated holes arrive at the recombination site at the interface of QUPD and SY and recombine with the electrons there. The recombination process at the interface and the hole transport across QUPD is much faster than the transport of electrons to the recombination site. The transport of holes across the 40 nm QUPD layer takes 0.58 µs at 10V and 0.85 µs at 4 V while the transport of electrons through the superyellow layer takes with 0.88 ms, around 1000 times longer. Therefore, a slight overshoot in recombination occurs (i.e higher recombination rate than at steady state) removing more electrons from the recombination site than would be present in the steady state since not enough electrons are transported within the time it takes for the recombination to take place. This slight electron deficiency in turn lessens the shielding of the electric field in the SY layer and thus the speed of the electrons increases and the electrons at the recombination site are eventually replenished. This initial overshoot in recombination is lower for lower voltages, which means less electrons must be transported across the SY layer and thus steady state is reached faster at low voltages. In this whole process, the electron transport is the limiting factor.
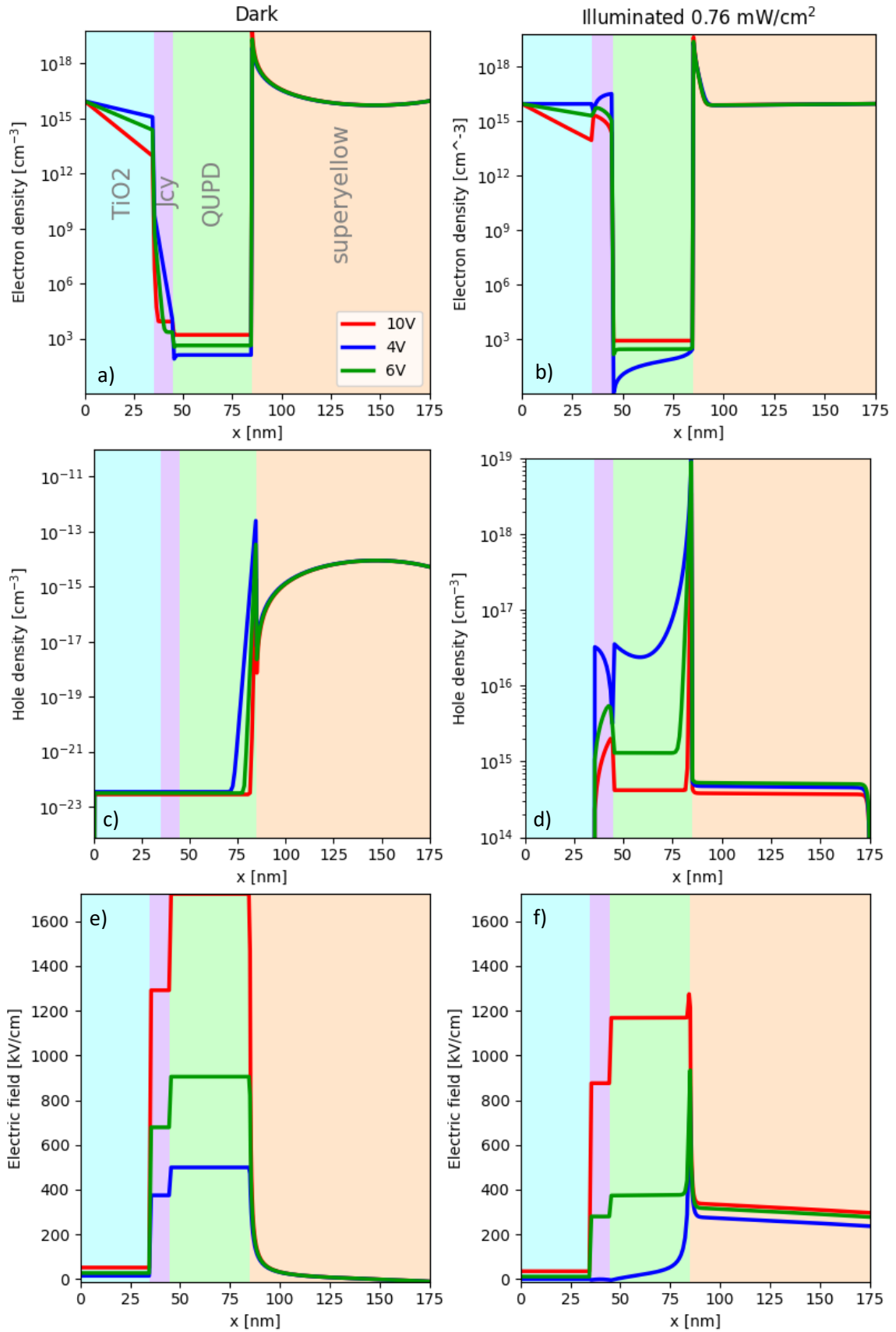
Figure 3.10 a),c), e) electron density, hole density and electric field, respectively at dark conditions and applied voltage b), d),f) electron density, hole density and electric field under illumination at 0.76 mW/cm², respectively. The device is at equilibrium both in dark and under illumination condition. Different voltages are used and denoted in blue for 4V, green for 6V and red for 10V.

This overshoot in the transient simulation can be observed when the illumination intensity is increased. In such a case, more holes are transported to the interface and recombine with the electrons present there than in a case with less illumination. This means more electrons must be replenished and the effects are more easily visible (S3.7).
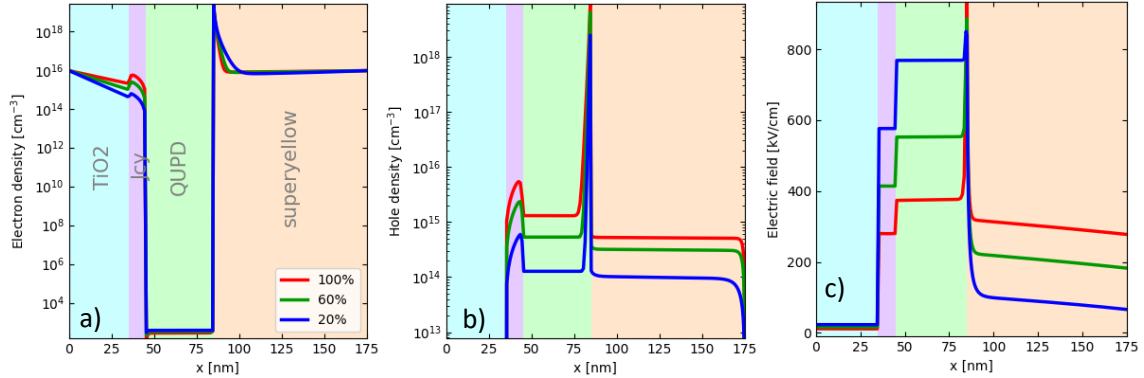

Figure 3.11 a) electric field b) hole density and c) electric field for 20% (blue), 60% (green) and 100% (red) illumination intensity. 100% illumination intensity corresponds to 0.76 mW/cm². The applied voltage is 6 V.

A similar chain of arguments can be used to explain the trend of speeding up of the device with increasing illumination intensity (Figure 3.11). At high illumination intensities, the number of generated charge carriers in the Jcy layer is higher than at lower illumination intensities. This is the case for electrons as well as holes. However, since the photogenerated electrons are extracted at the anode, the number of electrons in the QUPD layer stays low. The number of holes in QUPD is increasing substantially as part of the transport pathway. This increase in hole density in turn reduces the electric field in the QUPD and more of the applied potential decays across the SY layer. This leads to a higher speed of electrons and thus a lower transport time. The speed of the device thus increases with increasing illumination intensity.

A very interesting fact to observe is the location and the size of the recombination zone. The simulation revealed that a significant portion of the radiative recombination takes place within 5 nm of the implications for the device. It is known that emissive layer at the interface between QUPD and SY (Figure 3.9d). This has important electron-polaron quenching can occur at the interface between QUPD and SY since the electron density is very large [152]. This leads to poor efficiency of the device since a large portion of the photogenerated holes do not recombine radiatively. First preliminary tests show that the introduction of an additional hole transporting layer between QUPD and superyellow indeed lead to a higher luminance output [142]. Also, the transport of holes through QUPD could lead to oxidation of a fraction of QUPD. Oxidized QUPD can absorb light of wavelengths between 400–580 nm[153] and therefore is able to quench light emitted from superyellow (550nm). This in turn is one mechanism that can diminish the luminance output of the device at long run times as more oxidised QUPD is generated [142].

An important speed limiting factor in the SY-OUD is slow transport of the electrons across the superyellow layer. One possibility to reduce transport time and with it increase the device speed might be the decrease of the superyellow layer thickness and thus the reduction of the distance travelled by the electrons. In Figure 3.12a, the simulation of two devices, one with 45nm and one with 90nm thick superyellow layers is displayed. Indeed, the device with the thinner SY layer is faster (inlet). However, the optical properties of the device changes upon changing the thickness of SY leading to a lower charge carrier generation in the Jcy layer and thus a lower current in the device, but also to an increased outcoupling of luminance (Figure 3.12b).
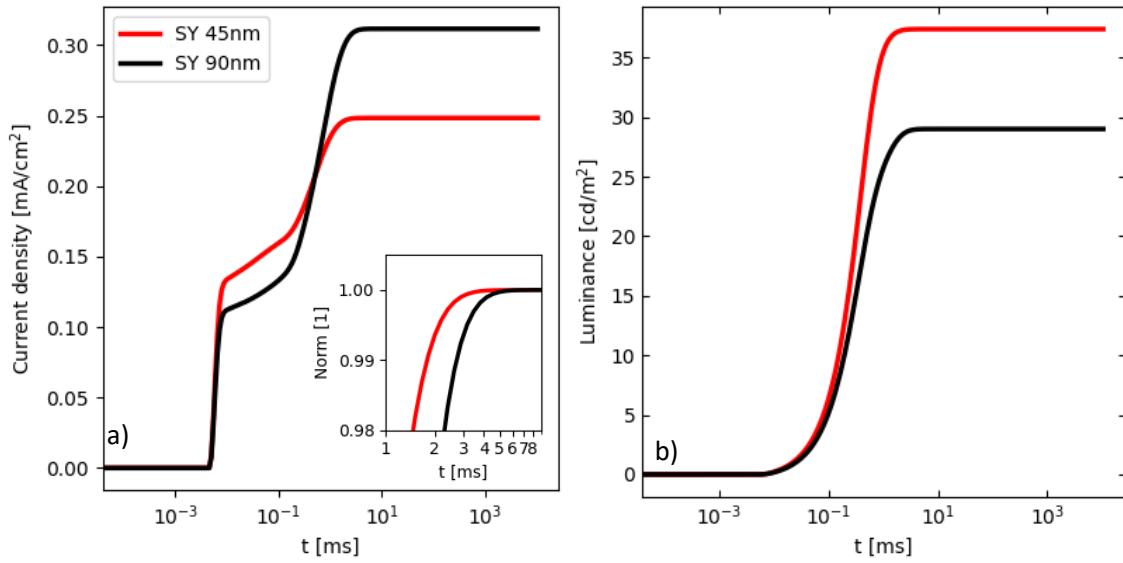
Figure 3.12 a) current transient for a normal SY layer (90nm, black line) and a thin SY layer (45nm, red line). inlet: zoom at the interesting time shortly before steady state for a current normalized transient. b) luminance transient for the same two SY thicknesses as in a)

An important parameter by which the experimental response speed can be increased is the electron mobility in the emission layer. Simulations with an electron mobility in the SY layer of $2*10^{-5}$ cm^2/Vs already reach steady state at 0.3 ms. This is a 20-fold improvement over the time needed with $6*10^{-7}$ cm^2/Vs (Figure 3.13b). For the high electron mobility case, the speed of the electrons at the start of the simulation at 110 nm is 0.34 cm/s and 26 us transport time which corresponds to a 30-fold increase in speed and 30-fold decrease in transport time as compared to the low electron mobility case. This is sufficient to prevent the recombination overshoot. Therefore, the speed increases with increasing voltage, as one would commonly assume (Figure 3.13a and inlet).
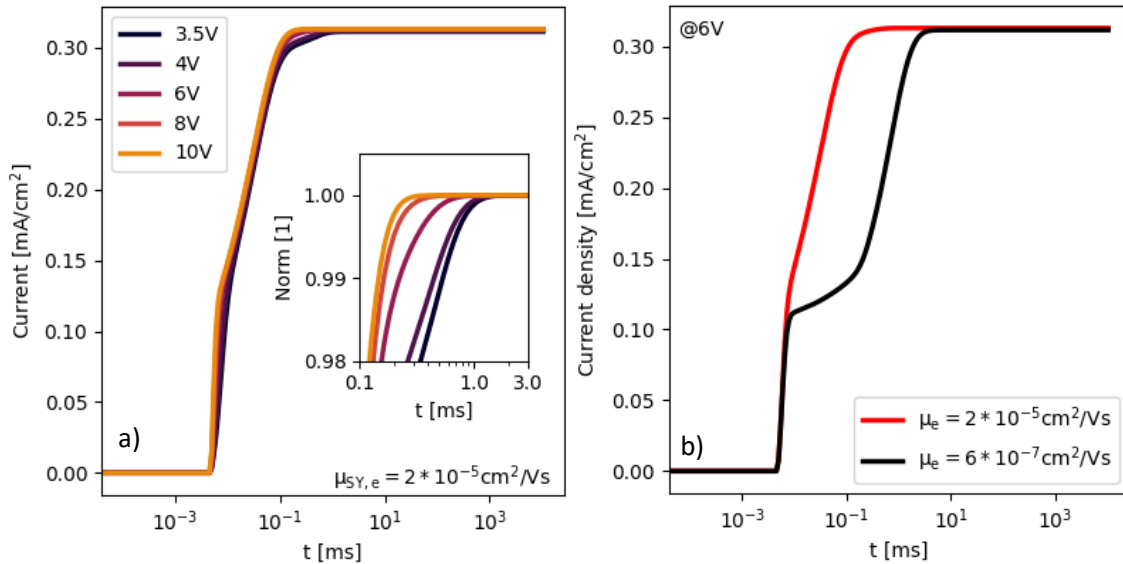
Figure 3.13 a) turn-on simulation with an electron mobility of $2*10^{-5}$ cm^2/Vs in the SY layer. The crucial part of the curve is magnified in the inset. In b) the turn on behaviour of two devices with high and low mobility is displayed.

99

3.6   Conclusion

We successfully generated a simple drift-diffusion model of an organic upconversion device by combining an NIR photon absorbing and charge generation layer with an emissive layer (550 nm wavelength) and appropriate barriers to ensure the functionality of the simulated device. With the help of drift-diffusion simulation, we were able to explain the counter-intuitive behaviour of decreasing speed with increasing voltage. We identified the electron mobility in the emitter layer as the parameter mainly responsible for this peculiar device behaviour. Also, we can suggest helpful improvements for the fabrication of upconverter devices by avoiding tedious parameter changes in the lab. The most important suggestion for improving the speed of the device is finding a way to increase the electron mobility in the emitter. This could lead to an increase in speed response up to 20 times. Another suggestion is to include a separation layer between the QUPD and the emissive layer in order to improve device lifetime. Simulations also suggest that the reduction of the emitter thickness can have beneficial effects ranging from improved luminance and faster speed to lower fabrication costs since material is saved.

3.7 Supporting information

3.7.1 Absorption and emission
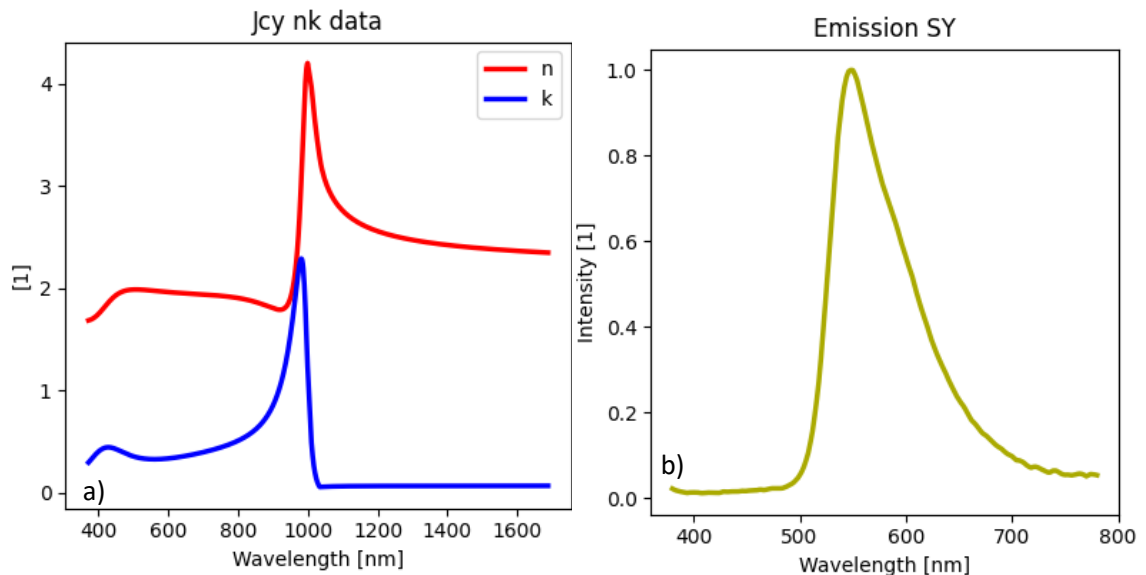
S3.1 a) Extinction coefficient (k) and refractive index (n) used for the Jcy layer[138]. b) photoluminescence data for the SY emission layer [144].

S3.1 emission and absorption spectra used for the simulation of the upconverter device. Note that the Jcy layer is only weakly absorbing in the wavelength range where super yellow is emitting.

3.7.2 Current at 6V for dark and illuminated conditions (high illumination case)
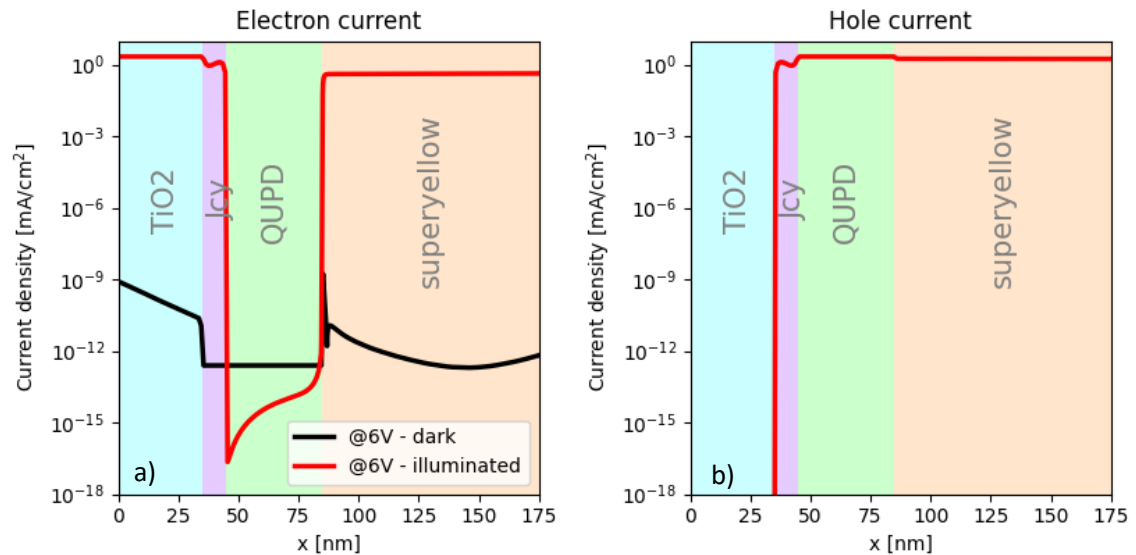
S3.2 a) electron current at 6 V for dark (black line) and illuminated (red line) condition. b) hole current at 6 V illuminated (red line) condition. There is no hole current present in dark conditions. The illumination for this simulation is 49 mW/cm²

The total current of a device consists of the sum of the electron and the hole current. In an experiment, it usually is not possible to ascribe the measured current to one or the other charge carrier type. Simulation therefore is a valuable tool to investigate the contribution of electron and hole movement to the total current.

Electron and hole current at 6 V – the current arising due to the drift of electrons or holes, respectively - are displayed in S2. In the dark, only electrons which overcome a barrier of 1eV contribute to the electron current. At room temperature the probability of overcoming this barrier is low which leads to the low electron current of around $1*10^{-12}$ mA/cm^2 and less (S3.2a). The barrier for holes is with 3.4 eV even larger. This is reflected by a non-existent hole current in the dark (S3.2b). The low overall current observed in the device is therefore only due to electrons. When illumination is turned on, electron and hole currents up to 2.2 mA/cm^2 are seen in certain areas of the device. The hole current in the TiO$_2$ layer is negligibly small, since no injection takes place at the anode (barrier of 3.4 eV) and the holes generated in the Jcy only drift towards the cathode. Since holes are generated at a constant rate, a nearly constant hole current is generated. In the Jcy layer, also electrons are generated which are driven towards the anode. Therefore, the electron current in the TiO$_2$ layer is large. In addition, electrons are injected at the cathode and cross the superyellow layer. There is a large electron barrier of 1eV between QUPD and SY layer, therefore only few electrons can enter the QUPD layer, leading to a small current of less than $1*10^{-12}$ mA/cm^2 in this layer. The barriers for electrons and holes for injection into the SY layer are low. Therefore, the current in this layer is composed of contributions from holes and electrons. The hole current in the SY layer is 5 times as high as the electron current since the holes are 5 times as mobile as the electrons.

3.7.3   Photocurrent limit
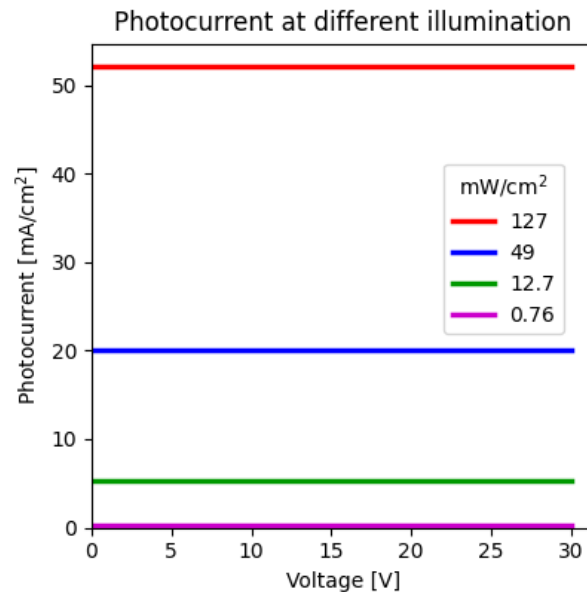
S3.3 Photocurrent generation at different illumination intensities. The blue line corresponds to the illumination used for experiment.

The generated photocurrent for different light intensities if the generation efficiency is 100%. Since we did not consider an increase in generation efficiency with increasing voltage, the photogenerated current is constant.

3.7.4 Diffusion of charge carriers
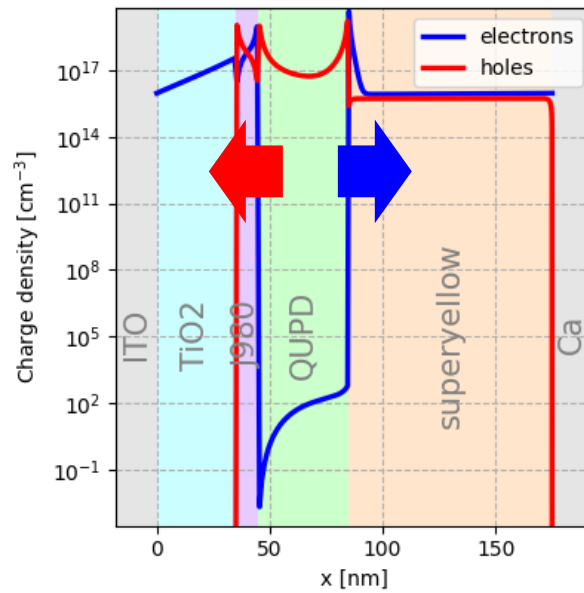
S3.4 Free charge carrier distribution at illumination with 49 mW/cm² intensity at 950 nm wavelength and an applied voltage of 4V. The preferred direction of diffusion is marked with a blue arrow for electrons and a red arrow for holes. Blue is also used for the charge carrier distribution of electrons, while red denotes the distribution of holes.

Distribution and density of electrons and holes in a SY-OUD at high illumination (950nm, 49 mW/cm²) and an applied field of 4V. In the Jcy layer, diffusion is the main driving force acting on the charge carriers. The preferred direction of diffusion is marked in the graph.

3.7.5 External quantum efficiency of a photodetector
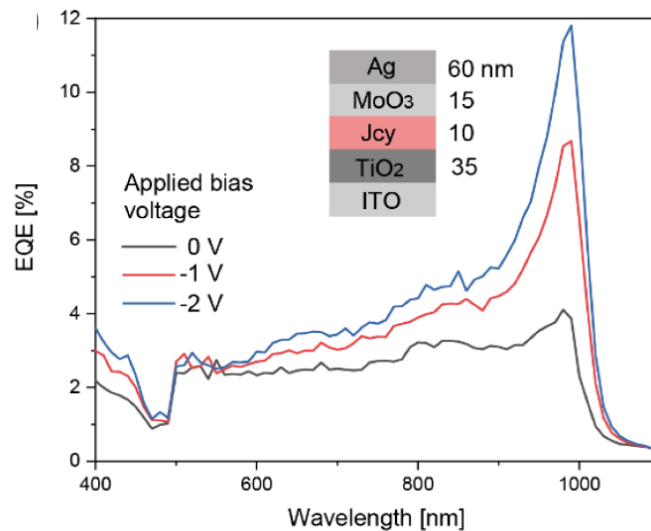
S3.5 External quantum efficiency for a photodetector setting with Jcy as absorbing layer. With increasing voltage, the efficiency increases

External quantum efficiency (EQE) measurements for a photodetector device (no emission layer present) at different voltages. The device architecture is ITO/TiO₂/Jcy/MoO₃/Ag. When the voltage is increased from 0 V to -2 V, the EQE at 995 nm increases from 3% to 12%.

3.7.6 Speed measurement in the frequency domain
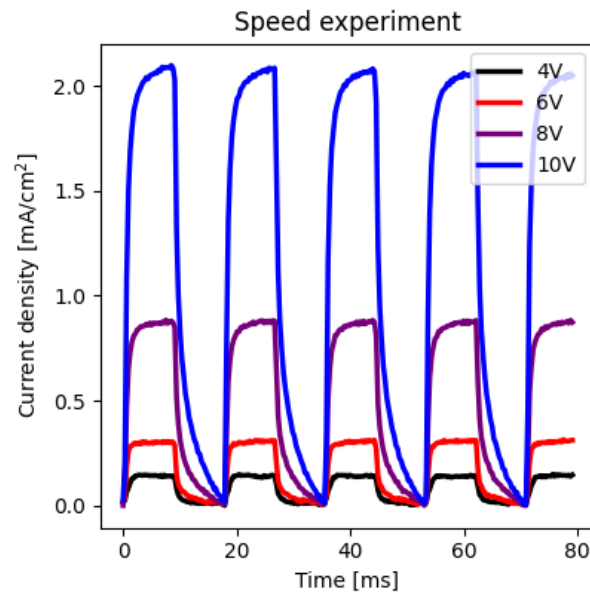
S3.6 Measurement data from transient photocurrent response measurement for 4,6,8, and 10 V

Transient photocurrent measurement of a SY-OUD at different voltages. It is clearly visible that the current density increases with voltage, as does the time to reach steady state.

3.7.7 Overshooting current at higher illumination intensities
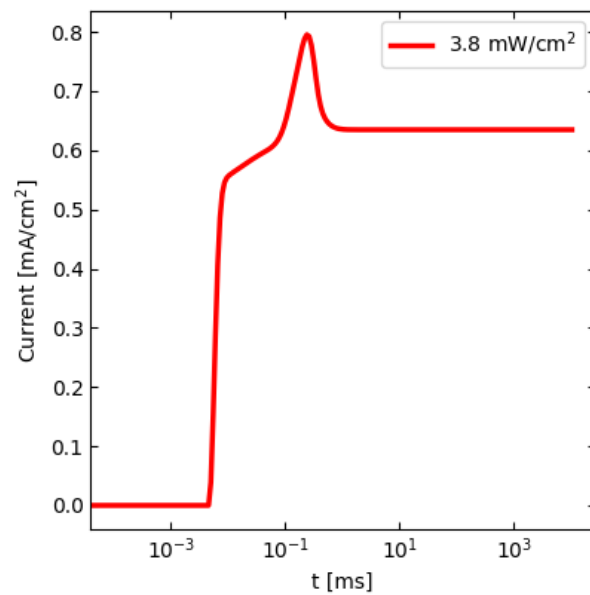
S3.7 transient current simulation for a light intensity of 3.8 mW/cm². An overshoot in current is visible.

For higher illumination, an overshoot in current is visible between 0.08 and 0.65 ms of the simulation. This is in the same order of magnitude as is expected for the transport time of electrons across the super yellow layer.

In this work, we capitalised on many advantages of drift-diffusion simulation. In chapter 1, we demonstrated that drift-diffusion is an excellent tool to generate simulated characterization data

on complete devices that can be used to compare the performance of different interpretation methods. This was done on the measurement method called thermally stimulated current (TSC), where the effect of thermal de-trapping is used to investigate energy, density and the emission rate of trap sites within a device. We could show that specific extraction methods like T4max - the method where it is assumed that the trap energy is proportional to the logarithm of the maximum temperature to the power of four - for TSC are not suitable for the extraction of reliable parameters since the underlying assumption of this method is not valid for organic semiconductors. In addition, the use of drift-diffusion allowed us to observe the dynamics of trap emptying and the impact of diffusion, which usually is neglected. Also, drift-diffusion simulation showed that the extracted current does not directly correspond to the number of involved charge carriers. Instead, there exists a proportionality factor which in TSC depends on trap distribution and extraction direction. This factor is known to occur when displacement currents are involved but rarely is considered in the traditional analysis of TSC data.

Another advantage of drift-diffusion used in chapter 1 is the possibility of studying parameter sensitivity. By changing varying parameter in the simulation, one can observe and quantify the change in the simulated characterization data. This allows the qualitative identification of the parameters which have the most considerable influence on a measurement and also can show whether parameters are correlated, i.e. whether it is possible to identify the parameter which is responsible for a change unambiguously. We found that the most crucial trap parameters energy, density and capture rate, can be identified clearly in TSC data. Usually, the correlation between different parameters makes the clear identification of the responsible parameter quite difficult.

Only if suitable parameters are chosen for a simulation, the results of a simulation are meaningful. It is sometimes quite difficult to extract the desired parameters from experiments, since it is not always possible to separate the effects from different sources. For example, the electron mobility extracted in measurements usually is influenced by the presence of electron trap sites. It is therefore possible to substitute a variation in trap density with a decreased mobility and vice versa. This became apparent in chapter 2 where the uncertainty in electron and hole mobility leads to a trap density estimation which varied by a factor 3 and even lead to different trap evolution trends. A part of the issue is a low device reproducibility. The devices were prepared by different people with varying expertise in device fabrication using different batches of materials. Also, environmental conditions like residual traces of oxygen and water in the glovebox as well as lab temperature are not stable. So even though the manufacturing process is standardised, the devices had a non-negligible variability in performance and also exhibited different behaviours depending on temperature. However, this difference in behaviour helped understand the different mechanisms taking place in the forming and dissolution of reversible trap sites. High quality devices have lower levels of trap sites. Counterintuitively, this increases the time which reversible trap sites require to dissolve. The proposed mechanism behind this trap recovery process is Shockley-Read-Hall recombination with charge carriers from the electrode followed by dissociation of the water-oxygen complex making up the trap. Devices with lower quality have an inherently higher number of water and oxygen molecules in the semiconducting layer. This leads to a higher voltage increase due to more trap formation during measurement. The presence of more trapped charge carriers upon turn-off will lead to larger number of free holes present in the device and thus a faster trap dissociation rate. The dynamics for trap decay was studied by transient drift-diffusion simulations.

Although quantitative analysis was not possible, the use of drift-diffusion helped understand the processes which take place within the superyellow PLED. Especially at lower fields, the electron

density will be a limiting factor for trap generation. It therefore is expected that the majority of electron trap sites will be close to the cathode as the electron density is highest there.

It is possible to generate quite complex stacks within the framework of drift-diffusion modelling. We showed that it is possible to simulate the behaviour of an all organic upconverter device by combining a photosensitive layer with an emissive layer using appropriate charge transport enhancing and blocking layers in-between.

Generally, local effects are hardly accessible via experimentation. Drift-diffusion thus is a valuable tool to understand local effects within a complete device. This was shown in chapter 3 where only the application of drift-diffusion could shed light on the unexpected behaviour of decreasing response speed in upconverter devices. We could show that at low light intensities, the electric field and thus the drift of electrons was low in the SY layer. This led to a mismatch between the number of holes and electrons in the device upon turn-on which needed some time to equilibrate. This equilibration time was the limiting factor for the speed of the device.

Drift-diffusion is a versatile tool that can be applied to various devices. We used it for simulation of a simple electrode-semiconductor-electrode sandwich as well as for an PLED and an upconverter device. It takes some time to master the use of drift-diffusion. However, if the time is invested, drift-diffusion can immensely aid in research by providing insight into the device. This allows for example to identify the areas where the device would profit most from optimisation.

Drift-diffusion is especially interesting if several different measurement methods are used to characterise a device. Only one model of the device needs to be generated which can be used to simultaneously fit all the measurements. This increases confidence in the extracted parameters. Though, a lot of time needs to be invested in order to find suitable values for model parameters.

However, it is important to keep in mind that drift-diffusion itself is only a model. This continuum model does consider the movement of free charged carriers inside a device depending on two effects – drift and diffusion. Other effects like coulomb interaction across longer distances and microscopic differences in the material are not explicitly considered. For this, different models would need to be employed.

Chapter 4: Outlook

4.1   Simulation of TSC

Thermally stimulated current is an interesting method for characterising trap states in low-conductivity organic semiconductors. It can simultaneously give information about trap energy, trapping dynamics and trap density and displays different sensitivities for these parameters, making it possible to distinguish between them. We showed that the most reliable results can be expected using the entire TSC formula. However, we only used this formula for discrete trap states with a band-like transport model. In order to be applicable to organic semiconductors with a more complex energetic structure, the TSC formula has to be adapted. For example, adding an integration over the trap energy distribution includes the trap energy distribution and introducing a temperature-dependent band edge accounts for the temperature-dependent accessibility of transport states.

Such extensions of the TSC formula make relying on iterative fitting procedures necessary since the formula is no longer analytically solvable. This more complex formula can be benchmarked as well with a more complex drift-diffusion simulation which also takes into account the trap energy distribution and the temperature dependent band edge. Also, in this context it would be interesting to investigate the sensitivity of the different parameters and determine the trap energy resolution – i.e. determine whether trap states with different energies can be distinguished.

Drift-diffusion simulation is an exciting tool to generate simulated data with varying complexity imitating the results of measurement methods. The approach used in chapter 1 can be extended to other measurement methods beyond TSC. One example is SCLC which can give information about the mobility of charge carriers. For the extraction of the mobility, it is possible to consider trap states with various distributions, making the model more complex, or disregard them altogether, making the model simpler. Benchmarking the different analysis methods would allow to estimate the errors that are introduced by using models with differing complexity and help find a good balance between time and effort spent on analysis and expected error in the extracted parameters.

4.2   Reversible trap states

The mobility value extracted by SCLC on bipolar devices has contributions from both electrons and holes. A way to separate electron and hole mobility is to switch to monopolar devices by using a metal-insulator-semiconductor device configuration or employing electrodes which either only inject holes or electrons. The mobility measured in such devices originates from only one kind of charge carriers, making it possible to determine the mobility of electrons and holes separately. With more accurate input parameters drift-diffusion can be used to make a quantitative prediction for the number and location of generated trap states. However, since we assume that SRH recombination plays a vital role in trap decay, we expect to see a different trap dissociation behaviour. Namely, the decay will be very slow and the recovery in electron-only devices thus less pronounced in the experimental timeframe we employed.

For the study of reversible trap states it is also necessary to refine the drift-diffusion model used. It is common for organic semiconductors to exhibit multiple kinds of trap states from different origins like shallow electron trap sites due to disorder and deep trap sites due to impurities like water-oxygen complexes. In the current drift-diffusion model, only one trap energy per type of charge carrier can be simulated. This means that currently either deep or shallow electron trap

sites can be simulated – but not both at once. Also, SRH recombination is not yet implemented for the EGD model. For the investigated devices, this recombination path is significantly influencing the performance. It is therefore only possible to quantify important charge transport parameters of organic semiconductors like mobility, trap energy and trap density after SRH recombination is implemented.

We theorise that the physical origin of the reversible trap states are water-oxygen complexes. However, it is difficult to measure the amount of such low quantities of water and oxygen in a full device. To further investigate this hypothesis, more indirect evidence is required. One possibility is to deliberately increase or decrease the water content of the devices by storing them in wet atmosphere or ultra high vacuum conditions. The voltage observed in the devices should reflect this change in water content if it is involved in trap formation.

Since drift-diffusion simulates steady state conditions, the use of other simulation tools like kinetic Monte Carlo might give further insight into the dynamics of trap state formation. For the in this work proposed trap states, four particles are required. It might be of interest to study the timescale of complex formation using three or four constituent particles.

The presence of trap states also has a significant influence on the luminance output of the device. A further step required for a full and comprehensible understanding of a PLED thus is the is the simulation of a combined electrical and optical model including exciton dynamics and outcoupling calculations. This will also allow to identify the location of the recombination zone and thus might give hints to the experimentalist as to where to start optimising.

4.3   Upconverter devices

While visible light is the only part of the electromagnetic spectrum that humans can directly observe, there are many interesting electromagnetic phenomena that remain hidden. Fortunately, there are technological solutions available to make these effects visible. One such solution involves using a near-infrared (NIR) sensitive photodetector in combination with a visible light-emitting diode (LED) to make infrared light visible to humans. Both the photodetector and LED have been extensively studied, but when connected in series, an optimisation of different aspects is necessary compared to each device separately. To evaluate the upconverter device, figures of merit such as speed and photon-to-photon conversion efficiency can be utilised.

For future work we recommend replacing the emissive layer with a material with higher intrinsic electron mobility or modifying the electron mobility of SY by trap dilution via implementation of an inert host with an active host or n-type doping. In general, the mobility of charge carriers appear to be limiting the device response time.

The drift-diffusion model of the upconverter device can be refined in a further step. Especially the generation, transport, and recombination of excitons can be introduced. At the moment, the generation efficiency of charge carriers in the photodetection layer is independent of the electric field and light intensity. Also, as a contact model, ohmic injection was used. However, with the large discrepancy in energy between the anode and the hole blocking TiO_2, a thermionic or even a tunneling injection model may be more appropriate.

The measurement was done with pulsed light while the simulation only considered the first half of a light pulse – i.e. turn-on. The possibility to simulate a pulsed light only recently was introduced in the most recent iteration of the drift-diffusion software. Implementing this pulsed light into a

simulation would allow to remove the time uncertainty between the cut-off frequency -3dB chosen as measurement parameter and the time to reach steady state chosen in the simulation.

Bibliography

[1]   B. Hepburn, H. Andersen, **2021**.

[2]   B.X. Dong, J. Wenderott, P.F. Green, *Colloid Polymer Science* **2021**, *299*, 439.

[3]   P. Stallinga, *Electrical characterization organic electronic materials Devices*, John Wiley & Sons**2009**.

[4]   J. Rao, X. Liu, X. Li, L. Yang, L. Zhao, S. Wang, J. Ding, L. Wang, *Angewandte Chemie* **2020**, *132*, 1336.

[5]   Y.H. Lee, W. Lee, T. Lee, J. Jung, S. Yoo, M.H. Lee, *Chemical Engineering Journal* **2023**, *452*, 139387.

[6]   Y. Zou, J. Hu, M. Yu, J. Miao, Z. Xie, Y. Qiu, X. Cao, C. Yang, *Advanced Materials* **2022**, *34*, 2201442.

[7]   J. Lu, Y. Zheng, Z. Chen, L. Xiao, Q. Gong, *Applied Physics Letters* **2007**, 91, 201107; doi: 10.1063/1.2813619

[8]   W. Van Roosbroeck, *The Bell System Technical Journal* **1950**, *29*, 560.

[9]   A. Jüngel, *Transport equations semiconductors*, Springer Berlin, Heidelberg**2009**.

[10]   Fluxim, *Setfos Manual*, Fluxim AG, Fluxim AG Katharina-Sulzer-Platz 2, CH8400 Winterthur Switzerland **2019**.

[11]   J. Huang, J. Lee, J. Vollbrecht, V.V. Brus, A.L. Dixon, D.X. Cao, Z. Zhu, Z. Du, H. Wang, K. Cho, others, *Advanced Materials* **2020**, *32*, 1906027.

[12]   T. Kerkhoven, *Computational Electronics Semiconductor Transport Device Simulation* **1991**, 21.

[13]   W. Kaiser, J. Popp, M. Rinderle, T. Albes, A. Gagliardi, *Algorithms* **2018**, *11*, 37.

[14]   Staudinger, *Berichte der Deutschen Chemischen Gesellschaft* **1920**, *53*, 1073.

[15]   C. Chiang, M. Druy, S. Gau, A. Heeger, E. Louis, A.G. MacDiarmid, Y. Park, H. Shirakawa, *Journal American Chemical Society* **1978**, *100*, 1013.

[16]   C. Chiang, Y.-W. Park, A. Heeger, H. Shirakawa, E. Louis, A.G. MacDiarmid, *The Journal Chemical Physics* **1978**, *69*, 5098.

[17]   C.K. Chiang, C. Fincher Jr, Y.W. Park, A.J. Heeger, H. Shirakawa, E.J. Louis, S.C. Gau, A.G. MacDiarmid, *Physical review Letters* **1977**, *39*, 1098.

[18]   H. Shirakawa, E.J. Louis, A.G. MacDiarmid, C.K. Chiang, A.J. Heeger, *Journal Chemical Society, Chemical Communications* **1977**, 578.

[19]   NobelPrize.org, **n.d.**

[20]   M.J.M. D.A. Papaconstantopoulos, in (Ed: P.W. Gerald L. Liedl Franco Bassani), Elsevir **2005**, 194.

[21]   K. Namsheer, C.S. Rout, *RSC advances* **2021**, *11*, 5659.

[22]   M. Christine K. Maitra Uday Walter Luscombe, pp. 169-183. https://doi. org/10. 1515/ct.-2020-0020 Susanne K.. " l vol. 3 no. 2 2021 Wiedmer, *Chemistry Teacher International* **2021**, *3*, 169.

[23]   F. Schauer, V. Nádaždy, K. Gmucová, *Journal Applied Physics* **2018**, *123*, 161590.

[24]   N. Apsley, H. Hughes, *Philosophical Magazine* **1974**, *30*, 963.

[25]   S. Fratini, D. Mayou, S. Ciuchi, *Advanced Functional Materials* **2016**, *26*, 2292.

[26]   V. Arkhipov, E. Emelianova, G. Adriaenssens, *Physical Review B* **2001**, *64*, 125125.

[27]   J. Shinar, *Organic Light Emitting devices survey*, Springer Science & Business Media**2004**.

[28]   I.E. Jacobs, A.J. Moulé, *Advanced Materials* **2017**, *29*, 1703063.

[29]   H.F. Haneef, A.M. Zeidell, O.D. Jurchescu, *Journal Materials Chemistry C* **2020**.

[30]   Y.-H. Lou, Z.-K. Wang, D.-X. Yuan, H. Okada, L.-S. Liao, *Applied Physics Letters* **2014**, *105*, 143_1.

[31]   L. Li, G. Meller, H. Kosina, *Solid state Electronics* **2007**, *51*, 445.

[32]   R. Street, M. Schoendorf, A. Roy, J. Lee, *Physical Review B* **2010**, *81*, 205307.

[33] F. Bussolotti, J. Yang, A. Hinderhofer, Y. Huang, W. Chen, S. Kera, A.T. Wee, N. Ueno, *Physical Review B* **2014**, *89*, 115319.

[34] J.Q. Zhong, H.Y. Mao, R. Wang, D.C. Qi, L. Cao, Y.Z. Wang, W. Chen, *The Journal Physical Chemistry C* **2011**, *115*, 23922.

[35] O. Rubel, S. Baranovskii, W. Stolz, F. Gebhard, *Physical review Letters* **2008**, *100*, 196602.

[36] D. Abbaszadeh, A. Kunz, N.B. Kotadiya, A. Mondal, D. Andrienko, J.J. Michels, G.-J.A. Wetzelaer, P.W. Blom, *Chemistry Materials* **2019**, *31*, 6380.

[37] H.T. Nicolai, M. Kuik, G. Wetzelaer, B. De Boer, C. Campbell, C. Risko, J. Brédas, P. Blom, *Nature materials* **2012**, *11*, 882.

[38] J.-M. Zhuo, L.-H. Zhao, R.-Q. Png, L.-Y. Wong, P.-J. Chia, J.-C. Tang, S. Sivaramakrishnan, M. Zhou, E.C.-W. Ou, S.-J. Chua, others, *Advanced materials* **2009**, *21*, 4747.

[39] Y. Zhang, B. de Boer, P.W. Blom, *Physical Review B* **2010**, *81*, 085201.

[40] M. Nikolka, I. Nasrallah, B. Rose, M.K. Ravva, K. Broch, A. Sadhanala, D. Harkin, J. Charmet, M. Hurhangee, A. Brown, others, *Nature materials* **2017**, *16*, 356.

[41] M. Nikolka, K. Broch, J. Armitage, D. Hanifi, P.J. Nowack, D. Venkateshvaran, A. Sadhanala, J. Saska, M. Mascal, S.-H. Jung, others, *Nature communications* **2019**, *10*, 1.

[42] P.A. Bobbert, A. Sharma, S.G. Mathijssen, M. Kemerink, D.M. de Leeuw, *Advanced materials* **2012**, *24*, 1146.

[43] K. Gu, Y.-L. Loo, *Journal Polymer Science Part B: Polymer Physics* **2019**, *57*, 1559.

[44] S. Fratini, M. Nikolka, A. Salleo, G. Schweicher, H. Sirringhaus, *Nature materials* **2020**, *19*, 491.

[45] W. Pasveer, J. Cottaar, C. Tanase, R. Coehoorn, P. Bobbert, P. Blom, D. De Leeuw, M. Michels, *Physical review Letters* **2005**, *94*, 206601.

[46] J.H. Burroughes, D.D. Bradley, A. Brown, R. Marks, K. Mackay, R.H. Friend, P.L. Burns, A.B. Holmes, *Nature* **1990**, *347*, 539.

[47] R. Marks, J. Halls, D. Bradley, R. Friend, A. Holmes, *Journal Physics: Condensed Matter* **1994**, *6*, 1379.

[48] S. Khalifeh, in (Ed: S. Khalifeh), ChemTec Publishing **2020**, 251.

[49] R. Aderne, K. Strassel, S. Jenatsch, M. Diethelm, R. Hany, F. Nüesch, R. dos Santos Carvalho, C. Legnani, M. Cremona, *Organic Electronics* **2019**, *74*, 96.

[50] S.E. Root, S. Savagatrup, A.D. Printz, D. Rodriquez, D.J. Lipomi, *Chemical reviews* **2017**, *117*, 6467.

[51] A. Irfan, A.R. Chaudhary, S. Muhammad, A.G. Al-Sehemi, H. Bo, M.W. Mumtaz, M.A. Qayyum, *Results Physics* **2018**, *11*, 599.

[52] X. Liu, K.S. Jeong, B.P. Williams, K. Vakhshouri, C. Guo, K. Han, E.D. Gomez, Q. Wang, J.B. Asbury, *The Journal Physical Chemistry B* **2013**, *117*, 15866.

[53] S. Ahmad, *Journal Polymer Engineering* **2014**, *34*, 279.

[54] Y. Cui, Y. Xu, H. Yao, P. Bi, L. Hong, J. Zhang, Y. Zu, T. Zhang, J. Qin, J. Ren, others, *Advanced Materials* **2021**, 2102420.

[55] S.K. Gupta, K. Dharmalingam, L.S. Pali, S. Rastogi, A. Singh, A. Garg, *Nanomaterials Energy* **2013**, *2*, 42.

[56] D. Ray, L. Burtone, K. Leo, M. Riede, *Physical Review B* **2010**, *82*, 125204.

[57] M. Mandoc, F. Kooistra, J. Hummelen, B. De Boer, P. Blom, *Applied Physics Letters* **2007**, *91*, 263505.

[58] N. Karl, *Synthetic Metals* **2003**, *133*, 649.

[59] J. Dacuña, A. Salleo, *Physical Review B* **2011**, *84*, 195209.

[60] T.-P. Nguyen, C. Renaud, P.L. Rendu, S.-H. Yang, *Physica status Solidi* **2009**, *6*, 1856.

[61] S. Wang, P. Kaienburg, B. Klingebiel, D. Schillings, T. Kirchartz, *The Journal Physical Chemistry C* **2018**, *122*, 9795.

[62] H. Woo, S. Jeon, *Scientific reports* **2017**, *7*, 1.

[63] L. Burtone, D. Ray, K. Leo, M. Riede, *Journal Applied Physics* **2012**, *111*, 064503.

[64]   Z. Lin, *Scientificreports* **2020**, *10*, 1.

[65]   M.B. Upama, M. Wright, B. Puthen-Veettil, N.K. Elumalai, M.A. Mahmud, D. Wang, K.H. Chan, C. Xu, F. Haque, A. Uddin, *RSC advances* **2016**, *6*, 103899.

[66]   D. Becker-Koch, B. Rivkin, F. Paulus, H. Xiang, Y. Dong, Z. Chen, A.A. Bakulin, Y. Vaynzof, *Journal Physics: Condensed Matter* **2019**, *31*, 124001.

[67]   Y. Nakayama, S. Kera, N. Ueno, *Journal Materials Chemistry C* **2020**, *8*, 9090.

[68]   C. Große, O. Gunnarsson, P. Merino, K. Kuhnke, K. Kern, *Nano Letters* **2016**, *16*, 2084.

[69]   Y. Fujii, *Surface Interface Analysis* **2016**, *48*, 1136.

[70]   R. Chen, Y. Kirsh, *The analysis thermally stimulated processes*, Elsevier**1981**.

[71]   A. Salleo, *Organic Electronics* **2013**, 341.

[72]   M. Zdzislaw Szymaski, B. Luszczyska, *Solution Processable Components Organic Electronic Devices* **2019**, 483.

[73]   F. AG, **n.d.**

[74]   R.R. Haering, E.N. Adams, *Physical Review* **1960**, *117*, 451.

[75]   G.A. Dussel, R.H. Bube, *Physical Review* **1967**, *155*, 764.

[76]   A. Lewandowski, S. McKeever, *Physical Review B* **1991**, *43*, 8163.

[77]   V. Arkhipov, E. Emelianova, R. Schmechel, H. Von Seggern, *Journal non-crystalline solids* **2004**, *338*, 626.

[78]   G. Garlick, A. Gibson, *Proceedings physical society* **1948**, *60*, 574.

[79]   Z. Fang, L. Shan, T. Schlesinger, A. Milnes, *Materials Science Engineering: B* **1990**, *5*, 397.

[80]   P. Yu, A. Migan-Dubois, J. Alvarez, A. Darga, V. Vissac, D. Mencaraglia, Y. Zhou, M. Krueger, *Journal non-crystalline solids* **2012**, *358*, 2537.

[81]   C. Qin, T. Matsushima, T. Fujihara, W.J. Potscavage Jr, C. Adachi, *Advanced Materials* **2016**, *28*, 466.

[82]   A. Halperin, A. Braner, *Physical Review* **1960**, *117*, 408.

[83]   A. Kadashchuk, R. Schmechel, H. Von Seggern, U. Scherf, A. Vakhnin, *Journal applied physics* **2005**, *98*, 024101.

[84]   T. Walter, R. Herberholz, C. Müller, H. Schock, *Journal Applied Physics* **1996**, *80*, 4411.

[85]   J.A. Carr, M. Elshobaki, S. Chaudhary, *Applied Physics Letters* **2015**, *107*, 107_1.

[86]   V.K. Khanna, *Extremetemperature harsh-environment electronics*, IOP Publishing Limited Bristol**2017**.

[87]   T. Sakanoue, H. Sirringhaus, *Nature materials* **2010**, *9*, 736.

[88]   W. Warta, N. Karl, *Physical Review B* **1985**, *32*, 1172.

[89]   S. Heun, P. Borsenberger, *Chemical physics* **1995**, *200*, 245.

[90]   H. Bässler, A. Köhler, in *Organic Light Emitting Diodes (OLEDs)*, Elsevier**2013**, 192.

[91]   H. Martens, P. Blom, H. Schoo, *Physical review B* **2000**, *61*, 7489.

[92]   T. Okachi, T. Nagase, T. Kobayashi, H. Naito, *Applied Physics Letters* **2009**, *94*, 20.

[93]   R.A. Awni, Z. Song, C. Chen, C. Li, C. Wang, M.A. Razooqi, L. Chen, X. Wang, R.J. Ellingson, J.V. Li, others, *Joule* **2020**, *4*, 644.

[94]   V. Nandal, S. Agarwal, P.R. Nair, *arXiv preprint arXiv:2106.06930* **2021**.

[95]   H.L. Gomes, P. Stallinga, F. Dinelli, M. Murgia, F. Biscarini, D. De Leeuw, T. Muck, J. Geurts, L. Molenkamp, V. Wagner, *Applied Physics Letters* **2004**, *84*, 3184.

[96]   S.A. Hawks, B.Y. Finck, B.J. Schwartz, *Physical Review Applied* **2015**, *3*, 044014.

[97]   F. Monestier, J.-J. Simon, P. Torchio, L. Escoubas, F. Flory, S. Bailly, R. de Bettignies, S. Guillerez, C. Defranoux, *Solar Energy Materials solar cells* **2007**, *91*, 405.

[98]   C. Li, L. Duan, H. Li, Y. Qiu, *The Journal Physical Chemistry C* **2014**, *118*, 10651.

[99]   A. Chauhan, S. Gupta, D. Taguchi, T. Manaka, P. Jha, P. Veerender, C. Sridevi, S. Koiry, S. Gadkari, M. Iwamoto, *RSC advances* **2017**, *7*, 11913.

[100]   D. Markov, C. Tanase, P. Blom, J. Wildeman, *Physical Review B* **2005**, *72*, 045217.

[101]   B. Ebenhoch, S.A. Thomson, K. Genevicius, G. Juška, I.D. Samuel, *Organic Electronics* **2015**, *22*, 62.

[102] W. Gill, *Journal Applied Physics* **1972**, *43*, 5033.

[103] H. Zheng, Y. Zheng, N. Liu, N. Ai, Q. Wang, S. Wu, J. Zhou, D. Hu, S. Yu, S. Han, others, *Nature communications* **2013**, *4*, 1.

[104] J. Bharathan, Y. Yang, *Applied Physics Letters* **1998**, *72*, 2660.

[105] S. Shin, M. Yang, L.J. Guo, H. Youn, *Small* **2013**, *9*, 4036.

[106] G. Gustafsson, Y. Cao, G. Treacy, F. Klavetter, N. Colaneri, A. Heeger, *Nature* **1992**, *357*, 477.

[107] Z. Zhang, W. Wang, Y. Jiang, Y.-X. Wang, Y. Wu, J.-C. Lai, S. Niu, C. Xu, C.-C. Shih, C. Wang, others, *Nature* **2022**, *603*, 624.

[108] J.H. Cook, J. Santos, H. Li, H.A. Al-Attar, M.R. Bryce, A.P. Monkman, *Journal Materials Chemistry C* **2014**, *2*, 5587.

[109] W. Li, B. Wang, T. Miao, J. Liu, G. Fu, X. Lü, W. Feng, W.-Y. Wong, *Journal Materials Chemistry C* **2021**, *9*, 173.

[110] M. Suh, J. Bailey, S.W. Kim, K. Kim, D.-J. Yun, Y. Jung, I. Hamilton, N. Chander, X. Wang, D.D. Bradley, others, *ACS Applied Materials & Interfaces* **2015**, *7*, 26566.

[111] B. Park, I.-G. Bae, S.Y. Na, Y. Aggarwal, Y.H. Huh, *Optics Express* **2019**, *27*, A693.

[112] A.J.H. G. M. Treacy Y. Cao F. Klavetter N. Colaneri G. Gustafsson, *Synthetic Metals* **1993**, *57*, 4123.

[113] B. Van der Zee, Y. Li, G.-J.A. Wetzelaer, P.W. Blom, *Advanced Materials* **2022**, *34*, 2108887.

[114] A.W.-P. Pavel Chulkin Ruslana Udovytska, J. Jung, *Polymers* **2021**.

[115] D.K. Franky So, *Advanced Materials* **2010**, *22*, 3762.

[116] I.P. Che Hsu Chi Zhang Hjalti Skulason Frank Uckert Dan LeCloux Yong Cao Sunghan Kim, *Journal Information Display* **2004**, *5*, 14.

[117] E. Khodabakhshi, J.J. Michels, P.W. Blom, *AIP Advances* **2017**, *7*, 075209.

[118] P.W.M.B. Y. Zhang 1 A. Palmaerts H. T. Nicolai M. Kuik R. J. P. Kist G. A. H. Wetzelaer J. Wildeman J. Vandenbergh L. Lutsen D. Vanderzande N. I. Craciun, *Journal of Applied Physics* **2010**, *107*, 124504.

[119] M. Diethelm, A. Devižis, W.-H. Hu, T. Zhang, R. Furrer, C. Vael, S. Jenatsch, F. Nüesch, R. Hany, *Advanced Functional Materials* **2022**, *32*, 2203643.

[120] Q. Niu, R. Rohloff, G.-J.A. Wetzelaer, P.W. Blom, N.I. Crăciun, *Nature materials* **2018**, *17*, 557.

[121] R.H. Michael Bauer Wei-Hsu Hu Camilla Vael Sandra Jenatsch Paul W. M. Blom Frank Nüesch Matthias Diethelm, *Advanced functional Materials* **2022**, *32*, 2106185.

[122] N.I.C. Gert-Jan A. H. Wetzelaer Paul W. M. Blom Quan Niu, *Advanced Electronic Materials* **2016**, *2*, 1600103.

[123] G. Zuo, M. Linares, T. Upreti, M. Kemerink, *Nature materials* **2019**, *18*, 588.

[124] E.M. Mohammadreza Fathollahi Tirad Barghi Saba Zare Zardareh Farhad Akbari Boroumand Mohsen Azadinia, *Journal electronic materials* **2020**, *49*, 3645.

[125] S.D. Yambem, K.-S. Liao, N.J. Alley, S.A. Curran, *Journal Materials Chemistry* **2012**, *22*, 6894.

[126] J. Cameron, P.J. Skabara, *Materials Horizons* **2020**, *7*, 1759.

[127] A.J. Bell, T.G. Wright, *Physical Chemistry Chemical Physics* **2004**, *6*, 4385.

[128] D. Upadhyay, P. Mishra, *Journal Molecular Structure: THEOCHEM* **2003**, *624*, 201.

[129] M. Kuik, G.-J.A. Wetzelaer, H.T. Nicolai, N.I. Craciun, D.M. De Leeuw, P.W. Blom, *Advanced Materials* **2014**, *26*, 512.

[130] A.E. Rico Meerheim Karsten Walzer Karl Leo Wilfried Lövenich Karsten Fehse, *Applied Physics Letters* **2008**, *93*, 083303.

[131] J.A.G. J. H. Kaufman P. J. Brock R. DiPietro J. Salem J. C. Scott, *Journal Applied Physics* **1996**, *79*, 2745.

[132] M.S. Abdou, F.P. Orfino, Y. Son, S. Holdcroft, *Journal American Chemical Society* **1997**, *119*, 4518.

[133] S. Burns, J. MacLeod, T. Trang Do, P. Sonar, S.D. Yambem, *Scientific reports* **2017**, *7*, 1.

[134] T. Ogawa, T. Nagata, Y. Hamada, *Journal applied polymer science* **1993**, *50*, 981.

[135] J.C. Blakesley, F.A. Castro, W. Kylberg, G.F. Dibb, C. Arantes, R. Valaski, M. Cremona, J.S. Kim, J.-S. Kim, *Organic Electronics* **2014**, *15*, 1263.

[136] B.J. Worfolk, S.C. Andrews, S. Park, J. Reinspach, N. Liu, M.F. Toney, S.C. Mannsfeld, Z. Bao, *Proceedings National Academy Sciences* **2015**, *112*, 14138.

[137] P. Sigaud, J.-N. Chazalviel, F. Ozanam, O. Stéphan, *Journal Applied Physics* **2001**, *89*, 466.

[138] G. Hong, A.L. Antaris, H. Dai, *Nature biomedical Engineering* **2017**, *1*, 1.

[139] R. Hany, M. Cremona, K. Strassel, *Science technology Advancedmaterials* **2019**, *20*, 497.

[140] K. Strassel, A. Kaiser, S. Jenatsch, A.C. Véron, S.B. Anantharaman, E. Hack, M. Diethelm, F. Nuesch, R. Aderne, C. Legnani, others, *ACS applied Materials & Interfaces* **2018**, *10*, 11063.

[141] K. Strassel, W.-H. Hu, S. Osbild, D. Padula, D. Rentsch, S. Yakunin, Y. Shynkarenko, M. Kovalenko, F. Nüesch, R. Hany, others, *Science technology Advanced materials* **2021**, *22*, 194.

[142] W.-H. Hu, C. Vael, M. Diethelm, K. Strassel, S.B. Anantharaman, A. Aribia, M. Cremona, S. Jenatsch, F. Nüesch, R. Hany, *Advanced Optical Materials* **2022**, *10*, 2200695.

[143] H. Zhang, S. Jenatsch, J. De Jonghe, F. Nüesch, R. Steim, A.C. Véron, R. Hany, *Scientific reports* **2015**, *5*, 1.

[144] A.C. Veron, H. Zhang, A. Linden, F. Nüesch, J. Heier, R. Hany, T. Geiger, *Organic letters* **2014**, *16*, 1044.

[145] H.-J. Jhuo, P.-N. Yeh, S.-H. Liao, Y.-L. Li, S. Sharma, S.-A. Chen, *Journal Materials Chemistry A* **2015**, *3*, 9291.

[146] X. Yang, D.C. Müller, D. Neher, K. Meerholz, *Advanced Materials* **2006**, *18*, 948.

[147] P. Tiwana, P. Docampo, M.B. Johnston, H.J. Snaith, L.M. Herz, *ACS nano* **2011**, *5*, 5158.

[148] H. Najafov, I. Biaggio, T.-K. Chuang, M.K. Hatalis, *Physical Review B* **2006**, *73*, 125202.

[149] L. Wang, S. Jenatsch, B. Ruhstaller, C. Hinderling, D. Gesevicius, R. Hany, F. Nüesch, *Advanced Functional Materials* **2018**, *28*, 1705724.

[150] M. Zhang, S. Höfle, J. Czolk, A. Mertens, A. Colsmann, *Nanoscale* **2015**, *7*, 20009.

[151] E.F. Schubert, *Light Emitting Diodes* **2006**, 275.

[152] S. Van Reenen, M. Vitorino, S. Meskers, R. Janssen, M. Kemerink, *Physical Review B* **2014**, *89*, 205206.

[153] K. Sreenath, C.V. Suneesh, V.K. Ratheesh Kumar, K.R. Gopidas, *TheJournal Organic Chemistry* **2008**, *73*, 3245.

[154] L.A. Curtiss, C.A. Melendres, A.E. Reed, F. Weinhold, *Journal of Computational Chemistry* **1986** 7(3):294 - 305

Curriculum Vitae

Camilla Vael

41, Altmattweg, 4600 Olten
PhD student at Swiss Federal Institute of Technology (EPFL)
Phone +41 79 739 48 09
E-Mail Camilla.vael@gmail.com

PROFESSIONAL EXPERIENCE - Scientific

Apr 2019 – to date	**FLUXIM AG (PhD position)**

(Swiss Private inc. producing simulation software and measurement hardware for industry and academia (about 30 employees))

- Creating simulation models for thermally stimulated current using **SETFOS** (Fluxim tool)
- Acting as consultant for **Swiss Federal Laboratories for Material Science and Technology** in NIR to visible light program up-converting devices
- Conducted experiments to determine trap states in super yellow PLED using **PAIOS** (Fluxim tool)
- Conducting data analysis using Python

Aug 2018 – Mar 2019	**LEICA Geosystems**

Swiss digital measurement specialist company, owned by Hexagon

(About 100 employees)

- Conducted QC testing of opto-acoustic crystal materials for use in development and commercial products
- Calibrated and stress tested laser tracking systems

Feb – Apr 2016	**Fossil Group Europe GmbH**
Mar – Apr 2015	Working as seasonal student for 3 consecutive years
Mar 2014	• Organized and lead set-up and technical support for customer iPads for the Basel World exhibition using Apple Configurator
	• Conducted user trainings in mobile device handling
	• Organized mobile device management and content management
	• Performed network patching of new office space
	• Provided on site IT support during office move

Jul 2019 – to date	**Swiss Federal Institute of Technology Lausanne (EPFL)**
	• Enrolled as PhD student
	• Passed oral exam – equivalent to Dr. des.
	• Public defence planned in September 2023
	• The Thesis work is based at and financed by Fluxim AG
	Title dissertation:
	Drift-Diffusion Simulations of Charge Transport and Trap Dynamics in Organic Semiconductor Materials
	Thesis Director: Prof. Frank Nüesch
	Thesis Co-director: Dr. Beat Ruhstaller
2018	**Master of Science in Nanosciences (M Sc)**
	University of Basel, Swiss Nanoscience Institute
	Title master thesis:
	Understanding a dual ion system: Properties governing the eligibility of an aqueous $ZnCl_2$ and LiCl based electrolyte for the use in large scale batteries
	Supervisors: Prof. Martino Poggio & Dr. Corsin Battaglia
	Additional master projects:
	• Investigation of components of p-type dye sensitized solar cells
	o Supervisor: Prof. Catherine Housecroft
	• Characterization of thin films fabricated by facing target sputtering
	o Supervisor: Prof. Hans J. Hug
	Practical part of master studies at Swiss Federal Laboratories for Material Science and Technology (EMPA, 1100 Employees, research lab for academia, industry, and public sector)
2017	**Bachelor of Science in Nanosciences (B Sc)**
	University of Basel, Swiss Nanoscience Institute
	Title: The different structures adapted by dehydrogenated DPDI on Cu111, Cu110 and Cu100
	Supervisor: Dr Aneliia Wäckerlin
	Practical part of the bachelor studies was done at University of Basel and Paul Scherrer Institute (Basel)

	Contributed talks
2022	**SimOEP,** Winterthur CH, Temperature dependent dynamics of reversible electron traps in polymer light-emitting diodes
2021	**EMRS spring**, online Verification of trap states parameters extracted from simulated TSC curves
2020	**Nanotexnology,** Thessaloniki, GR Simulation of TSC response of a solar cell using a drift diffusion model approach

	Campus presentations
2022	**EDMX research day**, online On the presence and formation of electron traps in polymer light-emitting diodes
2021	**EDMX research day**, online Using a drift diffusion modelling approach to study the sensitivity of characterization methods for determination of trap states in organic semiconductors
2021	**OEPHO**, online Experimental assessment of trap states in SY devices
2020	**OEPHO**, online Simulation of TSC response of a solar cell using a drift diffusion model approach

	Conference participation
2021	**Industrialization of perovskite PV**, online
2019	**Nanotexnology**, Thessaloniki, GR

LANGUAGE SKILLS

German: B2, native

English: B2

French: B1

Luxemburgish: A2

Danish: A2

OTHER SKILLS

- Programming in Python
- Advanced knowledge in SETFOS, a drift-diffusion simulation software (Fluxim AG)
- Experience with multi-measurement system PAIOS (Fluxim)
- Completed scanning electron microscopy course at University of Basel

Vael, C., Jenatsch, S., Züfle S., Nüesch, F., Ruhstaller, B.,
Scrutinizing thermally stimulated current transients originating from trapped charges in organic semiconductors: A drift-diffusion study, *Journal of Applied Physics* 131, 205702, 2022
https://doi.org/10.1063/5.0088426

Hu, W.-H., **Vael, C.**, Diethelm, M., Strassel, K., Anantharaman, S. B., Aribia, A., Cremona, M., Jenatsch, S., Nüesch, F., Hany, R., On the Response Speed of Narrowband Organic Optical Upconversion Devices. *Adv. Optical Mater.* 2022, 10,
2200695. https://doi.org/10.1002/adom.202200695

Diethelm, M., Bauer, M., Hu, W.-H., **Vael, C.**, Jenatsch, S., Blom, P. W. M., Nüesch, F., Hany, R., Electron Trap Dynamics in Polymer Light-Emitting Diodes. *Adv. Funct. Mater.* 2022, 32,
2106185. https://doi.org/10.1002/adfm.202106185

Diethelm, M., Devižis, A., Hu, W.-H., Zhang, T., Furrer, R., **Vael, C.**, Jenatsch, S., Nüesch, F., Hany, R., Traps for Electrons and Holes Limit the Efficiency and Durability of Polymer Light-Emitting Electrochemical Cells. *Adv. Funct. Mater.* 2022,203643. https://doi.org/10.1002/adfm.202203643